Tropical Water Quality Hub

National Environmental Science Programme

Final Report

Benthic light as ecologically-validated GBR-wide indicator for water quality

Drivers, thresholds and cumulative risks

Barbara J. Robson, Marites M. Canto, Lachlan I. McKinna, M. Logan, S. Lewis and Katharina E. Fabricius

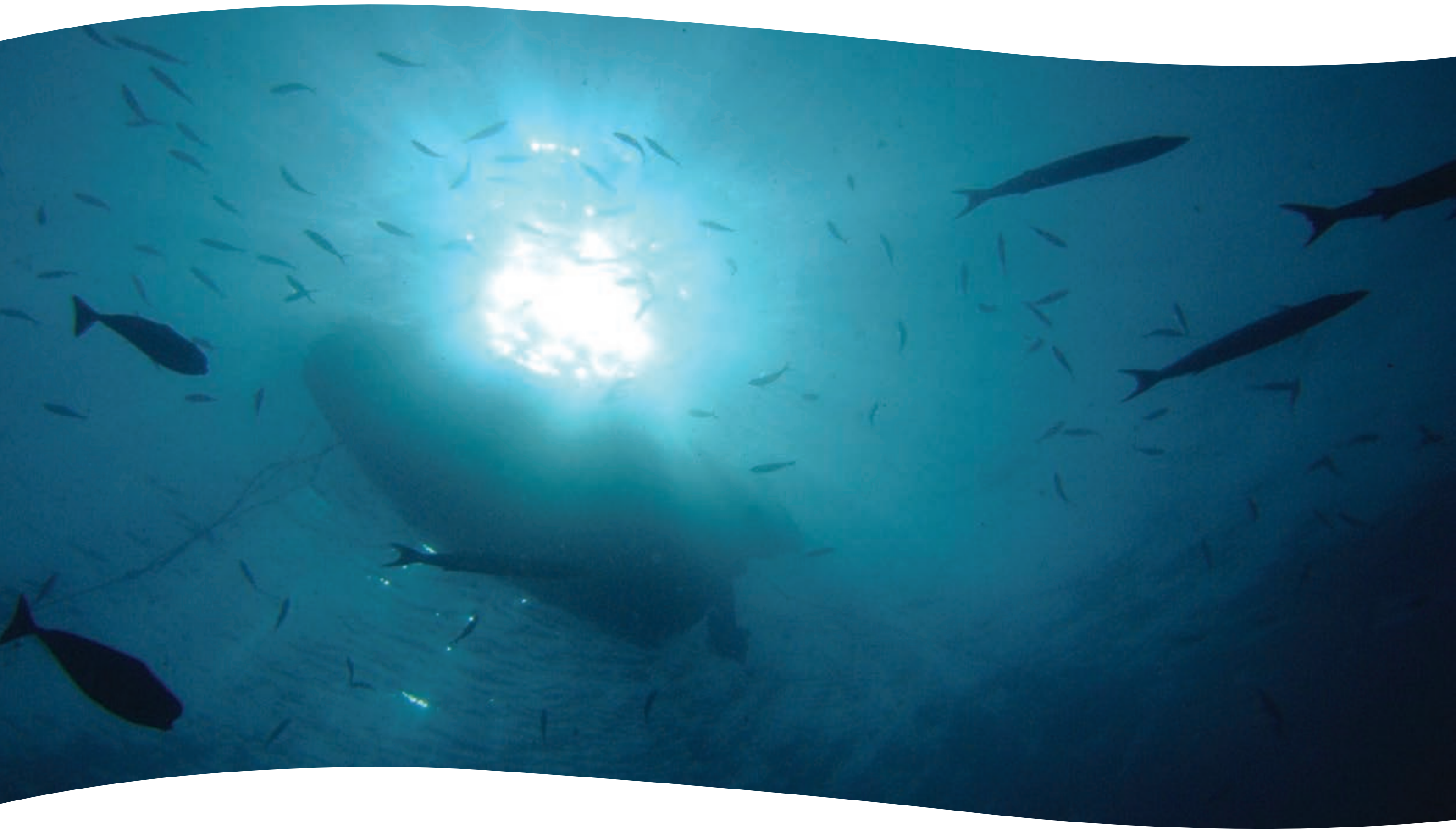

Australian Government

Australian Institute of Marine Science

Benthic light as ecologically-validated GBR-wide indicator for water quality

Drivers, thresholds and cumulative risks

Barbara J. Robson[1,2], Marites M. Canto[2,3], Lachlan I. McKinna[4], M. Logan[1], S. Lewis[3] and Katharina E. Fabricius[1,2]

[1] Australian Institute of Marine Science
[2] AIMS@JCU
[3] James Cook University
[4] Go2Q Consulting

Australian Government

National Environmental Science Programme

Supported by the Australian Government's
National Environmental Science Program
Project 5.3 Benthic light as ecologically-validated GBR-wide indicator for water quality: Drivers, thresholds and cumulative risks

National Library of Australia Cataloguing-in-Publication entry:
978-1-925514-74-2

This report should be cited as:
Robson, B.J., Canto, M.M., McKinna, L.I., Logan, M., Lewis, S. and Fabricius, K.E. (2021) *Benthic light as ecologically-validated GBR-wide indicator for water quality: Drivers, thresholds and cumulative risks.* Report to the National Environmental Science Program. Reef and Rainforest Research Centre Limited, Cairns (110pp.).

Published by the Reef and Rainforest Research Centre on behalf of the Australian Government's National Environmental Science Program (NESP) Tropical Water Quality (TWQ) Hub.

The Tropical Water Quality Hub is part of the Australian Government's National Environmental Science Program and is administered by the Reef and Rainforest Research Centre Limited (RRRC). The NESP TWQ Hub addresses water quality and coastal management in the World Heritage listed Great Barrier Reef, its catchments and other tropical waters, through the generation and transfer of world-class research and shared knowledge.

Cover photographs: (front) Light in coastal oceans is strongly indetermined by water quality. It is a critical factor for the health of marine ecosystem, and hence also for the prosperity of communities that depend on them for their livelihoods. Image: Katharina Fabricius, AIMS; (back) Image: Renata Ferrari.

This report is available for download from the NESP Tropical Water Quality Hub website:
http://www.nesptropical.edu.au

CONTENTS

LIST OF TABLES

LIST OF FIGURES

ACRONYMS

AIMS .... Australian Institute of Marine Science
bPAR .... benthic Photosynthetically Active Radiation
bPAR Index . benthic Photosynthetically Active Radiation Index
DSA .... Depth Sensitivity Analysis
EAC .... East Australian Current
GBR .... Great Barrier Reef
GBRMPA ...... Great Barrier Reef Marine Park Authority
IMOS .... Integrated Marine Observing System
IOP .... Inherent Optical Property
ISP .... Independent Science Panel
JCU .... James Cook University
MMP .... Marine Monitoring Program
NAP .... Non Algal Particulates
NESP .... National Environmental Science Program
RRRC .... Reef and Rainforest Research Centre Limited
GBR .... Great Barrier Reef
GBRMPA ...... The Great Barrier Reef Marine Park Authority
MODIS .... Moderate Resolution Imaging Spectroradiometer, a satellite-based earth observing system run by NASA.
MMP .... Marine Monitoring Program
NRM .... Natural Resource Management
NESP .... National Environmental Science Program
OGBR .... Office of the Great Barrier Reef, Queensland Government
PAR .... Photosynthetically Active Radiation
P-E .... Photosynthesis-Irradiance (E is the symbol most commonly used to represent irradiance in the optical science literature)
SeaSIM .... Australia's National Sea Simulator
TWQ .... Tropical Water Quality
UPD .... Unbiased Percent Difference

ACKNOWLEDGEMENTS

This research was supported by the Australian Government's National Environmental Science Program (NESP) Tropical Water Quality (TWQ) Hub. The bPAR index presented here supersedes the version presented in the final report of NESP TWQ Hub Project 2.3.1: Benthic light as ecologically-validated GBR-wide indicator for water quality: drivers, thresholds and cumulative risk.

We thank Carol Honchin at the Great Barrier Reef Marine Park Authority (GBRMPA) and members of the Great Barrier Reef (GBR) Independent Science Panel (ISP), particularly Dr. Peter Doherty and Dr. Roger Shaw, for their feedback and suggestions to improve the index.

The development of the remote sensing bPAR algorithm and the bPAR index received additional support from an AIMS@JCU scholarship awarded to Marites Magno-Canto. AIMS@JCU is a joint initiative of the Australian Institute of Marine Science (AIMS) and James Cook University (JCU).

The Integrated Marine Observing System (IMOS) provided collaborative support for the deployment, maintenance and retrieval of the benthic light loggers. Thanks in particular to Chris Bartlett (AIMS) for his role in this.

Many thanks to Dr. Rodrigo Garcia (University of Massachusetts, Boston) and Dr. Paul Muir (Museum of Tropical Queensland) for assistance in identifying and correcting an error in an earlier version of the algorithm for calculating benthic PAR from remote sensing ocean colour data.

Many thanks to Dr. Angus Thompson (AIMS) and the Marine Monitoring Program (MMP) for sharing code, data and insight required for Section 6.2. Dr. Thompson will be a co-author of the planned paper to arise from this chapter.

Similarly, thanks are due to Dr. Catherine Collier, Luke Hoffman and Dr. Alex Carter, of James Cook University, for the modelling and analyses and text presented in Section 6.3. Dr. Collier and her team will lead a planned paper to arise from this chapter.

Thanks are also due to CSIRO (Dr. Mark Baird and team) and the Office of the Great Barrier Reef (particularly Dr. Paulina Kaniewska) for providing us with access to the eReefs catchment land use management change scenarios.

Thanks to Grace Frank, Miles Grandy and Renata Ferrari for allowing us to use their fantastic photos in this report.

Finally, thanks to Carol Honchin (GBRMPA) and Dr. Roger Shaw (GBR ISP) for their constructive and timely reviews of the draft of this report.

EXECUTIVE SUMMARY

While climate change is acknowledged as the greatest current threat to the Great Barrier Reef (GBR), substantial declines in GBR coral cover and ecosystem values have also been attributed to chronic stress resulting from reduced water quality. To manage water quality and the impacts of poor water quality on the World Heritage values of the GBR, it is essential that we have effective ways to measure, monitor and report key indicators of water quality on the scale of the whole of the GBR.

In this Report, we:

1) Describe in detail a **new method to measure** benthic light (bPAR) across the whole GBR using satellite ocean colour observations.
2) **Develop and introduce the bPAR index**, a new indicator of chronic light stress that can be used to monitor and report on water quality in the GBR.
3) Present time-series of **seasonal and annual variations in the bPAR index** across all GBR NRM Management Regions (from Cape York to the Burnett Mary) and Water Bodies (from Closed Coastal to Offshore).
4) Show that in Coastal and Midshelf regions **the bPAR index is sensitive to variations in river discharges** of freshwater, sediment and nutrient loads from GBR catchments.
5) Show that the **bPAR index predicts some of the variability in ecological outcomes** in the GBR including changes in coral community resilience. The regionally aggregated bPAR index predicts more of the variability in the GBR Marine Monitoring Program's recently-developed coral index than any other proposed water quality indicator considered, including river discharge, non-algal particulates or chlorophyll *a*. After the effects of known acute disturbances (bleaching events, crown of thorns starfish outbreaks, storm damage and exposure to freshwater plumes, which collectively account for more than 70% of total variability) are removed, variations in the bPAR index account for 43% of the remaining temporal variability in change in coral index in the Fitzroy Midshelf region, 33% of the variability in the Fitzroy Open Coastal region, 37% of the variability in the Wet Tropics Midshelf region, and 25% of the variability in the Dry Tropics Open Coastal region.
6) Show that **bPAR simulated by the eReefs models provides a suitable alternative data source for calculation of the bPAR index on seasonal and annual time-scales**. While it is not identical to remote sensing or *in situ* bPAR, it provides predictive power very similar to that of the bPAR index calculated from satellite ocean colour.

In conclusion, we recommend that the bPAR index be further explored as a potential indicator of water quality in future Reef Reports and catchment management policy scenario evaluations.

1.0 INTRODUCTION

While climate change is acknowledged as the greatest current threat to the Great Barrier Reef (GBR) (Great Barrier Reef Marine Park Authority, 2019), substantial declines in GBR coral cover and ecosystem values have also been attributed to chronic stress resulting from reduced water quality (Schaffelke et al., 2017). To manage water quality and the impacts of poor water quality on the World Heritage values of the GBR, it is essential that we have effective ways to measure, monitor and report key indicators of water quality on the scale of the whole of the GBR.

This NESP TWQ Hub Project 5.3: Benthic light as ecologically-validated GBR-wide indicator for water quality: drivers, thresholds and cumulative risk follows on from the previous NESP TWQ Hub Project 2.3.1 (Robson et al., 2019). In that Project, we assessed the light requirements of key habitat-building GBR coral species through experiments in the National Sea Simulator (SeaSim) (DiPerna et al., 2018; Strahl et al., 2019), and reviewed published literature regarding the light requirements of seagrasses. We used this information to develop and propose a new water quality indicator based on remote sensing of benthic photosynthetically active radiation (bPAR).

In this Project, we have developed and published a new method for measuring bPAR from satellite ocean colour observations of the GBR (Magno-Canto et al., 2019; Magno-Canto et al., 2020b) and, incorporating feedback from key stakeholders, have developed an improved bPAR index that can be used to monitor variations in water clarity across all GBR NRM Regions and Water Bodies (Canto et al., submitted).

Chapter 2.0 of this report documents the technical details of the method to calculate bPAR from ocean colour observations. The method makes use of the shallow water inversion model (SWIM) approach (McKinna et al., 2015), which is similar to earlier methods such as the adaptive Linear Matrix Inversion (aLMI) applied to the eReefs remote sensing data products (Brando et al., 2013) but improves upon them by accounting for the effects of light reflected from the seafloor in optically shallow waters.

Chapter 3.0 discusses the options for ongoing operational delivery of bPAR data needed of the bPAR index. Subsequent chapters focus on development of applications to the whole GBR. Chapter 4.0 describes the development of the new bPAR index and presents time-series of variations in the bPAR index calculated over both annual and seasonal reporting periods for each year between 2003 and 2019 for each NRM Region and Water Body in the GBR.

In Chapter 5.0, we present an analysis of the relationship between variations in the bPAR index and river discharge in each NRM region, showing that year-to-year variations in river discharge, sediment and nutrient loads are a key determinant of impacted water clarity in coastal regions and some midshelf regions of the GBR, while offshore regions maintain consistently high bPAR index scores, suggesting consistently good water quality.

For the bPAR index to become a useful and trusted indicator of water quality and GBR health, it is important that we can demonstrate that the new index is a useful predictor of spatial and variations and temporal changes in ecological outcomes. In Chapter 6.0, we discuss several analyses that have been performed in collaboration with other NESP TWQ projects that have found bPAR data layers and the new bPAR index to be useful predictors of seagrass distribution and seagrass and coral community composition. In addition, we present a new analysis that shows that the regionally aggregated bPAR index is, in areas impacted by variable water quality, a strong predictor of changes in coral community resilience as measured by the coral index (Thompson et al., 2020).

2.0 CALCULATION OF DAILY INTEGRATED BENTHIC PHOTOSYNTHETICALLY AVAILABLE RADIATION (BPAR) FROM REMOTE SENSING OCEAN COLOUR OBSERVATIONS

The work presented in Chapter 2.0 forms part of the PhD thesis of Marites Magno-Canto and has been published in the peer-reviewed international journal, *Optics Express*. Citation details are as follows:

1) Magno-Canto, M.M., McKinna, L.I., Robson, B.J. and Fabricius, K.E., 2019. Model for deriving benthic irradiance in the Great Barrier Reef from MODIS satellite imagery. Optics express, 27(20), pp.A1350-A1371. (link)
2) Magno-Canto, M.M., McKinna, L.I., Robson, B.J., Fabricius, K.E. and Garcia, R., 2020. Model for deriving benthic irradiance in the Great Barrier Reef from MODIS satellite imagery: erratum. Optics Express, 28(19), pp.27473-27475. (link)

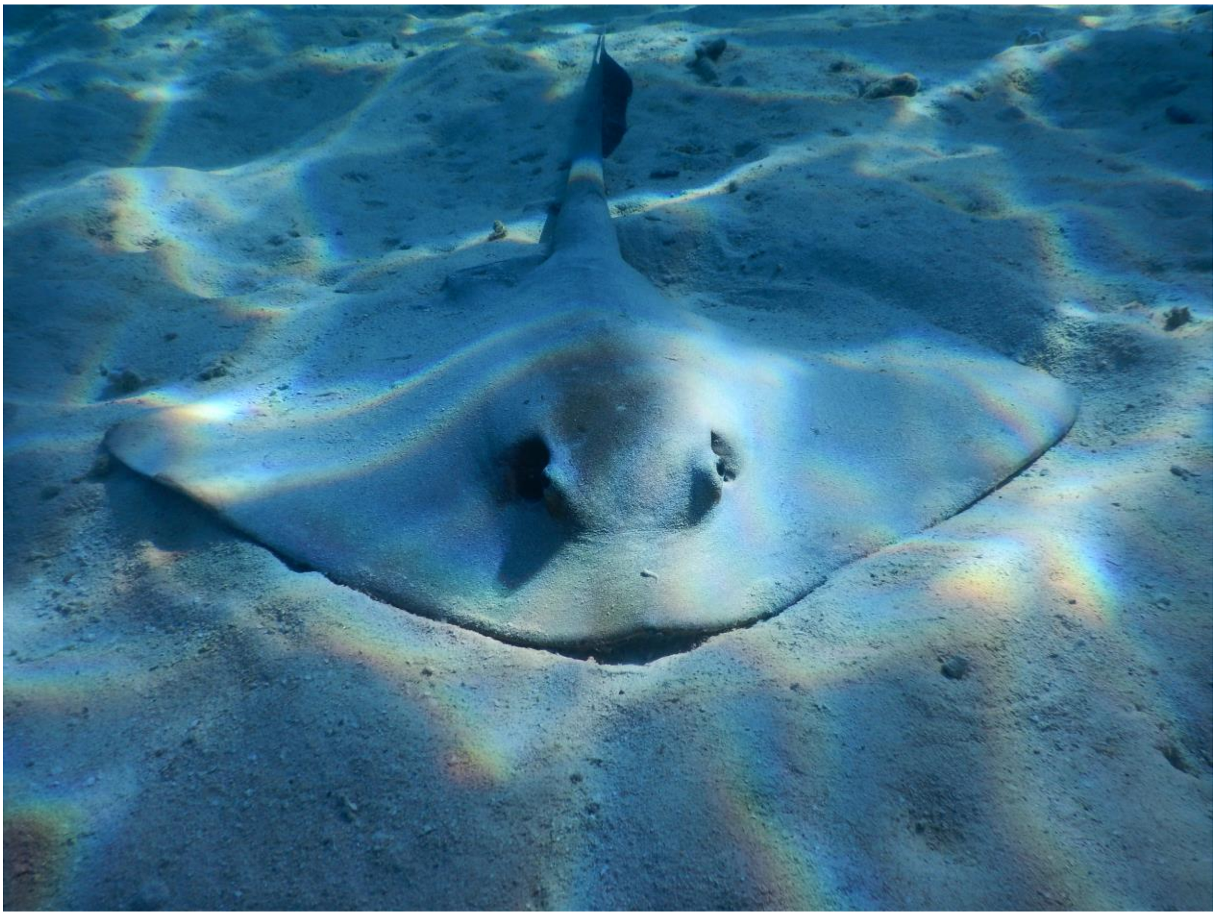

Figure 1: Dappled light at the bottom of GBR waters illuminates a ray. Credit: Miles Grandy.

2.1 Introduction

Benthic irradiance is defined as photosynthetically active radiation (PAR, or benthic PAR) at 400 – 700 nm wavelengths that reaches the seafloor. Benthic PAR provides the primary energy resource that drives benthic photosynthesis, thus essentially defines primary production in the benthic coastal ocean (Gattuso et al., 2006). Previous studies have emphasised the importance of light availability for benthic habitats. For example, light limitation determines photosynthesis, growth, and distribution of seagrasses (Collier et al., 2012a; Ralph et al., 2007), depth limits for coral reef development (Cooper et al., 2007; Fabricius, 2011; Kleypas et al., 1999; Muir et al., 2015), and vulnerability of coral reefs to ocean acidification as a result of reduced calcification (Suggett et al., 2013; Vogel et al., 2015). On the other hand, high light levels in combination with heat stress from elevated seawater temperature can also lead to coral bleaching (Baird et al., 2018; Hughes et al., 2018a). Such juxtaposition thus highlights the need for an improved understanding of the underwater light field and benthic light availability, to better assess and manage marine ecosystem health (Collier et al., 2012a; Fabricius, 2011). Efficient management of these benthic ecosystems would greatly benefit from a synoptic- scale understanding of spatial and temporal patterns of benthic light availability. Unfortunately, benthic light availability remains poorly understood (Ackleson, 2003; Gattuso et al., 2006), because datasets that could provide the much-needed information are either insufficient or lacking, including in one of the largest coral reef ecosystem on Earth, the Great Barrier Reef (GBR). As such, our main objective is to demonstrate the feasibility of estimating benthic light values within the GBR region using a remote sensing model to bridge this knowledge gap.

The GBR Marine Park (GBRMP) is a world heritage listed site adjacent to north-eastern Australian coast spanning from 10°S to 24°S latitude. It is located on a continental shelf with an area of ~344,000 km^2. While direct observations of the underwater light field have historically been measured by ships of opportunity and *in situ* moorings in the GBR, these existing data are spatially and temporally sparse. Although PAR in surface waters is frequently reported for marine ecosystems (Frouin et al., 2012), benthic PAR is usually available only at a few point locations over relatively short periods (Anthony et al., 2004; Ralph et al., 2007; Whinney et al., 2017). To understand the responses of whole ecosystems at regional scales, we need to estimate environmental conditions, including benthic PAR, at relevant scales (in this case, the scale of the whole GBR). Ocean colour remote sensing presents an option for observing benthic PAR in the GBR at ecologically relevant spatio-temporal scales, which can provide near-daily images of the entire GBR at a nominal pixel resolution of 1 km^2. While a number of ocean colour satellite processing algorithms have been developed for monitoring optically complex waters of the GBR (McKinna et al., 2015; Slivkoff, 2014; Weeks et al., 2012), we note that none have focused on deriving benthic light availability.

Benthic irradiance, here denoted as $E_b(\lambda)$, is essentially regulated by three factors. First, the downwelling irradiance incident on the ocean surface, $E_d^{0^+}(l, q'_{solz}(f))$ (W m^{-2}), which is subject to atmospheric processes (e.g., gaseous absorption and molecular scattering) that diminishes light as it makes it way to the sea surface. Second, the absorption and scattering processes within the water column (Ackleson, 2003; Kirk, 2011; Werdell et al., 2018) that depends on wavelength and have magnitudes and shapes that are proportional to the relative concentration of optically-active constituent matter (Robinson, 2004) including: phytoplankton, non-algal particles (NAP) and coloured dissolved organic matter (CDOM). It is important to note that Inherent Optical Properties (IOPs) are impartial to the direction and magnitude of the ambient light field (Mobley, 1994). In coastal regions, IOPs can be regulated by a number of drivers including, but not limited to: run-off and resuspension of fine sediments, nutrients and organic matter due to wave-induced vertical mixing, human activity such as dredging and dredge-spoil placement on the seafloor, and biological processes related to phytoplankton growth. Collectively, these drivers make the inversion of sensor-observed remote sensing reflectance, $R_{rs}(\lambda)$ (sr^{-1}), to derive IOP values, a non-trivial problem. Third, and also important is the water column depth which defines the distance of light penetration.

In optically shallow waters like those of the GBR, light reflected off the seafloor is another factor that limits the application of contemporary ocean colour algorithms developed for deep, open-ocean waters (McKinna and Werdell, 2018; McKinna et al., 2015). Fortunately, a GBR-specific IOP inversion model (Shallow Water Inversion Model, SWIM) has recently been developed (McKinna et al., 2015) that improves the derivation of spectral estimates of IOPs, specifically, total absorption coefficients, $a(\lambda)$ (m^{-1}), and total backscattering coefficients, $b_b(\lambda)$ (m^{-1}), for any pixel within the GBR where $R_{rs}(\lambda)$ are available. We note that $R_{rs}(\lambda)$ is a fundamental sensor-observed radiometric variable used in ocean colour algorithms. SWIM is described in detail elsewhere (see (McKinna et al., 2015)]). In brief, SWIM takes advantage of two mapped GBR-specific ancillary datasets, namely: (i) a high-resolution shelf bathymetry map (Beaman, 2010) matching the resolution of the remote sensing datasets, and (ii) a bottom substrate brightness (albedo) map (Reichstetter et al., 2015). Using these ancillary datasets, SWIM can generally correct for optically shallow effects. Note however, that for more optically complex waters, the skill of the SWIM model may still be challenged in deriving IOP values. Nonetheless, the IOP estimates that can be obtained via SWIM are the best available for our current purpose. By using SWIM-derived IOPs, it is thus possible to spectrally characterise near-daily GBR-wide light attenuation and, in turn, estimate benthic light availability (i.e., PAR) using ocean colour remote sensing.

A contemporary approach for estimating PAR at depth is to use the broadband, water- column averaged diffuse attenuation coefficient of PAR, K_d(PAR) (m^{-1}), and the Lambert- Beer's Law which assumes K_d(PAR) is constant over the optical pathlength (depth). However, in practice, K_d(PAR) exhibits strong depth dependence, particularly in the upper water column, even in well-mixed waters (Lee et al., 2005a; Lee et al., 2005b; Lee et al., 2014). Thus, using a K_d(PAR)-based method may lead to inaccurate estimates of PAR at depth. We note that usable solar radiation (*USR*), a spectrally integrated broadband term (integrated over the 400 – 560 nm range), has recently been proposed as a promising alternative to PAR (Lee et al., 2014) as its diffuse attenuation coefficient, K_d(USR) (m^{-1}), exhibits less depth dependence. However, most ecological studies report their findings (e.g., benthic light stress thresholds) in terms of PAR. Here, we described a remote sensing approach to estimate benthic PAR that does not use K_d(PAR).

In this study, we demonstrate a simple physics-based ocean colour remote sensing model to estimate two spectrally integrated benthic light variables, namely: (i) instantaneous PAR at the seafloor (hereby denoted as $bPAR_i$) (μmol photons m^{-2} s^{-1}), and (ii) daily integrated PAR at the seafloor (hereby denoted as $bPAR_d$) (mol photons m^{-2} d^{-1}). Estimates are derived from (i) $E_d^{0^+}(\lambda,\theta'_{solz}(\phi))$, (ii) high resolution shelf bathymetry, and (iii) spectral estimates of IOPs obtained using SWIM (McKinna et al., 2015). Here, $E_d^{0^+}(\lambda)$ and IOPs are derived from data collected by NASA's Moderate Resolution Imaging Spectroradiometer aboard the Aqua spacecraft (MODIS Aqua). We then validate the model by comparing concurrent satellite-derived and observed *in situ* benthic PAR values from four test sites within the GBR. Finally, results, as well as limitations and future applications of the model within the GBR region are discussed.

2.2 Benthic irradiance model

2.2.1 Benthic irradiance model description

To derive $E_b(\lambda)$, the total amount of subsurface downwelling planar irradiance, $E_d(\lambda,0^-)$ (W m^{-2}), transmitted to a depth z (m) under a clear sky, we used the Lambert-Beer's Law:

$$E_b(\lambda) = E_d(\lambda, 0^-)\exp(-K_d(\lambda)z) \qquad (1)$$

where $K_d(\lambda)$ (m^{-1}) is the spectral diffuse attenuation coefficient. We emphasise that in our approach, spectral dependence was kept throughout all calculations.

Satellite-derived $E_d^{0^+}(\lambda, \theta'_{solz}(\phi))$ (W m^{-2}) represents the downwelling planar irradiance when the Sun is at zenith and just above the air-sea surface. Here, $E_d^{0^+}(\lambda, \theta'_{solz}(\phi))$ was obtained by employing the standard NASA atmospheric transmittance model as described by Mobley (1994) which assumes that the cloud/surface system is non-reflecting and non-absorbing. Because $E_d^{0^+}(\lambda, \theta'_{solz}(\phi))$ is estimated just above the sea surface, it is necessary to propagate this parameter across the air-sea interface to derive $E_d^{0^+}(\lambda, \theta'_{solz}(\phi))$ (Kirk, 1992, 2011). Here, we followed (Baker and Smith, 1990) and used:

$$E_d(\lambda, 0^-) = t_g E_s(\lambda, 0^+) \qquad (2)$$

where t_g is the global transmittance of the air-water interface (Smith and Baker, 1986). Essentially, the total downwelling global irradiance just above the interface can be decomposed into direct ("sun") and diffuse ("sky") components, both of which are functions of wavelength and the corresponding solar zenith angle in air (Baker and Smith, 1990) and t_g is equal to $t_g = (1 - \rho_{sun})(1 - y) + (1 - \rho_{sky})(y)$, where ρ_{sky} and ρ_{sun} are the sea surface reflectance of the diffuse and the direct irradiances, respectively. The value of ρ_{sky} is roughly equivalent to 0.066 for cloud-free conditions (Baker and Smith, 1990) while the ρ_{sun} can be approximated by employing the Fresnel reflectance equation for unpolarised light (Mobley, 1994) written as:

$$\rho_{sun} = \left(\left[\frac{\sin(\theta_{solz} - \theta_t)}{\sin(\theta_{solz} + \theta_t)} \right]^2 + \left[\frac{\tan(\theta_{solz} - \theta_t)}{\tan(\theta_{solz} + \theta_t)} \right]^2 \right) * 0.5 \qquad (3)$$

where θ_{solz} (degrees) is the solar zenith angle in air at the time of satellite overpass and θ_t (degrees) is the solar zenith angle of light transmitted downward in the water calculated as:

$$\theta_t = \sin^{-1}(\sin\theta_{solz} / n_w) \qquad (4)$$

where n_w is the real refractive index of seawater approximately equal to 1.34 (Mobley, 1994). For cases where $\theta_{solz} \neq 0.0$ (e.g., sun not overhead), Eq. (3) was used. Otherwise, for normally incident light, the reflectance of the direct irradiance was calculated as:

$$\rho_{sun} = \left(\frac{n_w - 1}{n_w + 1} \right)^2 . \qquad (5)$$

We note that in this study we have assumed cloud-free, clear sky conditions for all calculations and neither considered the effect of a wind-roughened surface in our air-sea transmittance calculations. Further details on deriving the transmitted irradiance across the interface are described elsewhere (Baker and Smith, 1990; Smith and Baker, 1986).

An IOP-based method for deriving $K_d(\lambda)$ (Lee et al., 2005b) was employed as this approach is more robust in optically complex coastal waters relative to simple empirical methods (Austin and Petzold, 1981; Morel, 1988; Morel et al., 2007; Mueller, 2000). The IOP-based $K_d(\lambda)$ model we have used in this study is described and evaluated in detail elsewhere (Lee et al., 2005a; Lee et al., 2005b) and has a general form:

$$K_d(\lambda) = (1 + 0.005\theta_{solz})a(\lambda) + 4.18(1 - 0.52e^{-10.18a(\lambda)})b_b(\lambda) \qquad (6)$$

where $a(\lambda)$ and $b_b(\lambda)$ are the coefficients of spectral total absorption and spectral total backscattering, respectively. An interesting feature of this model (Lee et al., 2005b) is that it allows estimation of the attenuation coefficient for any wavelength with high accuracy, given the coefficients for $a(\lambda)$ and $b_b(\lambda)$ for any region-of-interest can be obtained with suitable accuracy. For our purpose, we obtained location- and time-specific estimates of $a(\lambda)$ and $b_b(\lambda)$ from the SWIM algorithm and implemented Eq. (6) for each pixel location within our test sites to obtain $K_d(\lambda)$. We note however, that the $K_d(\lambda)$ model above can use IOPs derived from other IOP algorithms and is hence not tied to the SWIM algorithm.

2.2.2 Integrating benthic irradiance within the PAR range

2.2.2.1 Instantaneous benthic PAR

Values of $bPAR_i$ were calculated by spectrally integrating the values of $E_b(\lambda)$ as:

$$bPAR_i = \int_{400}^{700} E_b(\lambda)d\lambda. \qquad (7)$$

Note that the spectral range (as further detailed later) is not continuous and corresponds to the MODIS AQUA ocean colour band centers. The integration was performed in Python 3.6.3 using the numerical python (numpy) library's "trapz" function that implements the trapezoidal method to numerically approximate the area under the curve using definite integral over discrete intervals (i.e., here defined by the band centers of MODIS AQUA).

2.2.2.2 Daily integrated benthic PAR

To obtain $bPAR_d$ from sunrise to sunset for any given day and pixel location, we first estimated the instantaneous benthic PAR at noon, $bPAR_n$ (μmol photons m^{-2} s^{-1}), which gives the maximum potential PAR irradiance at the seafloor, using:

$$bPAR_n = \int_{400}^{700} \left(t_g E_d^{0^+}(\lambda)\right) e^{-K_d(\lambda)z} d\lambda \qquad (8)$$

where $E_d^{0^+} = F_0 * T * \cos(\theta'_{solz}(\phi))$ following Kumar et al. (1997) and $\theta'_{solz}(\phi)$ is solar zenith angle at a given time between sunrise to noon at each hour angle ϕ. Assuming clear skies (i.e., no clouds) and that the cloud/sky system is non-reflecting and non-absorbing, the magnitude of $E_d^{0^+}(\lambda, \theta'_{solz}(\phi))$ can be estimated as a function of θ_{solz} and is approximately sinusoidal in relation to the daylight hours and symmetric about noon (Kirk, 2011). Further, we can compute the solar zenith angle for a given solar hour angle, ϕ, as:

$$\theta'_{solz}(\phi) = \cos^{-1}\left(\sin(lat)\sin(\delta) + \cos(lat)\cos(\delta)\cos(\phi)\right) \qquad (9)$$

where, for a given pixel on a single day latitude, *lat* (radians), the solar declination angle, δ (radians) is computed as:

$$\begin{aligned}\delta = {} & 0.006918 - 0.399912\cos(\gamma) + \\ & 0.070257\sin(\gamma) - 0.006758\cos(2\gamma) + \\ & 0.000907\sin(2\gamma) - 0.002697\cos(3\gamma) + 0.00148\sin(3\gamma)\end{aligned} \quad . \qquad (10)$$

The term γ (radians) is the date expressed as an angle:

$$\gamma = \frac{2\pi}{365} * (jday - 1) \qquad (11)$$

where *jday* is the Julian day (0-365 in regular year, or 0-366 in leap year).

Thus, $bPAR_d$ can be expressed as the double integral:

$$bPAR_d = 2 * \int_{\phi_{rise}}^{\phi_{noon}} \int_{400}^{700} \left(t_g E_d^{0^+}(\lambda, \theta'_{solz}(\phi)) \right) e^{-K_d(\lambda) z} \, d\phi \, d\lambda \qquad (12)$$

where ϕ_{rise} and ϕ_{noon} = 0 denote hour angles at sunrise and noon, respectively. The integral with respect to solar hour angle in Eq. (12) is computed numerically using a trapezoidal rule by discretizing the solution into fifty ϕ steps ranging from ϕ_{rise} to ϕ_{noon} = 0, where ϕ_{rise} is computed as:

$$\phi_{rise} = \cos^{-1}\left(-\tan(\delta)\tan(lat)\right). \qquad (13)$$

2.3 Data and model evaluation

2.3.1 Satellite data processing

MODIS AQUA raw Level-1A (L1A) data files spanning 2002 – 2018 were downloaded from NASA (https://oceancolor.gsfc.nasa.gov/) and spatially subsetted to encompass four test sites within the GBR (black filled circles in Figure 2). These data files were then processed to geophysical Level-2 (L2) data products using NASA's Ocean Color Software Suite (OCSSW) processing code that is distributed as part of the SeaDAS display and analysis software package (NASA). L2 data products were produced for ten visible MODIS AQUA bands centered on: 412, 443, 469, 488, 531, 547, 555, 645, 667, and 678 nm and stored in NetCDF4 files. These L2 data products included: $E_d^{0^+}(\lambda, \theta'_{solz}(\phi))$, θ_{solz}, and SWIM-derived IOPs, $a(\lambda)$ and $b_b(\lambda)$. NASA's standard ocean colour atmospheric correction was used to produce all L2 data products (Ahmad et al., 2010; Bailey et al., 2010; Siegel et al., 2000). The data processing yielded nearly 5500 daily MODIS AQUA L2 files for each of the four test sites.

2.3.2 GBR bathymetry data

Bathymetric data used to define the water column depth (datum: mean sea level (MSL)) were extracted from a gridded high-resolution bathymetry and digital elevation model (DEM) of the GBR, 3D-GBR (Beaman, 2010). This DEM dataset has a grid pixel resolution of ~100 m x 100 m that can resolve fine-scale details of the bottom topography of the GBR reefs and inter-reefal systems (see Figure 2). The full GBR bathymetric dataset is available from Australia's eAtlas website and environmental research data mapping and management system at https://eatlas.org.au/data/uuid/200aba6b-6fb6-443e-b84b-86b0bbdb53ac.

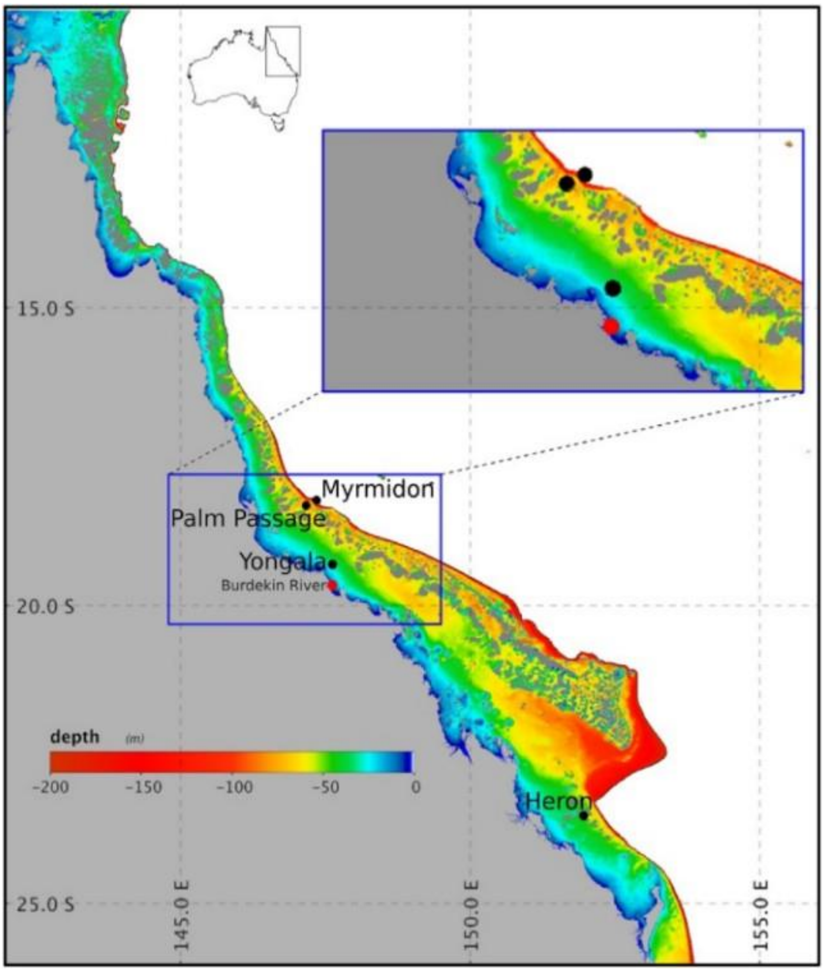

Figure 2: Location map of the four validation test sites (black filled circles) within the GBR region along the north eastern coast of Australia (inset map). The colour gradient indicates depth contours within the 200 m bathymetric shelf. The blue rectangle indicates the boundary of the small regional box, Burdekin region, used for temporal evaluation of the model (as detailed in section 3.6) with the corresponding subset bathymetry showing the complex topographic features in the model region. Red filled circle indicates location of the Burdekin River mouth while gray masked regions indicate land and coral reefs.

2.3.3 In situ data collection and processing

The Australian Integrated Marine Observing System (IMOS) maintains an array of observing sub-facilities (Rigby et al., 2014). One of the regional Shelf Mooring Array sub-facilities is located on the coast of Queensland, which is part of the Queensland IMOS (Q-IMOS) node established in 2007 and currently operated by the Australian Institute of Marine Science (AIMS). To conduct validation for this study, four existing mooring stations: Yongala, Palm Passage, Myrmidon, and Heron Island South (referred to as Heron throughout the manuscript) were expanded in 2015/2016 to also include PAR sensors, all located >1 km away from reefs and other geometrically shallow features (Table 1). These four mooring stations were therefore selected as *in situ* benthic PAR validation sites.

It is worth noting that the sites used for validation represent spatially and optically diverse water bodies. The Yongala mooring site is located midshelf with shallow lagoon waters often subject to wind-driven resuspension of bottom sediments and terrestrial influence. Hence, it encompasses both turbid and moderately clear seawater conditions and strong variation in optical properties (>20-fold range in PAR values). It is also exposed to seasonal runoff from the nearby Burdekin River. The Palm Passage and Myrmidon test sites are both located on the edge of the continental shelf, and although they are seasonally exposed to the influence of the East Australian Current (EAC), the southwest Pacific poleward western boundary current, these two stations most typically represent clear oceanic optical conditions (four- to six-fold range in PAR values), typical of oligotrophic waters. Meanwhile, the Heron station represents relatively stable intermediate in-water optical conditions (clarity and variability) although it may also be influenced by other important local oceanographic features (e.g., eddy-driven intrusion and productivity, tidally-driven flows, seasonal *Trichodesmium* blooms), yet not much more than the effects of the EAC oceanic intrusions experienced by the two deep oceanic test sites. Overall, the selected test regions comprise a range of optical water types within the GBR lagoon, and hence, suitable to test the capability of the newly developed benthic irradiance model over an optical dynamic range found in this region. A limitation of this validation, however, is that we have not included a nearshore *in situ* site. Nearshore GBR waters are more optically variable due to strong tidal and seasonal variations in water quality, which can be expected to result in greater error. The standard deviation around inherent optical properties has been found to be higher in the complex nearshore waters of the GBR. This, in combination with reflection from the bottom in optically shallow waters, has been found to reduce the accuracy of remote sensing data products in complex coastal environments (Blondeau-Patissier et al., 2009).

Table 1: IMOS mooring stations for *in situ* PAR data collection in the Great Barrier Reef.

IMOS Mooring station	Latitude (°S)	Longitude (°E)	Characteristics	Station depth (m)	Mean PAR logger depth (m)	Dates of deployment (inclusive)	No. of *in situ* data collected
Yongala	19.302	147.621	shallow inshore, periodically turbid	30	29	22 Mar 2015 to 26 Sep 2017	77,486
Heron	23.513	151.955	shallow mid-shelf, clear	46	24.5	03 Apr 2016 to 04 Oct 2017	248,849
Palm Passage	18.308	147.167	deep, outer shelf, clear oceanic	70	25	28 May 2016 to 22 Nov 2016	84,920
Myrmidon	18.220	147.344	deep, shelf edge, clear oceanic	192	19	25 May 2016 to 15 Nov 2017	145,859

To measure *in situ* benthic PAR at Yongala, a Seabird Scientific SBE16PLUS v2 SEACAT profiler with upward facing WETLabs Environmental Characterization Optics (ECO) PARSB sensor was deployed 0.5 m above the bottom substrate at ~30 m water depth. At the other three mooring sites, WETLabs ECO PARSB sensors were clamp-mounted to a permanent mooring wire at a fixed distance from the seafloor at each deployment period.

PAR sensors collected 5-second data bursts every 15 minutes (480 benthic PAR records per day) at all stations except Yongala where single measurements were collected every 15 minutes (96 benthic PAR records per day). Deployments and servicing of sensors occurred approximately every six months. After each deployment period, data were downloaded and the instrument's optical component was checked, characterised and tested to ensure the quality and validity of the data between deployments. For each recovery period, the data was analysed and quality controlled such that: (i) data records from the beginning and end of each deployment were excluded to ensure that only stable PAR measurements were included in subsequent analysis or within a complete day cycle in the case of $bPAR_d$ validation, (ii) data points when instrument failure was experienced (e.g., battery problems) were also excluded (e.g., Palm Passage deployments 2 and 3), and (iii) night-time values were forced to zero by applying an offset based on the dark count readings of the sensor for each deployment period. Table 1 lists the deployment details and total number of *in situ* PAR data remaining after quality controls were applied.

2.3.4 Algorithm validation approach

The model performance was evaluated via matchups between: (i) concurrent instantaneous parameters, $bPAR_i$ and *in situ* measured instantaneous PAR near the seafloor (Yongala) or in the water column (Myrmidon, Palm Passage and Heron), (ii) concurrent daily-integrated parameters, $bPAR_d$ and the daily-integrated *in situ* measurements, and (iii) all four test sites combined against overall satellite retrieval performance for both instantaneous and daily integrated cases.

For clarity, because the PAR loggers, except in Yongala, were mounted in mid-water rather than on the bottom, the model was also run for the depths that complemented the *in situ* data for each site and deployment period. Consequently, for brevity, we use the term 'benthic PAR' hereto for both PAR near the benthos (i.e., Yongala) or at specific water column depth (i.e., clamp-mounted logger depths at Palm Passage, Myrmidon and Heron).

2.3.4.1 Matchups of satellite-derived to in situ data pairs

For each L2 file containing results of the benthic irradiance model (either the instantaneous $bPAR_i$ and daily integrated $bPAR_d$) corresponding to an *in situ* measurement, satellite-derived values were extracted for a 3 x 3 pixel box centered at the mooring station locations (see Table 1 for coordinates). Next, image pixels were discarded if any of the pixels were associated with the following NASA L2 quality flags: LAND, CLDICE, HILT, HIGLINT and STRAYLIGHT (Robinson et al., 2003) for quality assurance. Extracted pixels were also discarded using two additional quality control procedures: (i) if any of the 9 pixels within the test box had been masked (Barnes et al., 2013), and (ii) if the coefficient of variation (CV, standard deviation/mean) between the nine pixels of the satellite-derived $bPAR_i$ or $bPAR_d$ was greater than 15%, indicating low intra-pixel stability of the modeled parameter over relevant time-scale (Seegers et al., 2018). Finally, common statistical parameters including minimum, maximum, mean, standard deviation, and median values were calculated for each nine-pixel box as a final check; however, we only reported and used median values in further analysis. Matchups between concurrent data pairs of satellite-derived and *in situ* measured *bPAR* were then performed using quality controlled median $bPAR_i$ (and $bPAR_d$) timeseries compared against the *in situ bPAR* timeseries. To qualify as 'concurrent', we included *in situ* data from ±3 hours around the MODIS AQUA satellite overpass time similar to previous studies (Bailey and Werdell, 2006). Matchups were conducted using R Studio (version 1.1.456) running R version 3.5.2 (R Core Team, 2019a) (codes available upon request).

2.3.4.2 Regression analysis and other performance metrics

Type-II linear regression analysis was used to compare the concurrent satellite-derived and *in situ* measured *bPAR* values per test site and on the combined dataset to assess how well the model performed over the dynamic range of benthic PAR in the GBR. The regression slope, intercept, and coefficient of determination (r^2) were calculated on $\log_{10}$-transformed data. Reduced major axis regression analysis was completed using lmodel2 package (Legendre, 2014) in R version 3.5.2. Model type II linear regression was chosen due to assumed inherent error in both the satellite and *in situ* datasets (e.g., because pixels from satellite imagery are not in exactly the same location and time as the *in situ* data, etc.). Lastly, additional metrics, including bias and mean absolute error (MAE), were calculated on $\log_{10}$-transformed data as measures of overall algorithm bias (i.e., systematic error) and accuracy (i.e., average model prediction error) that were back-transformed out of logarithmic scale before interpreting the results. Following Seegers et al. (2018), bias and MAE were calculated as:

$$bias = 10 \wedge \left(\frac{\sum_{i=1}^{n} \log_{10}(bPAR_{sat}) - \log_{10}(bPAR_{insitu})}{n} \right) \tag{14}$$

$$MAE = 10 \wedge \left(\frac{\sum_{i=1}^{n} |\log_{10}(bPAR_{sat}) - \log_{10}(bPAR_{insitu})|}{n} \right) \tag{15}$$

where $bPAR_{sat}$ is either $bPAR_i$ or $bPAR_d$, $bPAR_{insitu}$ is the corresponding *in situ* measured benthic PAR, and n is the number of observations. The resulting error metrics are in multiplicative space and dimensionless. As such, multiplicative bias values of 1.0 indicates no bias, and bias <1.0 denotes negative bias (e.g., underestimation of the observed values). Whilst for a multiplicative MAE, lower values (or closer to 1.0) would indicate better model performance.

2.3.4.3 Evaluation of model components: the diffuse attenuation model coefficients and spectral IOP-based approach ($K_d(\lambda)$ vs. $K_d(PAR)$)

It is worth noting that the $K_d(\lambda)$ model coefficients (0.005, 4.18, 0.52, and −10.18) in Eq. (6) were derived empirically from a dataset simulated with radiative transfer code (Lee et al., 2005b). These coefficients best estimate layer-averaged $K_d(\lambda)$ for the photic zone depth (i.e. the layer of water over which irradiance is diminished to 10% of surface incident values). Because we wish to estimate irradiance at the seafloor, the Lee et al. (2005b) $K_d(\lambda)$ model may be limited when the geometric depth is not equivalent to the photic depth. Hence, to evaluate the limitations of the $K_d(\lambda)$ model, we conducted a cursory comparison study for two optical scenarios: (i) 'oligotrophic' (chlorophyll-*a* concentration of 0.05 mg m^{-3}) and (ii) 'mesotrophic' (chlorophyll-a concentration of 0.5 mg m^{-3}); where the IOPs were known. We then compared layer-averaged $K_d(\lambda)$ values computed using the Lee et al. (2005b) model against the $K_d(\lambda)$ values more accurately simulated with Hydrolight-Ecolight 5.1 (HE5) radiative transfer code (Mobley, 1994). We used absolute percent difference (APD) as metric for this comparison. The radiative transfer modelling exercise we used followed the methodology described by McKinna et al. (2015) and considered four geometric depths (5, 10, 20, and 30 m), four θ_{solz} (10, 30, 50, and 80°) and used sand seafloor albedo for all simulations.

We next evaluated the skill of our spectrally-resolved $bPAR_i$ model and two other approaches based on the method of Morel et al. (2007). These alternative methods use K_d(PAR). In one model, K_d(PAR) is modelled as a function of known/derived chlorophyll-*a* pigment concentration. We refer to this as the "Chlorophyll-based" approach. In the other approach, K_d(PAR) is modelled as a function of known/derived K_d(490). We refer to this as the "K_d(490)-based" approach. Our spectrally-resolved $bPAR_i$ model is referred to as the "IOP-based" approach. In this case study we also used HES radiative transfer modelling to accurately simulate $bPAR_i$ values to which we could compare modelled $bPAR_i$. For this radiative transfer modelling exercise, a large set of synthesised IOPs were used as HE5 inputs and simulations were run over 14 depths (spanning 3 – 30 m), with fixed θ_{solz} = 30° and a sand seafloor albedo. These simulated data were generated by McKinna and Werdell (2018) and further details can be found therein. Also, note that we used a consistent value of t_g for transmitting surface irradiance values, either $E_d^{0^+}(l, q'_{solz}(f))$ or PAR, across the air-water interface. We note that for this radiative transfer study, model inputs for each of the three approaches (Chlorophyll-based, K_d(490)-based, and IOP-based) were taken directly from the radiative transfer simulation outputs (i.e., no satellite algorithms were employed in this brief case study).

2.3.4.4 Temporal evaluation

Performance metrics described above (see section 3.4.2) are robust indicators of the absolute accuracy of the model but do not provide additional information on temporal structure or variability of the parameter being considered against the validation dataset used. To assess whether the benthic irradiance model produces temporally stable estimates of benthic PAR (e.g., no unreasonable extreme values or unrealistic trends in the time series), we examined a regional box, the Burdekin region, within the central GBR that encompasses three of the four test sites considered in the study (inset map on Figure 2) by implementing the model to MODIS AQUA data from July 2002 to December 2018.

2.3.5 Simple depth sensitivity analysis

So far, we have used the MSL Beaman 3D-GBR bathymetry (Beaman, 2010) as a proxy for water- column depth. However, one of the possible sources of error of our benthic irradiance model could be driven by changes in water-column depth due to tidal fluctuations. The tides in the GBR are predominantly semidiurnal (tidal cycle with two high and two low tides of approximately equal size each lunar day) and with regional differences in maximum amplitudes ranging between 2.5 to 7 m (Hutchings et al., 2008). To assess the importance of correcting the water depth for tidal effects, we also conducted a *bPAR* model run using *in situ* depth (i.e., pressure data measured using seafloor-mounted SEABIRD SBE16 + V2 SEACAT CTD with pressure sensor at the Yongala site) as z in Eq. (1). The depth sensitivity analysis (DSA), thus compared two *bPAR* model parameterizations: (i) the original model using MSL Beaman 3D-GBR bathymetry referred to as "3D-GBR" model, and (ii) a model using *in situ* CTD depth measurements referred to as "*pressure"* model, to assess and evaluate differences, if any. As neither of these two model parameterizations was assumed initially superior, difference was quantified using unbiased percent difference (UPD) calculated as per (Barnes et al., 2013).

2.4 Results and discussion

Figure 3: Colours change with depth underwater as some wavelengths are attenuated more rapidly than others. Credit: Renata Ferrari.

2.4.1 Spectral IOP-based K_d model structure

Figure 4 and Figure 5 show the various layer-averaged $K_d(\lambda)$ spectra calculated for four different layer depths and two optical water scenarios. The solid lines in the upper panels of Figure 4 and Figure 5 respectively show the radiative transfer-modelled layer-averaged $K_d(\lambda)$ values for oligotrophic and mesotrophic optical scenarios, while the black dotted lines (also in upper panels of Figure 4 and Figure 5) show the model layer-averaged $K_d(\lambda)$ calculated via Eq. (6). For both examples, layer-averaged $K_d(\lambda)$ values for a given θ_{solz} are generally consistent with each other over the spectral range 400 – 600 nm, with the exception of the 30 m layer in the mesotrophic scenario. It can also be seen that as θ_{solz} increases, the magnitude of $K_d(\lambda)$ also increases slightly whilst the shapes stay much the same. Plots of APD show that the analytical $K_d(\lambda)$ model typically agrees to within 10% of radiative transfer values over 400 – 600 nm. We note that for the 30 m depth mesotrophic scenario, radiative transfer-simulated $K_d(\lambda)$ consistently deviates from the model of Lee et al. (2005b) in both the blue (400 – 450 nm) and red regions (600 – 700 nm) for all solar zenith values.

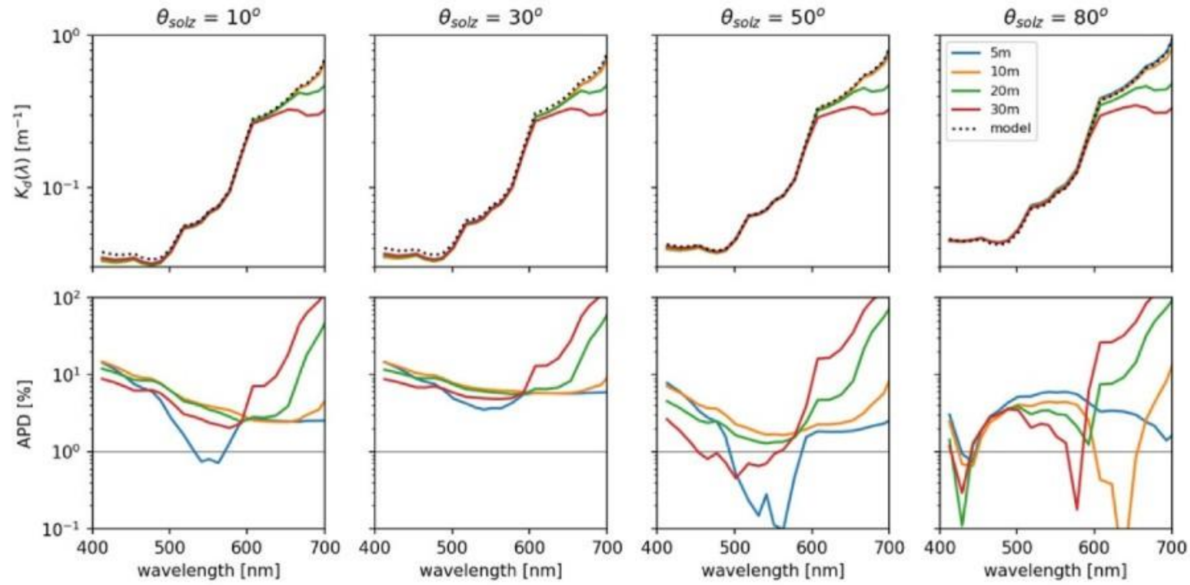

Figure 4: Top row: solid lines represent layer-averaged spectral diffuse attenuation coefficients for four different layer depths for an oligotrophic scenario. Blue, orange, green, and red lines correspond to layer depths of 5, 10, 20, and 30 m, respectively. The dashed line represents layer averaged spectral diffuse attenuation coefficient derived by the Lee et al. (2005b) model. Each panel (left-to-right) corresponds to four solar zenith angles (10, 30, 50, and 80°). Bottom row: absolute percent difference (APD) between radiative transfer modelled layer-averaged spectral diffuse attenuation coefficients and values estimated using the Lee et al. (2005b) model. The horizontal gray line represents 1% APD.

This brief analysis, whilst not exhaustive, nonetheless provides some confidence that the Lee et al. (2005b) model, although tuned for the photic depth layer, can estimate $K_d(\lambda)$ to within 10% of true values over a range of geometric depths. Indeed, this model for $K_d(\lambda)$ has been previously tested in optically shallow coral reef waters of the West Florida Shelf by Barnes et al. (2013). Using *in situ* validation data, Barnes et al. (2013) showed the Lee et al. (2005b) model had good skill at estimating $K_d(\lambda)$ at wavelengths shorter than 500 nm, which is consistent with this cursory case study.

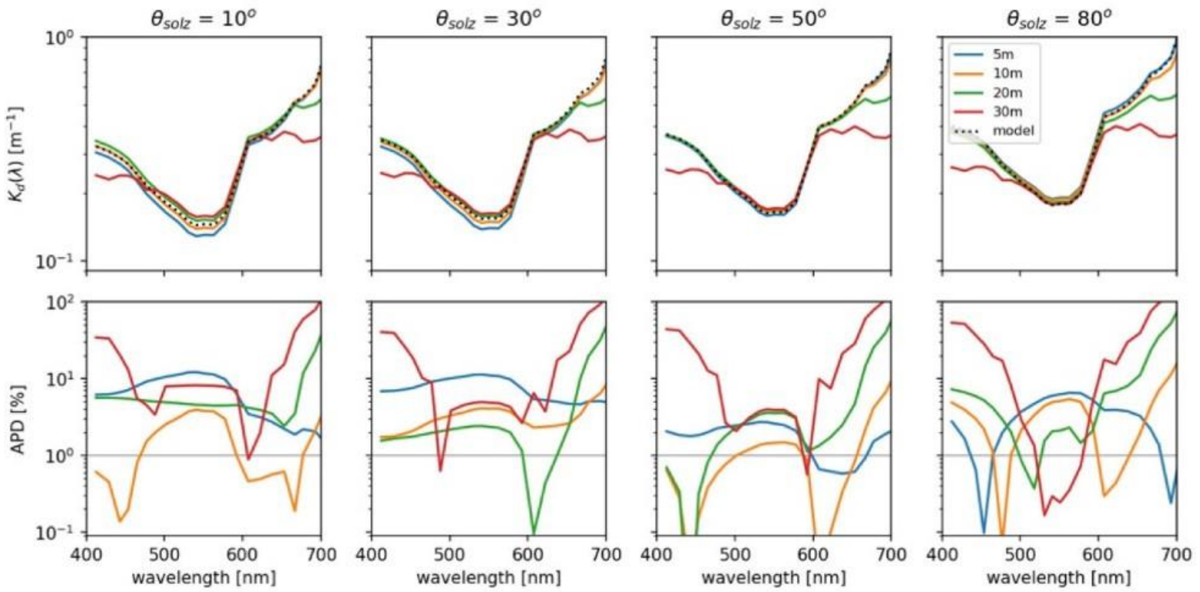

Figure 5: Top row: solid lines represent layer-averaged spectral diffuse attenuation coefficients for four different layer depths for a mesotrophic scenario. Blue, orange, green, and red lines correspond to layer depths of 5, 10, 20, and 30 m, respectively. The dashed line represents layer averaged spectral diffuse attenuation coefficient derived by the Lee et al. (2005b) model. Each panel (left-to-right) corresponds to four solar zenith angles (10, 30, 50, and 80°). Bottom row: absolute percent difference (APD) between radiative transfer modelled layer-averaged spectral diffuse attenuation coefficients and values estimated using the Lee et al. (2005b) model. The horizontal gray line represents 1% APD.

Figure 6 shows scatter plots comparing modelled $bPAR_i$ with values computed from radiative transfer simulations. The results show that the IOP-based model derives $bPAR_i$ with root mean square error (RMSE) and mean bias statistics that are better than the Chlorophyll- based and K_d(490)-based methods. Thus, this brief analysis demonstrates the benefit of using our spectrally resolved $K_d(\lambda)$-based model as opposed to a K_d(PAR)-based methods when estimating $bPAR_i$.

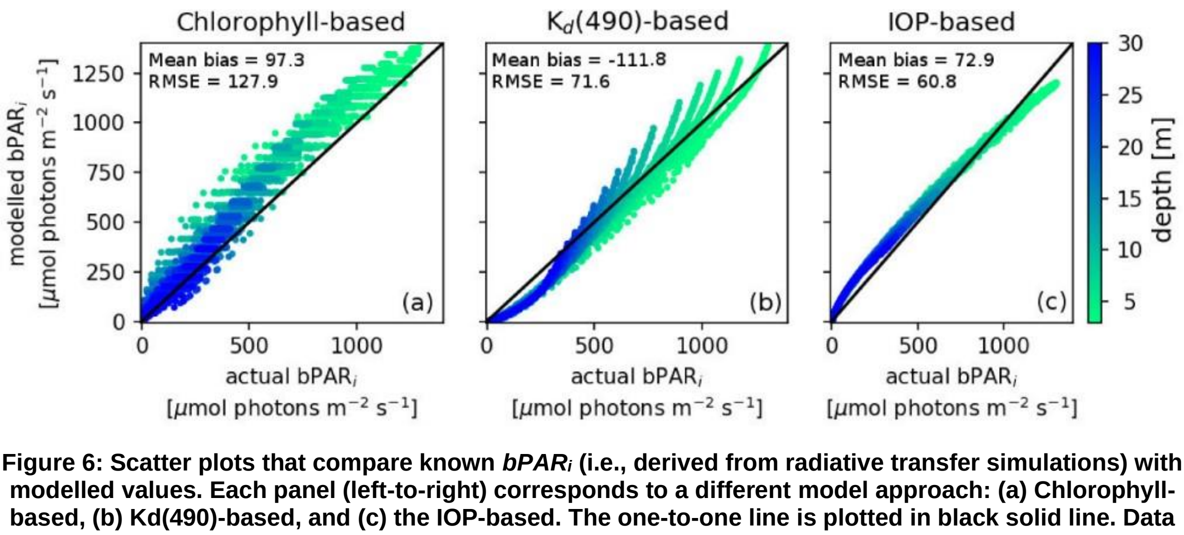

Figure 6: Scatter plots that compare known *$bPAR_i$* (i.e., derived from radiative transfer simulations) with modelled values. Each panel (left-to-right) corresponds to a different model approach: (a) Chlorophyll-based, (b) Kd(490)-based, and (c) the IOP-based. The one-to-one line is plotted in black solid line. Data points are colour coded by geometric depth. Highest values of *$bPAR_i$* typically occur in shallow waters less than 5 m in depth. For our radiative transfer simulations, incident surface PAR values were 1679 μmol photons m^{-2} s^{-1}.

2.4.2 Instantaneous benthic PAR matchup analysis

We acquired 1134 matchup pairs (i.e., days of observations) between satellite-derived $bPAR_i$ and *in situ* measured data across the test sites when only the L2 quality flags were used as exclusion criterion (Table 2). After the application of the two additional exclusion criteria (i.e., adjacent to a masked pixel in the 3 x 3 pixel box and CV > 0.15), 696 data pairs remained. These quality-controlled data pairs comprised the dataset that was subsequently used in the regression analysis. The highest number of valid concurrent data pairs were found for Yongala and Heron, with 348 and 210 days of observations considered for the matchups, respectively. Palm Passage had the lowest number of valid concurrent data pairs at 45 days, as this test site had only one deployment period with good data because of *in situ* instrument failures experienced during the other deployment periods. Consequently, the number of concurrent matchups between the test sites varied by almost a factor of eight between sites with the most and the least data pairs. Nevertheless, across all test sites, only high-quality concurrent data pairs were included in the validation analyses, hence, the veracity of the model performance evaluation should not be diminished.

By way of comparison, NASA's chlorophyll-a data product, considered to be a climate quality dataset for the global ocean, has a total number of 958 high quality matchups for the entire MODIS Aqau missions span (2002 – present). In shelf waters (depth < 200 m), NASA's chlorophyll-a algorithm has N=689 high quality matchups with mean absolute bias and mean absolute errors or 1.18374 and 1.67532, respectively (computed in log-transform space).

In situ measurements of instantaneous benthic PAR varied by almost two orders of magnitude ranging from 13 to 906 µmol m^{-2} s^{-1}, indicating that the validation dataset spanned a wide range of environmental conditions (Table 2). The satellite-derived $bPAR_i$ values showed comparable magnitudes spanning 22 to 672 µmol m^{-2} s^{-1}. Despite the wide range of inherent optical diversity across the test regions, regression analyses showed strong agreement between concurrent satellite-derived and *in situ bPAR* data pairs (Figure 8, Table 2), indicating that our approach was able to produce realistic estimate of *bPAR* values across a range of complex and optically shallow coastal waters. The model performed strongest at Heron and was only slightly weaker at Yongala and the two deep oceanic test sites, Palm Passage and Myrmidon. Yongala and Heron had smaller dynamic ranges of benthic PAR over the period of observation compared to Palm Passage and Myrmidon and may somewhat explain the better agreement found in the two former test sites.

Note that the capability of our newly developed benthic irradiance model may be limited under certain environmental conditions. For example, tropical cyclones can lead to extreme optical conditions via mixing and re-suspension of near bottom sediments which might not be fully captured by remotely sensed datasets. Excessive rainfall events during the wet season can also cause major flooding of river catchments (Devlin et al., 2012). During such events, freshwater plumes discharge from rivers and disperse outward across the GBR lagoon, leading to distinct stratification in near-shore regions. Buoyant freshwater flood plumes are typically NAP- and CDOM-laden, thus the water column becomes optically inhomogeneous and the *bPAR* model's assumption of vertically homogenous IOPs is violated.

Table 2: Matchup statistics for instantaneous satellite-derived (*bPAR$_i$*) and concurrent in situ bPAR observations for the four test sites and all sites combined (denoted as ALL). The number of concurrent valid data pairs (days of observation) after all quality criteria were applied and used in regression analyses is indicated as n. The number of valid data points when only the L2 flags were used as the exclusion criterion is given by (n0), shown to emphasise the importance of additional exclusion criteria as described in section 3.4.1. The highlighted row for Yongala indicate matchup statistics when extremely low *bPAR* values (coinciding with a severe tropical cyclone that passed across the Queensland coast in late March 2017) were included in the regression analysis. Note that model performance metrics are in multiplicative-space, while range of concurrent satellite-derived and *in situ* PAR values are given in the observed (non-transformed) scale to facilitate interpretation.

Site	**n (n_0)**	PAR range (μmol photons m^{-2} s^{-1})		Model II regression			**bias**	**MAE**
		in situ	***bPAR$_i$***	**r^2**	**slope**	**intercept**		
Yongala	348 (523)	13.1, 247.3	21.9, 274.0	0.71	0.90	0.25	1.15	1.26
Heron	210 (320)	25.4, 288.8	26.5, 283.6	0.73	1.10	-0.23	0.95	1.22
Palm Passage	45 (81)	80.2, 353.6	54.6, 332.4	0.68	1.18	-0.49	0.82	1.31
Myrmidon	93 (210)	146.7, 906.1	102.2, 672.1	0.66	1.08	-0.26	0.88	1.26
ALL	696 (1134)	13.1, 906.1	21.9, 672.1	0.80	0.91	0.19	1.03	1.25
Yongala	353	1.1, 247.3	8.0, 274.0	0.73	0.83	0.41	1.18	1.28

The *bPAR* model's limitation under optically extreme conditions can be seen at the Yongala test site during early April 2017 when several extremely low *in situ bPAR* values (filled triangles in Figure 8 (a), (c), and (f)) resulted in a weaker overall agreement between the derived and actual measurements (i.e., lower slope = 0.83 and higher intercept = 0.41, hence less unity, but high r^2 = 0.73) (see last row of Table 2). The *in situ bPAR* values, the minimum of which were an order of magnitude smaller than satellite-derived values during this extreme event period, coincided with Tropical Cyclone Debbie that affected the Queensland coast in late March 2017 (BOM, 2018) and led to low water clarity (due to high terrestrial river runoff) in the vicinity of the Yongala site long after the event (Fabricius et al., 2016a). In Figure 8 (a), wet season (colour-coded red) validation data for the Yongala site, which is seasonally dominated by the Buderkin River plume, were biased slightly high; again suggesting that the *bPAR* model is underperforming during optically challenging events. Although the scope of the current study did not allow to further explore this limitation, an additional investigation is warranted.

Further analysis conducted on the combined dataset also echoed the overall strong agreement between derived and *in situ* measured *bPAR* values (Figure 8, right hand side, Table 2). Across all test sites, the calculated bias was small and ranged between 0.82 (–18%) at Palm Passage to 1.15 (+15%) at Yongala which respectively suggest an underestimation and overestimation of the observed PAR values by an average of ±16.5%. MAE values were very similar for all four test sites. Again, Heron had the smallest MAE of 1.22 while Palm Passage had the highest MAE of 1.31 indicating an average error of satellite-derived *bPAR$_i$* ranging between 22% to 31%, respectively. The overall model error of the combined satellite-derived *bPAR$_i$* values was about 25% (ALL dataset MAE = 1.25). This average model prediction error is much smaller and well within the 35% uncertainty and accuracy goal set for the retrievals of chlorophyll-a concentration which is a widely-used ocean colour variable ((Hooker and Esaias, 1993) as mentioned in (Barnes et al., 2014; McClain et al., 2004)).

Figure 7: Sun glint at the surface of the water. Credit: Grace Frank.

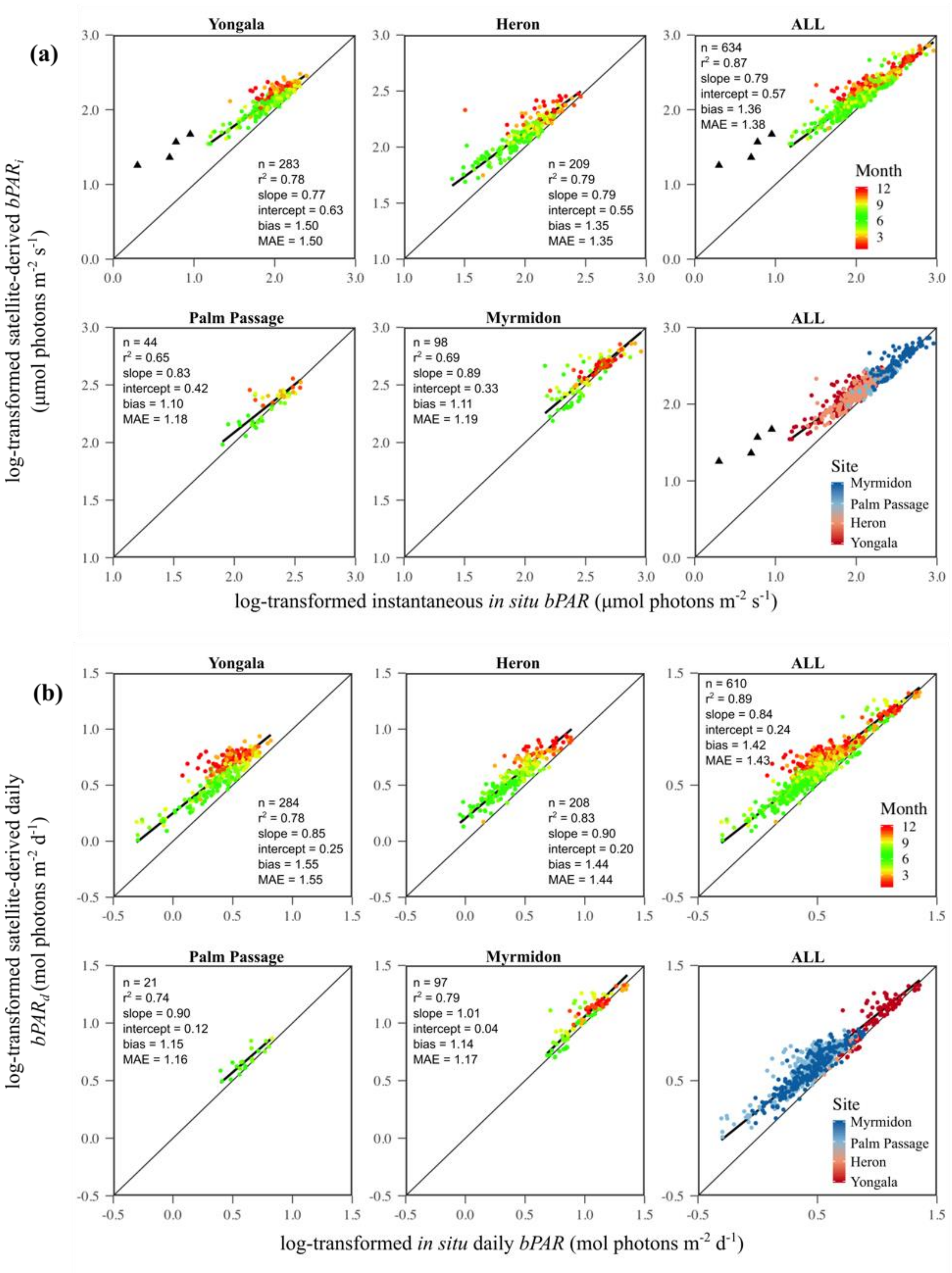

Figure 8: (a) Scatterplots of concurrent log-transformed satellite-derived instantaneous benthic PAR (*$bPAR_i$*) and *in situ bPAR* at four test sites (Yongala, Heron, Palm Passage, and Myrmidon). The red-yellow-green-magenta colour scale represents month of observation. The scatterplot labelled 'ALL' indicates combined observations from all test sites, plotted according to observation site (red to blue colour scale). Filled black triangles indicate values considered as outliers due to an extreme weather event experienced in the Yongala study site, which was excluded from the analysis (as previously reported). (b) The same as for (a) except log-log scaled scatterplots are of satellite-derived daily-integrated benthic PAR (*$bPAR_d$*) vs. *in situ* daily *bPAR*.

Collective consideration of the bias and MAE suggest agreement between satellite-derived $bPAR_i$ and *in situ* was best at the optically variable site Heron where many validation points existed, and lowest at the optically clear-water sites Palm Passage and Myrmidon, where relatively fewer data points were available. Given the overall strong agreement and small error of the derived values, we suggest that the larger error noted in Palm Passage and Myrmidon was more related to the quality of the *in situ* validation datasets and/or possibly related to fewer data points resulting in higher variability in the regression statistics rather than to a diminished ability of the model in these water bodies.

Table 3: Matchup statistics for daily integrated satellite-derived (*bPAR_d*) and concurrent *in situ bPAR* observations. The number of concurrent valid data points (days of observation) after all quality criteria were applied and which were used in regression analyses is indicated as n. Note that model performance and error metrics are in multiplicative-space, while range of *bPAR* values are given in the observed scale to facilitate interpretation.

Site	n	PAR range (mol photons m^{-2} d^{-1})		Model II regression			bias	MAE
		in situ	***bPAR_d***	r^2	**slope**	**intercept**		
Yongala	347	0.4, 6.6	0.6, 6.9	0.65	0.98	0.06	1.13	1.26
Heron	208	0.9, 7.7	0.8, 7.2	0.80	1.16	-0.09	0.96	1.21
Palm Passage	21	2.5, 6.7	1.9, 5.3	0.73	1.08	-0.18	0.75	1.35
Myrmidon	90	4.8, 22.7	3.1, 17.1	0.75	1.21	-0.29	0.83	1.28
ALL	666	0.4, 22.7	0.6, 17.1	0.80	0.94	0.04	1.01	1.25

2.4.3 Daily integrated benthic PAR matchup analysis

The same *in situ* validation datasets used for the instantaneous matchup analysis were integrated to obtain daily *in situ* benthic PAR values and compared with concurrent satellite-derived *bPAR_d*. The dynamic range of the *in situ* and satellite-derived daily values were comparable at 0.4 to 23 mol photons m^{-2} d^{-1} and 0.6 to 17 mol photons m^{-2} d^{-1}, respectively. Results of the Type II linear regression analysis on the daily integrated datasets also showed an overall strong positive relationship (Figure 9, Table 3). Again, agreement between derived and *in situ* values is most notable at the Heron test site with small negative bias (–4%) and highest accuracy (smallest MAE of 21%). Although Yongala showed a relatively lower coefficient of determination ($r^2 = 0.65$) amongst the test sites, the other regression statistics as well as bias and accuracy metrics indicate better model performance compared to the two deep test sites.

As previously discussed, relatively weaker agreement between the satellite-derived and the *in situ* data at Yongala may be attributed to our *bPAR* model underperforming under more complex and/or stratified in-water optical conditions in this shallow inshore test site. More specifically, this effect may be compounded when estimating daily-integrated PAR due to intra-daily temporal variability in physical factors that drive nearshore IOPs. For example, clear water, offshore pixels will have optical variability that occurs at longer time-scales, being distant from terrestrial sources of particles and other pollutants, such that temporally extrapolating the IOPs derived at the time of the MODIS AQUA satellite overpass for the whole day, is a reasonable assumption and one that indeed showed strong agreement with observed values. However, for more dynamic inshore waters that may have IOPs with variability occurring at shorter time-scales or higher frequency (e.g., hours), it becomes more challenging to temporally extrapolate the IOPs over the whole day. On the other hand, while the agreement between satellite-derived and *in situ* values was strong for the deep oceanic test sites, the bias and MAE at Yongala showed better results than at Palm Passage or Myrmidon. Again, we suggest that these results may be related to the quality of the validation data obtained for these test sites. As for the combined dataset, satellite retrievals showed strong positive agreement with an almost negligible systematic error (bias of +1%) and high accuracy (low MAE of 25%) (see Figure 8, right hand side and Table 3).

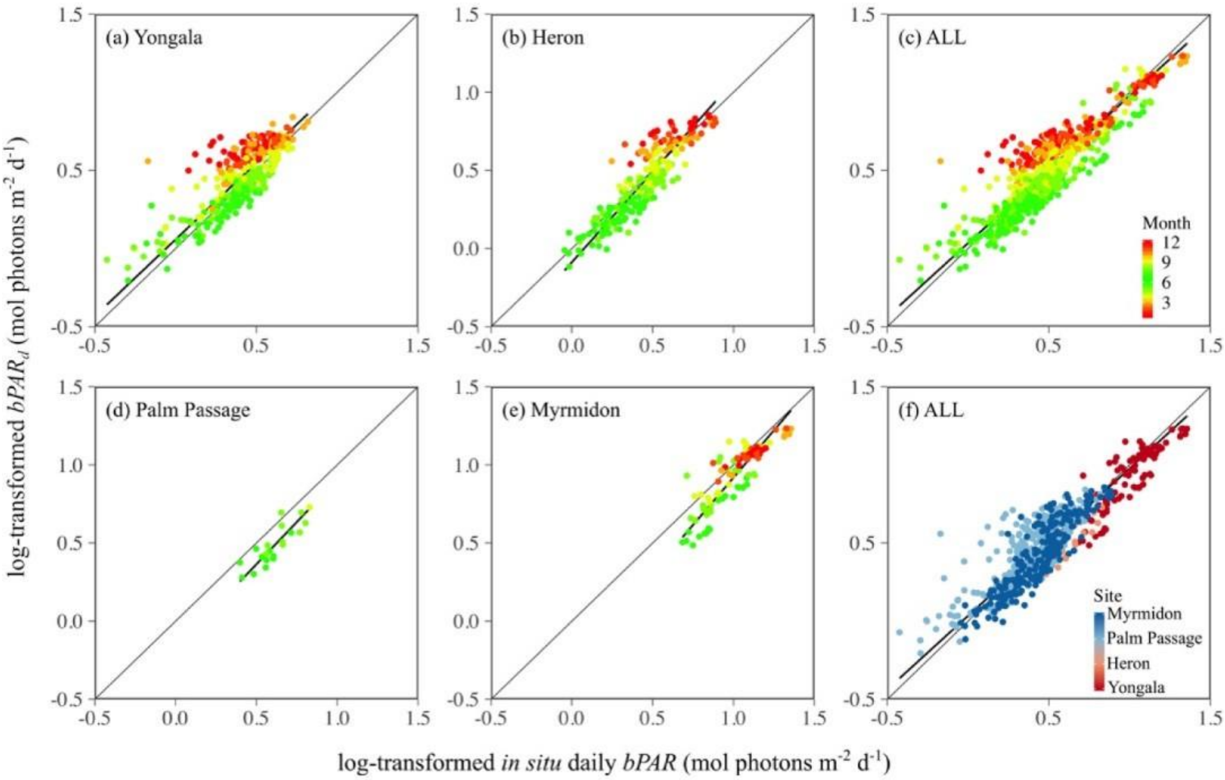

Figure 9: Scatterplots of concurrent log-transformed daily integrated satellite-derived (*$bPAR_d$*) and *in situ bPAR* for the four test regions of varying optical properties (a-b, d-e) plotted according to month of observation, and ALL sites combined plotted (c) by month of observation and (f) according to site. Colour scale gradient for the months of observations are defined to delineate seasonal contrast between austral wet (November to April of following calendar year, yellow-red) and austral dry (May to October, green) seasons. The thin and thick black solid lines indicate the 1:1 line and the reduced major axis regression slope, respectively.

Although we consider $bPAR_d$ to be an ecologically important parameter due to its role as an autotrophic requirement (e.g., energy source for photosynthesis), we also acknowledge that perhaps a more complete measure of light relevant for marine photosynthetic organisms is a PAR value estimated from the scalar irradiance (Kirk, 2011; Mobley, 1994) wherein light in every direction is considered (e.g., PAR measured by a spherical collector). However, as discussed earlier, the available validation dataset for this study is only collected for visible light measured on a plane (i.e., plane irradiance) which allowed us to only consider the downwelling plane irradiance in our model development. Indeed, if *in situ* scalar irradiance data becomes available in the future, this potential improvement could be considered.

While we acknowledge that our approach has several limitations and has room for further improvement (including cloud correction and quantification of error in optically complex nearshore waters), the baseline results obtained via this newly developed approach have demonstrated that our simple model can realistically estimate daily benthic PAR values within the GBR with skill exceeding that obtained for standard NASA Level 2 products such as chlorophyll *a*, at least in the Midshelf sites for which *in situ* PAR observations were obtained. Our new GBR-specific ocean colour benthic irradiance algorithm can thus be used for ecological studies within this important and world-heritage listed region by providing estimates of benthic light values.

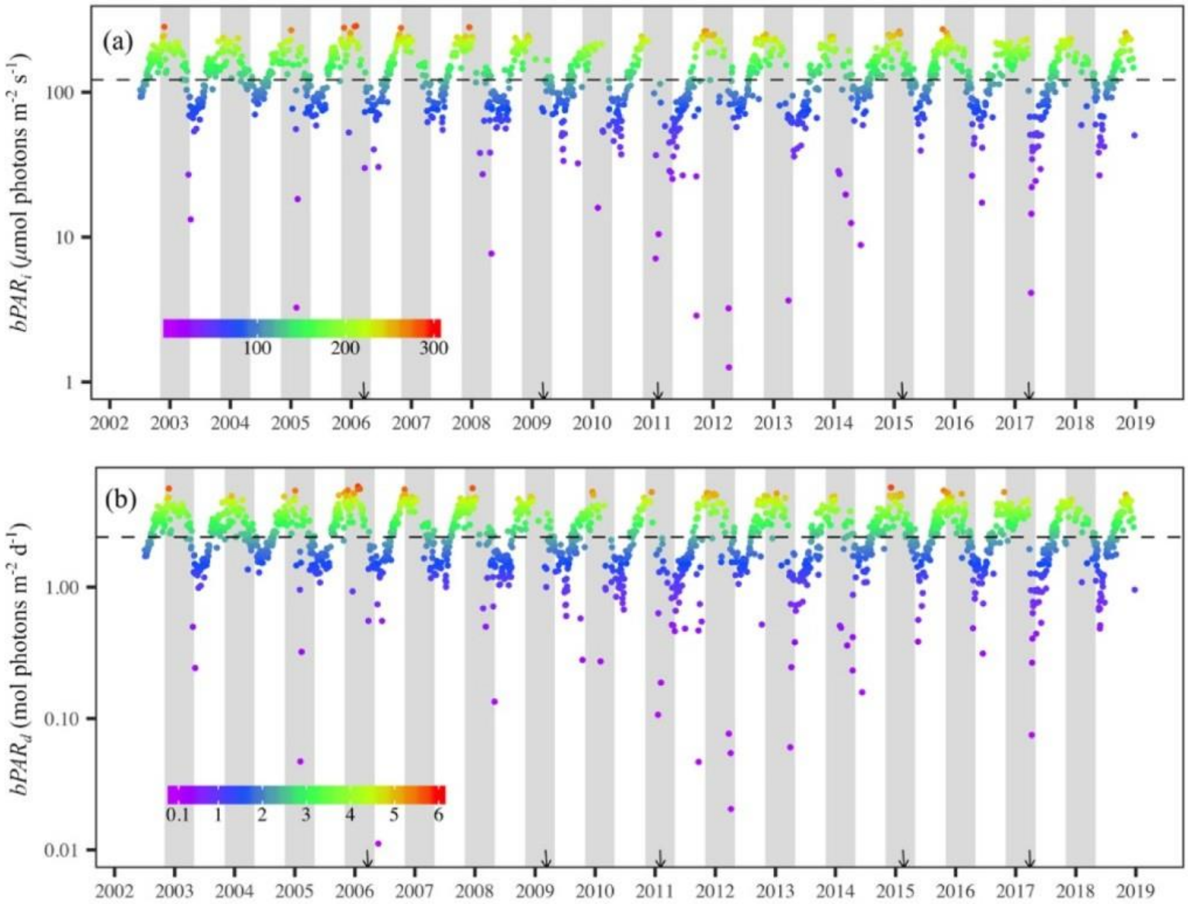

Figure 10: Timeseries plot of satellite-derived (a) instantaneous benthic PAR, *$bPAR_i$*, and (b) daily integrated benthic PAR, *$bPAR_d$*, for the Yongala test region from July 2002 to December 2018. The colour gradient indicate *bPAR* values while dashed horizontal line indicate the median value of the entire time series data for each parameter, overlaid for reference. The greyed-out areas indicate the austral wet season months (extending from November to April of following calendar year). Downward pointed black arrows on the x-axes denote occurrences of selected severe tropical cyclones that hit the eastern Australian coast. Note that vertical axes are in logarithmic scale.

2.4.4 Time series case study

The 16+ year time-series of satellite-derived benthic PAR values for the Yongala site exhibits strong seasonality (Figure 10). Lower values (purple to blue spots below the median lines) coincide at the end of austral wet season months (which extends from November to April the following calendar year, denoted as grey areas on both panels of Figure 10) and beginning of austral dry season (May to October). Relatively higher values (green to red spots above the median lines) were derived for most of the austral dry season towards the proper austral wet season. This temporal pattern agrees with the variability of satellite-derived photic depth data previously obtained for GBR (Weeks et al., 2012). This time-series provides insight into the influence of local events or phenomena that can drive variability of the underwater light field. As an example, decreased benthic light values are seen to coincide with tropical cyclones events (downward arrows in Figure 10). Indeed, the future near-synoptic, high-temporal resolution output of this model, which will be the first of its kind for the GBR, will provide a critical dataset that will allow us to further explore and understand how light availability varies both in space and time and in relation to the presence of important benthic organisms that is found within the GBR.

Figure 11 shows another view of the same data, with daily *bPAR* overlain on daily discharge from the Burdekin River (Queensland gauging station 120006B). Low *bPAR* values consistently follow periods of high discharge.

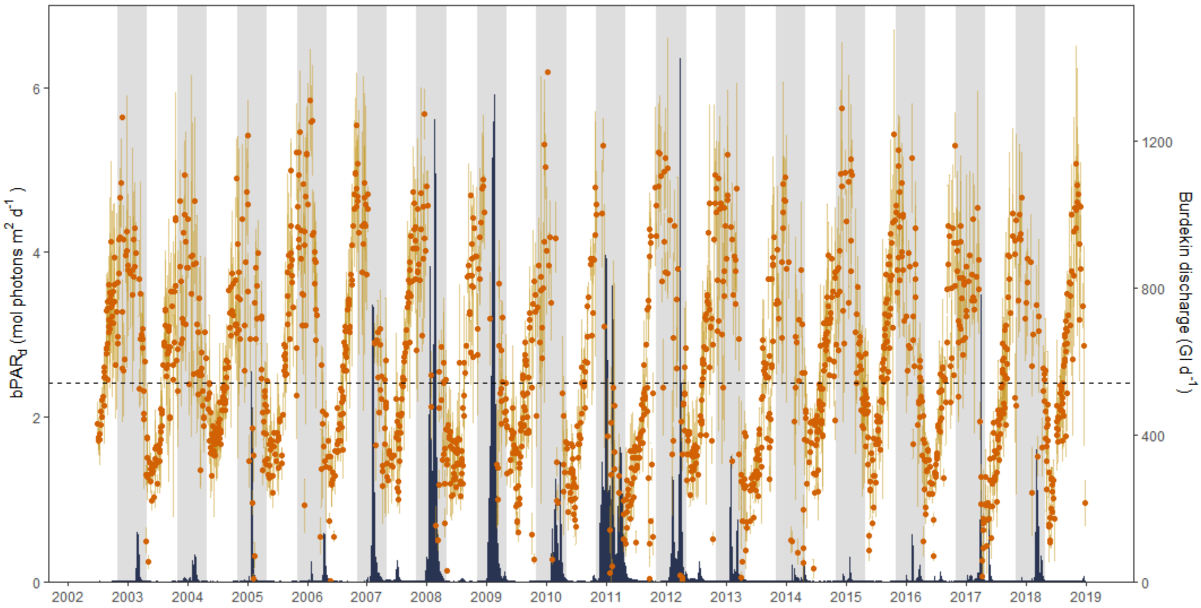

Figure 11: Timeseries plot of satellite-derived daily integrated benthic PAR, *bPAR$_d$*, for the Yongala test region from July 2002 to December 2018. Error bars indicate the standard deviation of bPAR over the 9-pixel box around the site location while the dashed horizontal line indicate the median value of the entire time series data for each parameter, overlaid for reference. The greyed-out areas indicate the austral wet season months (extending from November to April of following calendar year). Daily discharge from the Burdekin River is shown in navy blue.

2.4.4.1 Understanding the effects of tide on instantaneous benthic PAR estimates

Both “3D-GBR” and “*pressure*” models show good temporal coincidence with the observed instantaneous benthic PAR values (Figure 12 (a) and (b)). For the purpose of this exercise, a large difference between the satellite-derived *bPAR$_i$* values (for either model) would mean it is necessary to correct the original 3D-GBR bathymetry data for tidal effects. Otherwise, we can reasonably assume minimal tidal influence in the results of our new benthic irradiance model, but sentient of caveats when interpreting results.

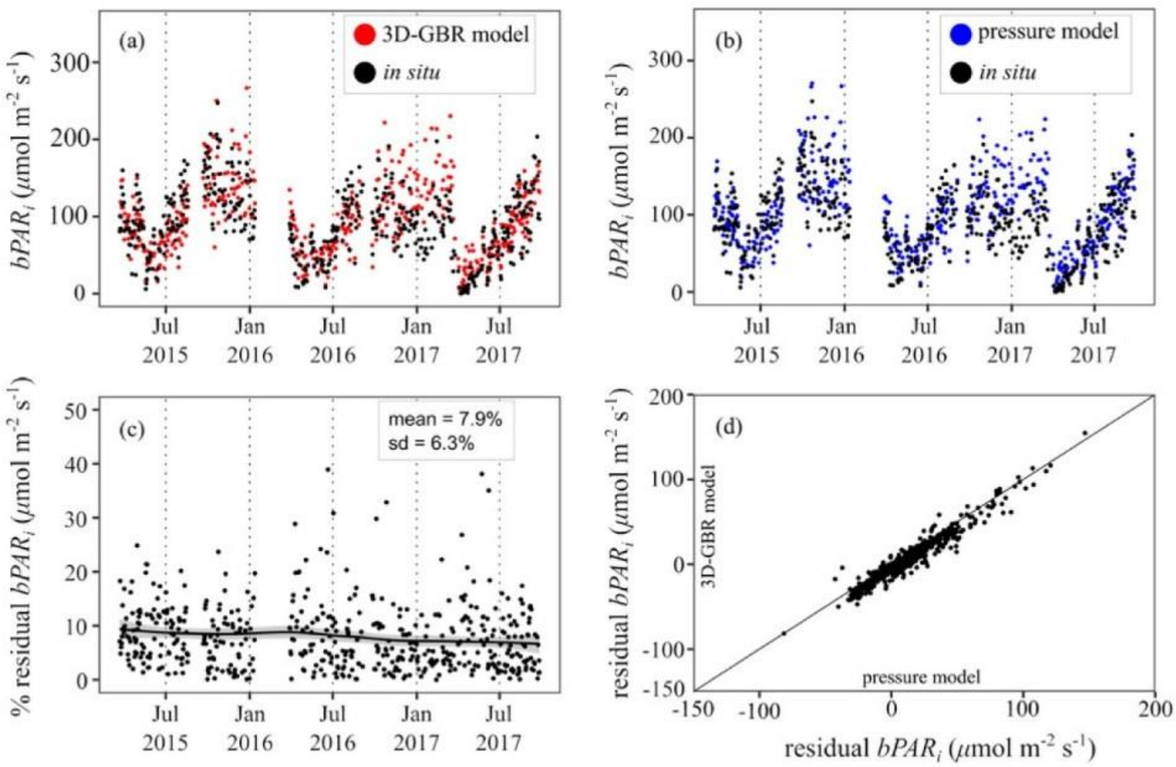

Figure 12: Depth sensitivity analysis and model results comparison at the Yongala test site. (a) plot of satellite-derived instantaneous benthic PAR values modeled using Beaman 3D-GBR bathymetry as z (red, 3D-GBR model) with *in situ* instantaneous benthic PAR (black); (b) plot of satellite-derived instantaneous benthic PAR values modeled using in situ pressure data as z (blue, pressure model) with in situ instantaneous benthic PAR (black); (c) unbiased percent difference between bPARi, calculated as: $|(bPAR_{3D\text{-}GBR} - bPAR_{pressure})|/(0.5*bPAR_{3D\text{-}GBR} + 0.5*bPARpressure)*100$; and (d) scatterplot of the residuals (against *in situ* values) of the two models where diagonal black solid line denotes the 1:1 line. Gaps in plots a-c indicate periods where there were no in situ data available for validation.

The comparison showed a mean UPD of 7.9% between the two models, equivalent to ~7 μmol photons m^{-2} s^{-1} (roughly 0.6 mol photons m^{-2} d^{-1}) (Figure 12(c)). Scatterplot of residuals between the two satellite-derived $bPAR_i$ values against *in situ* values (Figure 12 (d)) also show good agreement. This difference is relatively small compared to published ecologically-relevant minimum irradiance value required to maintain autotrophic health, which depending on the benthic organisms considered may vary between 0.4 to 5.1 mol photons m^{-2} d^{-1} (Gattuso et al., 2006). We concede that the tidal influence will vary depending on a location's known bathymetry and range of daily tidal fluctuations such that effects will be greater in areas with shallow depths and bigger tides. We note, however, that our model does not consider intertidal regions of the GBR or locations where MSL bathymetry is less than 5 m and where influence of the bottom can be significant (Barnes et al., 2013).

2.5 Conclusion

Here we have demonstrated that our simple benthic irradiance model can be employed to estimate realistic benthic PAR values within the GBR with good accuracy in Midshelf waters. We emphasize once again that although our results were reported in terms of a single broadband PAR irradiance, our approach does not use K_d(PAR). Instead, our model resolved $K_d(\lambda)$ by carrying out all calculations spectrally, where the full spectral variability of $E_b(\lambda)$ in Eq. (1) has been retained in the process. Thus, aside from its simplicity, the key strength and novelty to our benthic irradiance model mean it can be easily extended to other ocean colour sensors. In particular, we expect that model-derived estimates of *bPAR* may be improved when applied to data collected by sensors with contiguous spectral bands such as the upcoming NASA's Plankton, Aerosol, Cloud, and ocean Ecosystem (PACE) mission which is scheduled to launch ca. 2022. In addition, the *bPAR* model should also be extendable to other coastal waters for which high resolution bathymetry data exists and where spectral IOPs can be obtained accurately.

Overall, the validation exercise using four optically diverse test sites proved that our model was able to estimate both $bPAR_i$ and $bPAR_d$ values from MODIS AQUA remote sensing data with good skill as indicated by small bias and low MAE (within ~25%) compared to the observed "true" *bPAR* values. This suggests that our benthic irradiance model is robust to variation in optical water types found in the optically complex and shallow GBR lagoon. We do note that during extreme seasonal events, such as sediment-laden flood plumes, where acute optical stratification is present (i.e. buoyant turbid freshwater lens) the model's assumption of an optically homogenous water column is violated. Indeed, the validation results revealed that season retrievals of *bPAR* for the Yongala site, which is adjacent to the Burdekin River mouth, deviated from *in situ* observations.

We also acknowledge that the baseline *bPAR* model presented here has some limitations that if addressed, may further improve the model in the future. Firstly, our model assumed clear skies and that our validation data were generally obtained during cloud-free days, yet cloud cover variability modulates $E_d^{0^+}$ (Kirk, 2011). This assumption proved to be satisfactory for instantaneous $bPAR_i$ estimates but may have significant consequences for deriving daily integrated $bPAR_d$ values; particularly in locations where temporal variation in cloud cover may be high. We concede that cloud variability should be considered when computing $bPAR_d$, however, it is challenging to generate a cloud climatology dataset to correct our $bPAR_d$ data. Future enhancement may include statistically quantifying the effect that clouds have upon $bPAR_d$ by using *in situ* surface and sub-surface PAR datasets to empirically tune the model, both regionally and seasonally (e.g., as a cloud cover climatology). Secondly, the atmospheric model used to obtain $E_d^{0^+}$ did not include diffuse sky irradiance. Future work to improve the *bPAR* model may include using a two component "clear sky" and "cloud layer" model similar to (Frouin and McPherson, 2012). Thirdly, contributions of a wind-roughened sea surface to reflectance/transmittance across the interface may also be accounted for following Haltrin et al. (Haltrin, 2002; Haltrin et al., 2000), provided appropriate ancillary wind data that matches our model input datasets can be obtained. Lastly, the applicability of our model may also be limited in areas where tidal fluctuations are much higher than what our DSA has tried to address. The DSA represents the impact on derived bPAR if we used *in situ* (pressure) depth and 3D GBR bathymetry. We expect that the DSA is representative of most seaward regions in the GBR as well as the Cape York and Northern areas where tidal range would be similar to that observed at Yongala. In near-shore regions such as Broad Sound and Mackay we accept that the tidal ranges are about 4.6 and 6.9 m, respectively (e.g. see 3.3.5 Tides in: Steinberg et al 2007, Impacts of climate change on the physical oceanography of the Great Barrier Reef). In these locations the the DSA may not be representative.

As an estimate, the coastal area between Mackay and Broad Sound that is less than 10 m (and deeper than 5 m – which is automatically masked) represents of 0.6% of the entire GBR.

For further context, the area of GBR that automatically masked out as less than 5 m represents approximately 4% of the GBR’s total shelf area (where ‘shelf’ is water depth less than 200 m).The bottom topography and physical processes that drive the oceanography of the entire GBR are complex and therefore cannot be easily generalised. Fine tuning the water column depth in shallow locations or in regions where tides vary significantly (e.g., Broad Sound located at the southern GBR) may also improve benthic irradiance estimates for these locations.

In addition, we have not validated the results against *in situ* observations in coastal nearshore waters directly impacted by river plumes. In these waters, our assumption of vertical uniformity in water quality is likely to be weak and the error is likely to be greater than at our validation sites.

Despite the above limitations, the model results we have presented can be implemented (albeit with caution) to the entire GBR region using near-daily MODIS-Aqua data collected since 2002. This will allow for a spatiotemporally rich benthic PAR dataset to be generated for the first time at this scale. Given the importance of light availability for the health of benthic ecosystems, our model results can now be used to explore the spatial and temporal variability of benthic light in the GBR region (see Figure 13). The resulting benthic light datasets will provide information needed to assess habitat quality for corals and seagrasses. Specifically, GBR-wide maps of light thresholds (i.e., minimum light requirements for optimal system function) for these organisms can be developed from the benthic PAR values derived using this model and form the basis of a new GBR water quality index based on light, as outlined in the following chapters of this Report.

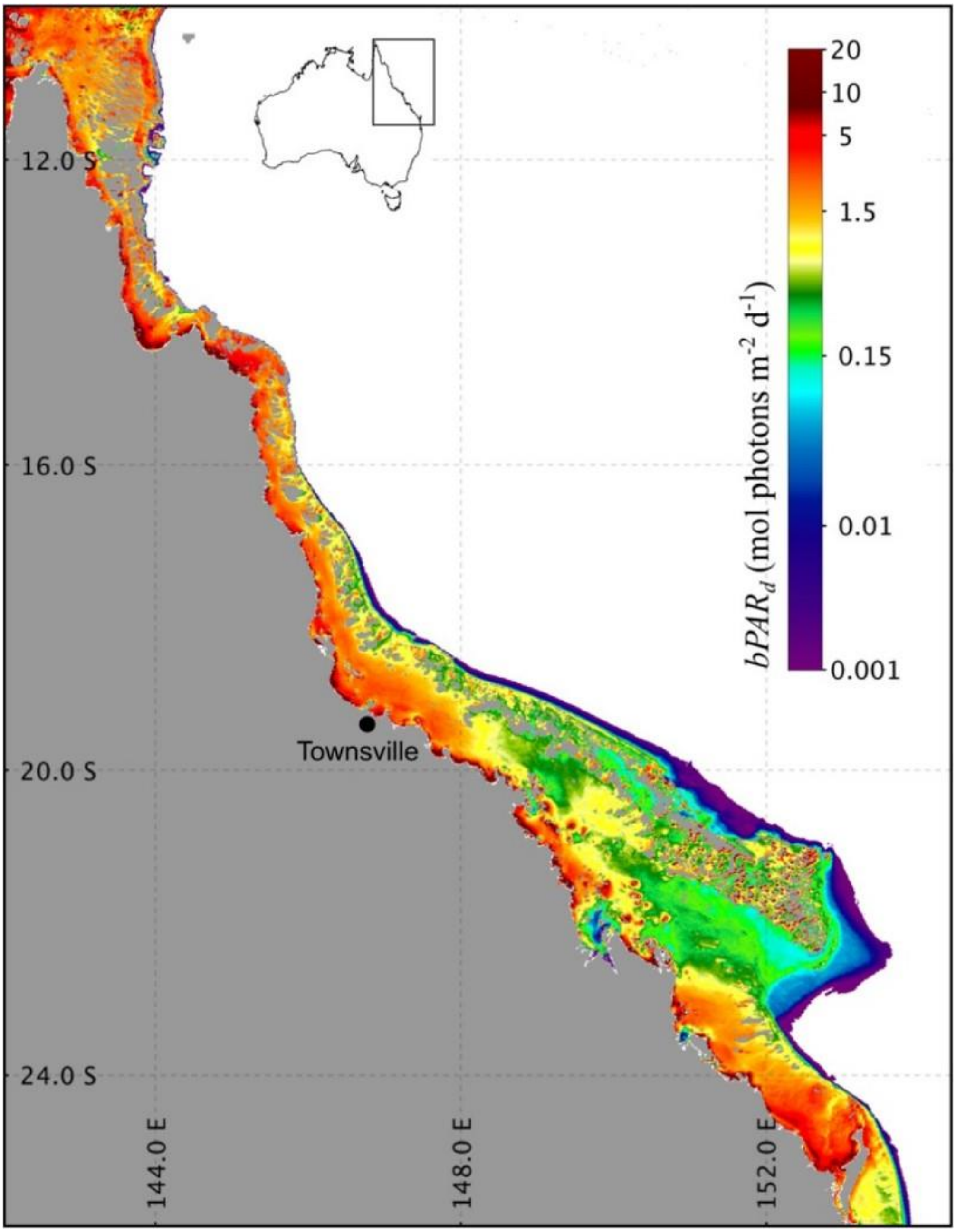

Figure 13: Map of 2016 annual mean of daily integrated benthic PAR (*$bPAR_d$*) for the Great Barrier Reef region. Colour gradient indicates values in mol photons m^{-2} d^{-1}.

Whilst we have outlined some limitations of the *bPAR* model, it is important to recognise that we do not necessarily anticipate that the satellite-derived benthic irradiance data presented here will become a standalone solution for monitoring water quality and ecosystem health in the GBR. Instead, we expect the *bPAR* model will complement existing monitoring tools such as the eReefs hydrodynamic model (Baird et al., 2016b), the Q-IMOS mooring array, and the routine *in situ* water quality sampling programs. There is great potential for the uptake of the *bPAR* model in developing additional management criteria for monitoring water quality in the GBR based on light availability, as well as exploring effects of long-term patterns of benthic light availability on corals and/or seagrasses which has not been possible before now.

3.0 OPERATIONAL DELIVERY OF BPAR DATA

Code to calculate spectral K_d and PAR at any depth, as described in Chapter 2.0, has been provided to NASA for incorporation into their Ocean Colour Science Software (OCSSW) as an experimental/test algorithm. Pre-compiled OCSSW code is traditionally released with versions of the SeaDAS software package (NASA) and the source code is also released via github. NASA have advised that it will be available to the remote sensing community in the upcoming release of SeaDAS v8. We note that NASA's OCSSW code is multi-sensor code, meaning it can be applied to data from any NASA-supported ocean colour sensor (see: https://seadas.gsfc.nasa.gov/missions/). Thus, the bPAR model can be applied to existing MODIS data and data from newer and satellites with higher spectral resolution and greater reliability such as the upcoming Plankton, Aerosol, Cloud, ocean Ecosystem (PACE) hyperspectral sensor. Legacy ocean color sensors, such as the Sea-viewing Wide Field-of-view Sensor (SeaWiFS), are also supported meaning it is possible to produce a near-daily multi-sensor climatology of bPAR for the entire GBR from mid-1997. A number of non-NASA ocean color sensors can also be processed using OCSSW code including the European Space Agency's (ESA) Medium Resolution Imaging Spectroradiometer (MERIS ; 2002 – 2012) and the Ocean and Land Colour Instrument (OLCI) aboard the EU Copernicus Programme's Sentinel 3A/B satellites (S3A 2016 – present; S3B 2018 – present).

Using multiple ocean colour datasets, it is feasible that a multi-sensor merged bPAR data product could be developed, however, OLCI-derived bPAR would need to be validated as we have done so for MODIS Aqua. We also note that recent advancements in gap filling have emerged in the ocean colour research community that are very promising. For example, NOAA have recently demonstrated Data Interpolating Empirical Orthogonal Functions (DINEOF) as a way to merge and gap fill VIIRS-JPSS and VIIRS-NPP chlorophyll-a dataset (Liu and Wang, 2019). Thus, there is potential for the work presented here to be extended to produce a multi-sensor, gap filled bPAR climatology.

We have had preliminary discussions with CSIRO, who have agreed in principle to incorporate the algorithm into the Australian Geoscience DataCube to make K_d and bPAR data products for the GBR operationally available. This in-principle understanding is subject to logistical reality – there is no commitment if operational difficulties were to be encountered.

An alternative, already routinely available bPAR data source for the GBR is the eReefs biogeochemical model. eReefs biogeochemical model outputs include simulated ocean colour and Epibenthic PAR above the seagrass layer (essentially, bPAR). eReefs data is available from National Computing Infrastructure THREDDS servers at http://dapds00.nci.org.au/thredds/catalogs/fx3/catalog.html, from CSIRO servers via https://research.csiro.au/ereefs/ and in a simplified, regularised netCDF format from AIMS servers at http://thredds.ereefs.aims.gov.au/thredds/s3catalogue/aims-ereefs-public-prod/derived/ncaggregate/ereefs/catalog.html. At the time of writing this Report (November 2020), the most recent version of the near real-time eReefs biogeochemical model data (B3p1) has not yet been publicly exposed via the NCI server, but the CSIRO modelling team has assured us that it is their intention to do so in the near future (Baird, *pers. comm.*).

The algorithms used to calculate the eReefs optical data products have been described in detail in the peer-reviewed literature (Baird et al., 2020a; Baird et al., 2020b; Baird et al., 2016b).

In Chapter 7.0, we will discuss the performance of the eReefs PAR data product, and demonstrate that although it does not provide a 1:1 match with the remote sensing data product, it is suitable as a data source for the purpose of monitoring year-to-year variations in water quality in the GBR via the bPAR index.

4.0 DEVELOPMENT OF THE BPAR INDEX

The work presented in Chapter 4.0 and Chapter 5.0 has been submitted to a peer-reviewed international journal and will form part of the PhD thesis of Marites Canto. It can be cited as:

> Canto, M. M., Fabricius, K. E., Logan, M., Lewis, S., McKinna, L. I. W., & Robson, B. J. (submitted). A benthic light index of water quality in the Great Barrier Reef, Australia.

Figure 14: Photosynthesis drives productivity in healthy reef habitats, and is essential for reef associated fishes and invertebrates. Credit: Miles Grandy.

4.1 Introduction

4.1.1 Great Barrier Reef and water quality

Coastal oceans around the world are vulnerable to the impacts of multiple stressors ranging from increased coastal developments and anthropogenic activities to extreme weather events and climate change. Unfortunately, the Great Barrier Reef (GBR) is not impervious to these stressors (Wolff et al., 2018). The GBR is one of the most diverse marine habitats on Earth and forms a critical part of the Australian economy (Deloitte Access Economics, 2013) and national natural and cultural heritage (Lucas et al., 1997). Recurrent and recent mass coral bleaching due to thermal stress (Hughes et al., 2017; Hughes et al., 2018b), pollution from agricultural runoffs (Kroon, 2012) and the associated declining quality of the water entering the GBR lagoon (Fabricius et al., 2016b), and crown-of-thorns seastar (COTS) outbreaks (Fabricius et al., 2010) present current challenges in maintaining the health of the GBR.

Considering these numerous environmental pressures, it is important for management agencies to have tools that can be used to identify and monitor changes that can impact the ecosystem's health. Understanding the factors driving these changes and how the ecosystems respond to both short- and long-term environmental forces (Ackleson, 2003) can help focus management actions, integrate relevant management approaches and increase the anticipated success in addressing identified challenges.

One of the main priorities for maintaining the health and resilience of the GBR ecosystems is the management of water quality flowing into the Reef since poor water quality can reduce light availability at depth. Poor water quality is considered a key factor for declining marine ecosystem health (Fabricius et al., 2016b) and regarded as a major threat to the health of the GBR (De'ath and Fabricius, 2010; Devlin et al., 2015a). The need to address the threats associated with declining quality of the water (Fabricius et al., 2016b) has been recognised by both the Australian and Queensland Governments and this is reflected in the Reef 2050 Long-term Sustainability Plan (Reef 2050 Plan) (Commonwealth of Australia, 2015) which aims to preserve the heritage value of the Reef between now and 2050 and provide support to the development and implementation of water quality improvement plans strategic to relevant catchment and coastal systems along the length of the GBR, including development of tools to inform and monitor GBR water quality.

4.1.2 The ecological importance of benthic light

Light is essential for photosynthesis, the foundation of all food webs and the dominant source of energy for corals and seagrasses (Kirk, 2011). For these benthic organisms, the most important part of the light spectrum is the photosynthetically active radiation (PAR) – the amount of available solar irradiance (light) typically within the 400 to 700 nm wavelength range – and specifically, the amount of PAR reaching the sea floor or reef surfaces, known as 'benthic PAR' (bPAR, mol photons m^{-2} d^{-1}) (Magno-Canto et al., 2019; Magno-Canto et al., 2020b). The spatial and temporal variability of bPAR in shallow coastal environments is a crucial control of benthic primary production and its contribution to the total primary production (Gattuso et al., 2006). It is therefore key to understanding and monitoring the dynamics and health of important benthic habitats near the coasts.

Although some species of seagrass and corals can tolerate a wide range of benthic irradiance, both low and high benthic light can create stress (Bessell-Browne et al., 2017; Gattuso et al., 2006; Muir et al., 2015). Some species can tolerate short periods of reduced light intensities in shallow waters, but their photosynthesis and growth may be reduced during these periods. Some seagrass taxa are able to persist to appreciable water depths owing to effective morphological and physiological adaptations to low-light conditions (Dennison, 1987; Ralph et al., 2007). However, reduced light availability, whether chronic or acute, is a threat to seagrass meadow health (Collier and Waycott, 2009; McKenzie et al., 2012), a major driver of seagrass loss in coastal and inshore GBR (Collier et al., 2012b; Collier et al., 2012c), and can strongly alter coral communities (Bessell-Browne et al., 2017; Muir et al., 2015).

Interactions between benthic irradiance and other stressors are also important for both corals and seagrasses. For example, turbidity-induced light reductions can result in reduced coral recruitment and diversity (Fabricius, 2005). Similarly, prolonged exposure to 'dark' (low to no light) conditions during high turbidity (e.g., near dredging locations) can cause sub-lethal bleaching in some corals (Bessell-Browne et al., 2017a; Bessell-Browne et al., 2017b) while others were able to adjust to combination of low light (2.3 mol photons m^{-2} d^{-1}) and elevated suspended sediment concentrations (Jones et al., 2020). Other examples include increased coral bleaching during high irradiance in the presence of thermal stress (Leahy et al., 2013) and compromised seagrass survival during limited light levels and high nutrient conditions (McKenzie et al., 2010). Further, for some seagrass species (i.e., *Halophila ovalis*), additional shading in an already-turbid low light environment can result in complete mortality, demonstrating that historical light exposure is important in maintaining the resilience and ability of seagrasses to acclimate to chronic low light regimes (Yaakub et al., 2014). Yet, there is also recent evidence that during heat-induced bleaching events some turbidity can benefit nearshore reef corals by alleviating the harmful effects of the combination of thermal stress and high irradiance (Cacciapaglia and van Woesik, 2016; Fisher et al., 2019; Morgan et al., 2017; Sully and van Woesik, 2020). These results highlight the complex role of light availability to the survival, growth and maintenance of dependent benthic organisms and hence, the need to develop a water quality metric that is not only ecologically relevant but also responsive to changes in light availability.

4.1.3 Physical controls of benthic PAR

bPAR is controlled by both water quality and water column depth (Magno-Canto et al., 2019). In shallow coastal waters, bPAR is mainly determined by the attenuation of light as it travels through the water column by optically active constituents including phytoplankton, suspended non-algal particulate matter, and coloured dissolved organic matter (CDOM) which attenuate (either by absorption and/or scattering) and change the character of light with depth (Brando et al., 2012; Kirk, 2011).

Water clarity in the GBR, a parameter related to water quality and commonly expressed as Secchi depth (Z_{sd}) or photic depth, is affected by river discharge. River flood plumes often transport high loads of fine sediments, nutrients – that can induce phytoplankton blooms – and dissolved organic matter that directly impact coastal water clarity. Previous studies indicate that tracking interannual variability is important to understand temporal variability and to develop predictive casual relationships (Fabricius et al., 2013; Fabricius et al., 2014; Fabricius et al., 2016b). Metrics to calculate the exposure of GBR reef and seagrass habitats to flood plumes have been developed (Devlin et al., 2012; Devlin et al., 2015a; Petus et al., 2014) using the ‘colour’ of water in the vicinity of the plume from enhanced True Colour satellite-imagery. These metrics have provided an integration of multiple potential impacts of flood plumes, from reduced water clarity to freshwater exposure to the potential impacts of pesticide exposure and sedimentation. As such, these exposure metrics have offered a useful estimate of risk associated with water quality that can inform targeted management of relevant catchments (Alvarez-Romero et al., 2013; Petus et al., 2018).

However, light penetration and photic depth indeed vary across the whole GBR in response to inter-annual variations in river discharge (Fabricius et al., 2014; Fabricius et al., 2016b; Logan et al., 2013) which occur not only in the coastal areas adjacent to river mouths, but also in the mid- and outer-shelf areas of some regions. These effects were also not only shown to be spatially extensive but can be observed more than six months after flood plumes have dispersed, suggesting that flood plume detection is not in itself sufficient to characterise the likely spatial and temporal extent of the ecological impacts of river runoff and human activities in Queensland catchments and coastal regions.

4.1.4 The need for an improved water quality index (WQI)

A motivation for developing a benthic light-based index of water quality is the need to relate changes in bPAR to ecological outcomes such that interannual progress and variations in water quality can be tracked within the whole GBR region (i.e., within each Natural Resource Management (NRM) region and water body across the GBR shelf, see Figure 15). A WQI is a quantitative metric that provides a standardised measure of water quality indicators (examples discussed below) as compared against a threshold value (Robillot et al., 2018), defined at a level intended to help identify the need for management actions (Great Barrier Marine Park Authority, 2010b). In the GBR, the WQI is used to generate scores for water quality which forms part of the annual GBR "Report Card" (Robillot et al., 2018) (https://www.reefplan.qld.gov.au/tracking-progress/reef-report-card) used to monitor the condition and trend of GBR ecosystem health and drivers to guide management based on a consistent science-based national strategy for managing water quality (e.g., Reef 2050 Water Quality Improvement Plan 2017-2022 (State of Queensland, 2018) as part of the Reef 2050 Long-term Sustainability Plan (Reef 2050 Plan) (Commonwealth of Australia, 2015)).

Two water quality sub-indicators are currently used to provide information about GBR inshore marine conditions and generate a WQI reported as part of the annual GBR Report Cards: chlorophyll-*a* pigment concentration, Chl *a* (mg/L) as a productivity sub-indicator, and Secchi depth, Z_{sd} (m) as a water clarity sub-indicator (Robillot et al., 2018). Chl *a* associated with phytoplankton biomass is a widely-used proxy for nutrient pollution in the GBR, in that annual mean concentrations above a threshold (which varies from 2.0 to 0.4 mg/L from inshore to offshore locations) are considered an indication of water quality degradation associated with eutrophication (increased nutrient inputs, e.g., from floods or river runoffs, and a subsequent increase in phytoplankton biomass) (Schaeffer et al., 2013) and light attenuation (Platt et al., 1994). The photic depth, Z_{sd}, which quantifies the depth of in-water visibility (Kirk, 2011), is a common proxy for water clarity (transparency) and is inversely related to turbidity (i.e., cloudiness/opacity of the water). Declining Z_{sd} indicates increased turbidity and reduced light. Although indicative of changes in water quality, Z_{sd} does not directly tell us what light environments are experienced by seagrasses and corals, as the relationship varies with depth in the water column and with the colour (i.e., optical properties) of the water. Hence, while the spatial and temporal variations in Z_{sd} can be characterised using existing remote sensing data products developed for the GBR (Weeks et al., 2012), translating these variations to ecological outcomes such as the exposure to stress from low-light is not straightforward.

Using satellite-derived bPAR to provide an index of water quality instead of the WQI from combined Z_{sd} and Chl *a* indices will allow the interacting effects of complex optically active constituents that define water clarity and the spatially variable bathymetry (water depth) to be considered. This will allow, for the first time, the application of ecologically-relevant, GBR-specific light thresholds for corals, seagrasses and overall ecosystem health.

The objective of this work is therefore to use the new satellite-derived estimates of daily benthic irradiance or bPAR to develop an ecologically-relevant marine index of water quality to replace or complement the current combined Z_{sd}– and Chl*a*–based index. The proposed benthic light index will incorporate the benthic light regimes within the GBR at spatial scales that is required by the GBR Marine Park Authority (GBRMPA) in the preparation and issue of the annual GBR Water Quality Report Cards.

4.2 Methods

4.2.1 Study site

The GBR Marine Park lies adjacent to the Queensland coast along the north-eastern seaboard of the Australian continent. It stretches about 2300 km in length, occupying the continental shelf roughly between 9°S and 24°S. Along its length, there are 35 main river basins with catchment areas that drain into the GBR lagoon (Furnas, 2003), and each catchment varies in its land use (Fabricius et al., 2016b) and impact on the quality of the water within the lagoon. To facilitate regional comparisons consistent with recent efforts to manage and monitor the health of waters within the GBR lagoon and account for spatial differences across the shelf, we used a combination of the NRM regional GBR catchment and cross-shelf water body boundaries which respectively include (from North to South): the Cape York, Wet Tropics, Dry Tropics (Burdekin), Mackay-Whitsunday, Fitzroy, and Burnett Mary regions, and the (i) enclosed coastal, (ii) open coastal, (iii) midshelf and (iv) offshore water bodies (Great Barrier Marine Park Authority, 2010a) (see Figure 15). For clarity, combinations of the NRM regions and the water bodies are interchangeably referred to as “zones” throughout this Chapter.

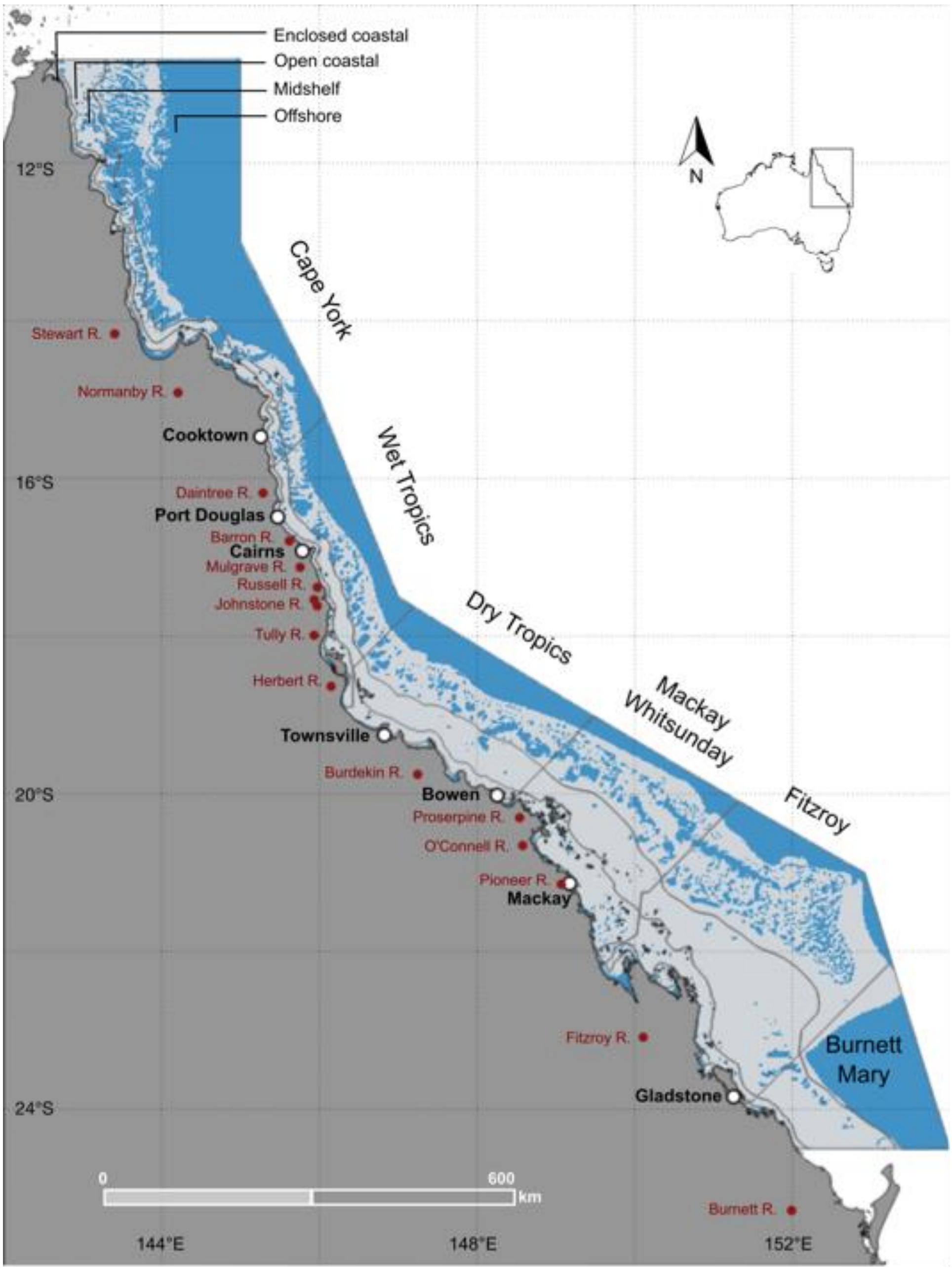

Figure 15: Map of the Great Barrier Reef showing the reef matrix, boundaries of the six NRM regions (N to S: Cape York, Wet Tropics, Dry Tropics, Mackay Whitsunday, Fitzroy, and Burnett Mary) and the four cross-shelf water bodies used in the analysis (Enclosed coastal, Open coastal, Midshelf and Offshore). Also indicated are several major cities (filled white circles) and rivers (filled red circles) along the length of the GBR.

4.2.2 Defining spatial and temporal aggregation aligned with the current GBR Report Cards

Annual GBR Report Cards are currently used to monitor and communicate the condition and trend of GBR ecosystem health and drivers to guide management of the Reef. The GBR reporting framework uses consistent, well-defined spatial boundaries for aggregation, which are based on a combination of the NRM regions and cross-shelf water body boundaries (as shown in Figure 15) and temporal boundaries that uses a “water year” – defined as the period between 01 October to 30 September of the following calendar year. This temporal aggregation ensures that austral wet seasons are not split across reporting years (Waterhouse et al., 2017) and is hence adapted in the present study to align with the current management, monitoring and reporting framework of water quality status in the GBR.

4.2.3 The bPAR index

The development of a bPAR index requires three components: (i) a benthic light threshold relevant to targeted benthic organisms (i.e. corals and seagrasses); (ii) robust, spatiotemporally consistent estimates of bPAR data; and (ii) a method of combining these to map benthic light stress within the entire GBR and generate an index that can inform managers and policy makers of when and where benthic light conditions are less optimal for corals and seagrasses as a result of intermittent factors that control water clarity. The following sections provide more detail for each of these components.

4.2.4 Benthic light responses and thresholds for key GBR coral and seagrass species

Information about light responses and relevant thresholds for some key GBR coral and seagrass species was compiled from both field and laboratory/experimental data obtained from complementary laboratory studies and a review of pertinent literature. Our purpose is to determine a collective maximum benthic light threshold that both corals and seagrasses could potentially make use of for photosynthesis and growth under varying water quality conditions. The relationship between light intensity and photosynthesis is modelled as a photosynthesis-irradiance (P-E) curve (Sakshaug, 1997) which provides a measure of the efficiency of utilization of the incident light (Kirk, 2011). In a P-E curve, photosynthetic rates initially increase linearly with irradiance until the maximum photosynthetic potential, P_{max}, is reached. Further increases in irradiance then result to photosynthetic rates plateauing, until the point of light-induced reduction in photosynthetic capacity of the plant (i.e., photoinhibition) (Sakshaug, 1997). P-E curves thus provide the information needed to define a relevant threshold for our benthic light index.

Most of the previous studies that examined benthic light requirements have focused on determining the lowest light limits at which species are being found (e.g., (Gattuso et al., 2006; Muir et al., 2015). In contrast, we focused our index on the light needed to obtain P_{max}, as below this level, the organisms' growth rates are compromised, and above this P_{max}, there are no further growth benefits of increased light.

Light requirements and responses of corals and seagrasses to light vary considerably between species and conditions (Table 4). For example, Muir et al. (2015) has suggested that for Acropora corals, the most important reef-building coral species found in the GBR, a winter PAR threshold of 5.2 mol photons m^{-2} d^{-1} strongly determines their depth limits, a value relatively lower than the 7 to 8 mol photons m^{-2} d^{-1} light limit for reef formation reported by Kleypas (1997). Considering the surface area corresponding to global coastal oceans where important benthic organisms flourish, Gattuso et al. (2006) also calculated a mean benthic irradiance of 1.2 mol photons m^{-2} d^{-1} at the maximum depth of coral colonisation as well as a mean compensation irradiance for benthic communities at a range of 0.24 to 4.4 mol photons m^{-2} d^{-1}. Gattuso et al. (2006)'s mean benthic irradiance value is comparable to benthic light threshold for reef development of ~2 mol photons m^{-2} d^{-1} estimated for Whitsunday Islands in the GBR – a region with strong water quality gradient (Cooper et al., 2007) and in the Gulf of

Siam (Titlyanov and Latypov, 1991). A benthic PAR threshold for other important benthic habitats (e.g., macroalgae) has also been reported where levels below 2 mol photons m^{-2} d^{-1} were found to cause steep declines in macroalgal species richness (Hurrey et al., 2013) while other assemblages such *Lobophora*-turf and *Halimeda*/Bryopsidales have strong affinity to light thresholds of 3.6 mol photons m^{-2} d^{-1} and 4.6 mol photons m^{-2} d^{-1}, respectively.

For seagrasses, average daily irradiance (i.e., PAR) above 5.0 to 8.4 mol photons m^{-2} d^{-1} has been associated with increased seagrass abundance (i.e., cover) but prolonged exposure to conditions below 3.0 mol photons m^{-2} d^{-1} resulted in 50% seagrass cover loss (Collier et al., 2012b). More than 4 weeks of light below 5.0 mol photons m^{-2} d^{-1} also resulted in a decline in seagrass condition (i.e., biomass, shoot density and percent cover) (Chartrand et al., 2016). Hence, for seagrasses, it has been suggested that risk of light limitation may occur when average daily benthic PAR falls below 5 to 6 mol photons m^{-2} d^{-1} (Chartrand et al., 2016; Collier et al., 2012b) although some deep-water species (e.g., *Halophila spp*.) can tolerate daily average light from 2 to 6 mol photons m^{-2} d^{-1}. The latter range is thus suggested as the lowest light threshold for managing acute impacts of light limitation on seagrasses, while 10 to 13 mol photons m^{-2} d^{-1} is the currently suggested limit for managing long term chronic impacts of light limitation on seagrasses (Collier et al., 2016a).

Recent experimental studies that investigated the different responses of key GBR coral species to different water quality gradients (Strahl et al., 2019), different daily light integral (DLI) levels at either constant or variable doses (DiPerna et al., 2018), and effects of variable light on adult and juvenile corals under increasing carbon dioxide levels (Noonan et al., (in prep)) have also provided useful insights on coral light requirements relevant to the present study. For example, Strahl et al. (2019) highlighted that in a region with a strong water quality gradient (e.g., near the Burdekin River), *Acropora tenuis* showed reduced calcification at light levels below ~10 mol photons m^{-2} d^{-1} but exhibited high growth rates (i.e., total Chl *a* content, net photosynthesis and light and net calcification) at moderate light levels between ~14 to 16 mol photons m^{-2} d^{-1} (Table 4). A reduction of light by ~ 50% (e.g., from moderate to low light levels), for instance in shallow turbid inshore waters like the Burdekin River region, markedly reduced rates of net photosynthesis and light calcification although the observed variations in water quality did not have detrimental effects on *A. tenuis* (e.g., as long as light levels received are not limiting such as when there is no light).

DiPerna et al. (2018), on the other hand, showed that coral responses to constant (high or low DLI) or variable light conditions (with alternating segments of high and low DLI levels) during a 20-day laboratory experiment did not vary greatly between two morphologically different GBR reef corals, *Pachyseris speciosa* and *Acropora millepora*. Specifically, the 'shade-tolerant' *P. speciosa* showed chronic light-limitation response at low DLI of 6 mol photons m^{-2} d^{-1} and light inhibition response at high DLI of 32 mol photons m^{-2} d^{-1}, under both constant and variable light conditions (DiPerna et al., 2018). For a 'high-light tolerant' *A. millepora* exposed to the same light conditions, observed responses suggested chronic light-limitation under all conditions by the end of the experiment although growth observations noted (i.e., differences in nubbins' buoyant weight over time) in *A. millepora* also indicated that it was able to gain some advantage when exposed to constant high daily light. Relationships between incident irradiance and oxygen production (one of the parameters used to indicate photosynthetic efficiency) for *P. speciosa* and *A. millepora* at all light treatments (high, low and variable light levels) presented in the DiPerna et al. (2018) paper did not greatly differ between the coral species studied, suggesting that these corals have equivalent photosynthetic efficiency regardless of the level of instantaneous irradiance treatment received. In other words, the minimum or the maximum instantaneous light is probably less important than the total daily integrated light received as a predictor of the health and growth of these corals. This is further supported by the results obtained by Noonan et al. ((in prep)) in their laboratory experiments that investigated the effects of variable light levels and pCO_2 (partial pressure of carbon dioxide, used in ocean acidification studies) on *Acropora sp.* reef corals. This work (Noonan et al., (in prep)) concluded that the rate of increase in photosynthesis (as measured by the changes in the relative electron transport rate) on mature *Acropora sp.* is directly related to the total amount of light the corals received within the range of light conditions it was subjected to, highlighting the importance of cumulative amount of light received as opposed to instantaneous irradiance levels.

The above review has highlighted that light thresholds relevant to corals and seagrasses (and potentially other benthic organisms) vary widely (from ~ 2 mol photons m^{-2} d^{-1} to 16 mol photons m^{-2} d^{-1}) and that at irradiance values higher than these, there is very little additional benefit in terms of growth. In developing the benthic light limitation index, our intent is to use a parameter for benthic light stress that reflects reduced opportunity for photosynthesis due to low light, but does not consider stress (e.g., photoinhibition) due to excessively high bPAR that may be relevant during bleaching events (Leahy et al., 2013; Mumby et al., 2001) since our purpose is to produce an index of chronic light stress due to reduced water quality, which is not the cause of photo-oxidative stress during bleaching events.

Table 4: Benthic light thresholds and responses for some key GBR coral and seagrass species and other benthic organisms.

Taxonomic group	Species	Conditions / Notes	Threshold / Response	Reference
coral	*Acropora, Isopora*	global *in-situ* coral identification and depth data	winter PAR threshold of 5.2 mol photons m^{-2} d^{-1} define colonisation depth of Acropora	(Muir et al., 2015)
coral		global limit for reef formation (net $CaCO_3$ production)	7 to 8 mol photons m^{-2} d^{-1}	(Kleypas, 1997)
coral		*in-situ* total daily PAR, Whitsunday Islands, depth limit for reef development	absolute minimum light threshold ~ 2 mol photons m^{-2} d^{-1}	(Cooper et al., 2007)
coral	*Scleractinia*	*in-situ* surface irradiance (obtained as 50% of total solar radiation above water surface), depth limit for reef development, Gulf of Siam	~ 2 mol photons m^{-2} d^{-1}	(Titlyanov and Latypov, 1991)
coral		average benthic irradiance at the maximum depth of coral colonization	1.2±1.7 mol photons m^{-2} d^{-1}	(Gattuso et al., 2006)
macroalgae	*macroalgae (general)* *Lobophora*-turfs *Halimeda*/Bryopsidales		steep decline in richness at 2 mol photons m^{-2} d^{-1} 3.6 mol photons m^{-2} d^{-1} 4.6 mol photons m^{-2} d^{-1}	(Hurrey et al., 2013; Pitcher et al., 2007)
benthic community		daily compensation irradiance of benthic communities	ranges from 0.24 to 4.4 mol photons m^{-2} d^{-1}	(Gattuso et al., 2006)
seagrass (meadow)	Predominantly *Halodule uninervis*, some *Cymodocea serrulata* and *Halophila ovalis*	*in-situ* monitoring in Northern GBR (sites: Magnetic Island,	increased seagrass abundance (i.e., cover) at mean daily irradiance above 5	(Collier et al., 2012b)

		Dunk Island and Green Island), seagrass cover measure ~3-month intervals (2008 – 2011), nearshore reef habitats exposed to influence from terrigenous run-offs	and 8.4 mol photons m^{-2} d^{-1}, 16 to 18% of days below 3 mol photons m^{-2} d^{-1} associated with 50% seagrass cover loss	
seagrass	*Zostera muelleri sp. capricorni*	in-situ, intertidal mudbank, sheltered embayment, Gladstone Harbour, simulated dredging impacts	declined seagrass conditions (biomass, shoot density and percent cover) at £ 5 mol photons m^{-2} d^{-1} for periods > 4 weeks, 6 mol photons m^{-2} d^{-1} (suggested management light threshold) mitigated dredging impacts	(Chartrand et al., 2016)
seagrass	*Cymodocea serrulata, Halodule uninervis, Halophila ovalis* and *Zostera muelleri*	aquaria-based experiments, six light treatments: 0, 5, 10, 20, 40 and 70% of surface irradiance (= 32.8 mol photons m^{-2} d^{-1}) equivalent to light levels ranging from 0 to 23 mol m^{-2} d^{-1}, warm (~23°C) and cool (~28°C) temperatures over 14 weeks	declined seagrass shoot density and leaf growth rates at lowest light levels but were maintained at highest light levels, quicker decline of shoot density and leaf growth rates at low light treatments in warm than cool temperatures	(Collier et al., 2016b)
seagrass	*Halophila sp., Zostera muelleri, Halodule uninervis, Cymodocea sp., Syringodium isoetifolium, Thalassodendron ciliatum, Thalassia hemprichii, Enhalus acoroides*	synthesis of light thresholds and guidelines for seagrass of the GBR	biological light thresholds of 2–6 mol photons m^{-2} d^{-1} for managing acute impacts; 10–13 mol photons m^{-2} d^{-1} for managing long term impacts of light limitation (except for some deep water species which require less light)	(Collier et al., 2016a)
seagrass		global synthesis of published light requirements across multiple species	minimum light requirement: range of 0.06 to 14.1 mol photons m^{-2} d^{-1}; overall median of the minimum light requirement: 5.1 mol photons m^{-2} d^{-1}	(Gattuso et al., 2006)

seagrass	*Cymodocea serrulata, Halodule uninervis, Halophila ovalis* and *Zostera muelleri*	aquaria-based experiments	suggested conservative management guideline thresholds of 7 and 13 mol photons m^{-2} d^{-1} to provide 50% and 80% protection of seagrass shoots over a 14-week period, respectively.	(Collier et al., 2016b)
coral	*Pachyseris speciosa*	laboratory experiment, variable light treatments (alternating high and low light treatments)	physiological stress in both high and low light segments, rapid declines in maximum quantum yield (i.e. photoinhibition) at 32 mol photons m^{-2} d^{-1}, recovery (photoacclimation) within 3-5 days at 6 mol photons m^{-2} d^{-1}	(DiPerna et al., 2018)
coral	*Pachyseris speciosa*	laboratory experiment, constant light treatments	low values of Q_m (or excitation pressures on PSII (an estimate of light limitation against photoinhibition); chronic light-limitation at constant low light (6 mol photons m^{-2} d^{-1}); photoinhibition at constant high light (at 32 mol photons m^{-2} d^{-1})	(DiPerna et al., 2018)
coral	*Acropora millepora*	laboratory experiment, variable light treatments (alternating high and low light treatments)	intermediate growth in variable daily light conditions, slow (>20 days) photoacclimation	(DiPerna et al., 2018)
coral	*Acropora millepora*	laboratory experiment, constant light treatments	reduced growth (i.e., buoyant weight) due to photolimitation at constant low daily light (6 mol photons m^{-2} d^{-1}) compared with constant high daily light (32 mol photons m^{-2} d^{-1})	(DiPerna et al., 2018)
coral	*Acropora tenuis*	Laboratory-simulated inshore reef field conditions, three daily light integral (DLI) treatments (no light: 0 mol photons m^{-2} d^{-1}, low: 7.92 – 9.36 mol photons m^{-2} d^{-1}, and moderate: 13.86 – 16.38 mol photons m^{-2} d^{-1}), strong water quality gradient (Burdekin region),	decreased net photosynthesis rates, light calcification rates, and net calcification rates from low DLI (8-9.4 mol photons m^{-2} d^{-1}) to moderate light (14-16 mol photons m^{-2} d^{-1})	(Strahl et al., 2019)

		moderate water quality conditions (Magnetic Island), ~60 km from Burdekin River mouth		
coral	*Acropora tenuis* or *A. hyacinthus*	laboratory experiment, four light treatments including variable light levels (low: 2.5, medium: 7.6, and high: 12.6 mol photons m^{-2} d^{-1})	increasing growth rates from low (2.5 mol photons m^{-2} d^{-1}) to high (12.6 mol photons m^{-2} d^{-1}) light levels (growth rate linearly increased/decreased with cumulative daily light integrals received), cumulative amount of light received affects physiological response	(Noonan et al., (in prep))

4.2.5 Benthic PAR data

The second requirement for developing an index is a consistent and spatio-temporally rich estimate of benthic PAR. We obtained daily bPAR estimates for the GBR study region (Figure 15) from a benthic irradiance model (Magno-Canto et al., 2019; Magno-Canto et al., 2020b) that uses ocean colour satellite observations from the National Aeronautics and Space Administration (NASA)'s Moderate Resolution Imaging Spectroradiometer (MODIS) aboard the Aqua satellite (NASA Goddard Space Flight Center). The benthic irradiance model estimates the amount of light reaching the seafloor by considering spectrally-varying vertical diffuse light attenuation and variations in depth for each nominal 1 km^2 pixel (Magno-Canto et al., 2019; Magno-Canto et al., 2020b). Here, we used the daily integrated bPAR data product extracted over a domain within 10.7 – 24.5°S and 142 – 154°E along north-eastern Australia (Figure 15) between July 2002 and December 2019. Following the methods for generating the required daily bPAR data product described in Magno-Canto et al. (2019), we obtained 6322 individual files representing 17.5 years of data. Data aggregation and water quality index calculation were then conducted in R v3.4.1 (R Core Team, 2019b).

4.2.6 Developing the benthic light-based water quality index

4.2.6.1 Calculating total relative benthic light stress for each unmasked pixel

We first defined benthic light stress, S, as the cumulative stress due to benthic light levels falling below the defined bPAR threshold, T. The value of this threshold, 16 mol photons m^{-2} d^{-1}, forms part of the results of this study and is explained in section 4.3.1. For any location in each data file where the per pixel MODIS-derived daily benthic PAR value, $bPAR_d$, exceeded T, we capped at $bPAR_d = T$ on that pixel. Locations with missing data points in a $bPAR_d$ file were gap-filled using a monthly mean value calculated on that pixel (i.e., $bPAR_d$ values on days with data were averaged for each corresponding month).

For each pixel, we then calculated a reference value, $bPAR_R$, which was defined as the 95th-percentile $bPAR_d$ for each calendar month observed over the decade 2003-2013. This reference value was taken to represent the $bPAR_d$ that could potentially be achieved in the best possible water quality conditions at that location and time of year. In very deep water, 'sufficient' (high) $bPAR_d$ is not achievable regardless of water quality due to attenuation of downwelling irradiance over the pathlength by seawater and constituent matter. In the context that 'high' $bPAR_d$ is subjective depending on the body of water considered (e.g., GBR vs. Chesapeake Bay), we regard 'sufficient' $bPAR_d$ as values high enough relative to our chosen threshold. In shallow water, high $bPAR_d$ should be achievable, as light availability is a function of water column depth and optical properties, however some nearshore areas may be naturally turbid and therefore highly attenuating regardless of human impacts on water quality.

To calculate the relative daily stress due to low light, S_d, (mol photons m^{-2} d^{-1}) for each day and pixel location, we used:

$$S_d = bPAR_d - bPAR_R. \tag{16}$$

Equation (1) denotes that when S_d is close to zero, there is either sufficient $bPAR_d$ (hence, no stress) on that pixel on that day, i. e., no more light stress than observed in the best 5% of observed conditions for that pixel. S_d values <0 were set to zero.

The integral of S_d over a time-period of interest (seasonal or annual) thus indicates the chronic light stress due to poor water quality experienced at a given location.

4.2.6.2 *Summarising relative benthic light stress over management zones*

Finally, to obtain *S* (the cumulative stress due to benthic light levels falling below our defined bPAR threshold, with a unit of mol photons m^{-2} per year or season), we summed S_d spatially over each zone (i.e., combination of six NRM management regions and four shelf water bodies) and temporally for each 'water year' using:

$$S = \sum_{d=1}^{n} S_d \tag{17}$$

where *n* is the number of days in the time-period of interest (i.e., *n* = 365 for annual integral, or *n* = 183 for the number of days in the austral wet season (01 November to 30 April) and austral dry season (01 May to 31 October) for each 'water year', respectively).

4.2.6.3 *Calculating the bPAR index over management zones*

The bPAR index, *I*, for each zone was then obtained as:

$$I = \sum_{p=1}^{z} \left(S - S_{\max}\right)_p \tag{18}$$

where *z* is zone and $S_{max} = T{*}n$ where *T* is again the bPAR light threshold and *n* is the number of days in the integration period (i.e., S_{max} is the maximum theoretically possible value of *S* for that pixel). Note that for the Burnett-Mary NRM region, the offshore water body was deep throughout: there were few if any pixels that ever receive sufficient bPAR to support seagrass or coral habitats, hence unable to be reported.

4.2.6.4 *Scaling and assigning letter grades*

The final benthic light index, I_{PAR}, was then obtained by linearly rescaling *I* to a value between 0 and 1 to allow unbiased (e.g., equally weighted) comparison of relative benthic light stress values in different zones. The scaled I_{PAR} values range from 1.0, indicating *low benthic light stress* (very good water quality) to 0.0, indicating *the maximum observed benthic light stress in any season in the record for that zone* (very poor water quality). Finally, scaled I_{PAR} values were mapped onto the five-point (A-E) colour-coded grading scale (Table 5) used in the current GBR Water Quality report cards (Robillot et al., 2018).

Table 5: Colour-coded scoring system adapted to indicate the levels of light stress.

Grade	Light stress	Description	Numerical	Colour
A	No stress	Very good	> 0.8 – 1.0	Dark
B	Low stress	Good	> 0.6 – 0.8	Light
C	Moderate stress	Moderate	> 0.4 – 0.6	Yellow
D	High stress	Poor	> 0.2 – 0.4	Orange
E	Very high stress	Very poor	0 – 0.2	Red

4.2.6.5 *Relating the bPAR index to estimates of catchment-derived loads of total suspended sediments, dissolved inorganic nitrogen and river discharge*

For the purpose of relating potential variability in the bPAR index to a specific water quality driver (i.e., turbidity due to increased suspended sediment concentrations, CDOM from freshwater discharge or increased availability of nutrients that can support biological processes that may also reduce light availability), we also considered estimates of total suspended sediment (TSS) loads, dissolved inorganic nutrient (DIN) loads, and river discharge data from major catchment regions that contribute most to the runoff inputs to the GBR. The methods for generating these load estimates are described below and elsewhere (Gruber et al., 2020; Gruber et al., 2019) and form an integral part in mapping the superficial dispersion of land-derived nitrogen and sediment in the GBR as part of the GBR Marine Monitoring Program, managed by GBRMPA in collaboration with AIMS and other partners (James Cook University, Howley Environmental Consulting and Cape York Water Monitoring Partnerships). Briefly, the total river discharge for each basin was calculated using an approach that up-scaled available measured gauge flow data (i.e. the flow gauges rarely capture the full basin area and hence underestimate flow from the basin); available Grid-to-Grid (G2G) modelling (covers the Normanby to Mary Basins) from the Bureau of Metrology (Bureau of Meteorology, 2017; Wells et al., 2017) was used to inform the upscale factors for the flow data. An area-correction factor was applied to the four basins north of the Normanby (i.e. not modelled by G2G) and for basins which had no available flow data the flow gauge data from the nearest neighbour basin was applied (along with the relationship with the G2G model to produce the upscale factor) to calculate discharge (Gruber et al., 2020).

The TSS loads for the river basins of the GBR were derived from a systematic approach which included: 1. The measured TSS loads from the Burdekin, Pioneer and Fitzroy basins were compiled from the Great Barrier Reef Catchment Loads Monitoring Program (annual reports each year from 2010: https://www.reefplan.qld.gov.au/tracking-progress/paddock-to-reef/modelling-and-monitoring) as well as previous programs from the Burdekin (Kuhnert et al., 2012), Pioneer (Joo et al., 2012); note that for the 2002/03 to 2005/06 water years, an annual mean concentration (AMC) of 112 mg.L^{-1} was applied to calculate the load for this basin) and Fitzroy (Joo et al., 2012; Packett et al., 2009) basins. As the loads measured at these sites capture >95% of the basin area they provide the most accurate measure at these locations; 2. For the remaining basins with available monitoring data, the AMC data (i.e. load divided by flow) from available load monitoring data within the basin were compared with the Source Catchments model outputs (McCloskey et al., 2017). The most appropriate AMC (or a mean of the monitoring and modelled data) was chosen and multiplied by the annual discharge (calculated from the above method) to formulate an annual load for these basins; 3. Where no monitoring data were available in the basin, the AMC informed from the Source Catchments model (McCloskey et al., 2017) and data from neighbouring basins with similar climate and geomorphology was coupled with the annual water year river discharge to calculate the TSS load (Gruber et al., 2019). The Source Catchments model produces a load that represents a ~30-year long term mean load (McCloskey et al., 2017) but excludes annual water year loads. Like the TSS loads, the DIN loads for the river basins of the GBR were similarly derived from a systematic approach which included: 1. The measured DIN loads from the Burdekin, Pioneer and Fitzroy basins from the same sources listed for the TSS method; 2. The method of Lewis et al. (2014) was applied to calculate DIN loads for the basins of the Wet Tropics and the Haughton Basin. Briefly, modelled DIN loads in this method were calculated using existing load monitoring data to develop a relationship between the measured loads with flow volumes (at river monitoring sites) and the amount of fertiliser applied to calculate the percentage of applied nitrogen fertiliser lost as DIN across various discharge amounts. This relationship is then applied to upscale loads for the entire basin area; 3. For the remaining basins, similar to the TSS loads method, the AMC data from available load monitoring were compared with the Source Catchments model outputs and the most appropriate AMC (taking into account the cropping area above and below the measured site) was chosen for each basin and multiplied by the annual discharge to formulate an annual load; 4. Where no monitoring data were available, the AMC informed from the Source Catchments model (McCloskey et al., 2017) and data from neighbouring basins with similar climate and geomorphology was coupled with the annual water year river discharge to calculate the water year loads (Gruber et al., 2019). Resulting TSS and DIN loads and river discharge were presented as stacked bar graphs.

Table 6. Relative contributions of the major rivers considered for each of the NRM regions in estimating loads of total suspended sediment (TSS), dissolved inorganic nutrient (DIN) and discharge.

Region (current study)	Region (Fabricius et al., 2016b)	Relevant rivers Water Quality Index
Cape York	Cape York	Normanby, Endeavour, Stewart
Wet Tropics: (North Wet Tropics + South Wet Tropics)	North Wet Tropics	Daintree, Barron, Russell, Mulgrave, Johnstone, Burdekin (30% of discharge)
	South Wet Tropics	Russell, Mulgrave, Johnstone, Tully, Herbert, Burdekin (50% of discharge)
Dry Tropics	Burdekin	Burdekin
Mackay-	Whitsundays	Proserpine, O'Connell, Pioneer
Fitzroy	Broad Sound-Pompey, Keppel Bay	Fitzroy
Burnett-Mary	Fitzroy-Swain	Burnett

We then compared the annual river load estimates and the proposed bPAR index using simple linear regression analysis to highlight the drivers of variability in the bPAR index from year to year. We focused the comparison using the annual I_{bPAR} based on the light threshold for corals and the estimate of the total river loads and discharge relevant for each of the zones. It is important to note that the overall flow and transport of materials from the rivers along the length of the GBR is often northward (Devlin and Brodie, 2005) along the coast (i.e., due to Coriolis effects and SE trade winds) which means that the NRM regions may also receive inputs from other rivers situated in adjacent NRM regions (zones) (Skerratt et al., 2019). The total discharge for each NRM region was hence obtained by aggregating estimates for main influential rivers for each region following Fabricius et al. (2016b) (see Table 6). Note, however, that in the present study, estimates for the Fitzroy region are slightly different and that the Wet Tropics NRM region annual load estimate was combined and not separated to north and south sectors as in Fabricius et al. (2016b).

4.3 Results

4.3.1 Defining a light threshold for calculating benthic light stress

Considering the ranges of benthic light requirements of both corals and seagrasses described in Section 4.2.4 and examining the inflection point of the P-E curve presented in DiPerna et al. (2018) and the results of Strahl et al. (2019), we employed a benthic PAR threshold of 16 mol photons m^{-2} d^{-1}. This was chosen as the value likely to reflect the maximum usable PAR for most species. *Ad hoc* sensitivity analysis using other benthic light thresholds (i.e., 5, 10 and 14 mol photons m^{-2} d^{-1}) produced an index with less sensitivity to known regional and temporal variations. We note that the selected 16 mol photons m^{-2} d^{-1} threshold value represents the maximum amount of benthic light that both target benthic organisms will be able to make use of to attain optimal growth if other environmental conditions are optimal, rather than the minimum light below which net productivity will be negative regardless of other conditions. In other words, corals and seagrasses can and do exist in areas where the mean daily light is above or below 16 mol photons m^{-2} d^{-1}, but their survival and growth can be expected to be enhanced with increasing daily integrated light up to around 16 mol photons m^{-2} d^{-1}, and not substantially enhanced above this threshold.

In the case of seagrass habitat suitability, additional and more recent sensitivity analyses described in Section 6.3 found that for most species a threshold of 12 mol photons m^{-2} d^{-1} yielded improved predictive power. For simplicity, however, results presented in the remainder of the current chapter use a unified threshold of 16 mol photons m^{-2} d^{-1} for both corals and seagrasses.

4.3.2 Cumulative benthic light stress

The cumulative benthic light stress (S) within the GBR varied strongly both spatially and temporally. Figure 2 shows maps of S for selected water years highlighting this variability. Benthic light stress consistently showed greater variability in inshore locations compared to offshore areas. For example, the open coastal locations in the 2005 – 2006 'dry' (e.g., period where below average rainfall was recorded by the Australian Bureau of Meteorology) water year (Figure 2a) showed relatively low stress, but indicated considerably higher values in the 'wet' water years 2010 – 2011 (Figure 16b) and 2018 – 2019 (Figure 16c).

4.3.3 Annual bPAR index

The timeseries of the annual I_{bPAR} based on the relative benthic light stress showed strong interannual variation as well as spatial variation between the zones (Figure 17). Regional differences followed latitudinal gradients. From north (Cape York) to south (Burnett-Mary), the annual I_{bPAR} showed an overall decreasing trend that was consistent across all the shelf water bodies except the enclosed coastal water body to some extent. Out of all the NRM regions, Cape York consistently showed the best water quality throughout the 2003 to 2019 water years (i.e., indicated the most water years with letter grade A – "very good" bPAR index value).

The annual I_{bPAR} also showed an across-shelf gradient decreasing from offshore to inshore coastal water bodies. Notably, there was an overall higher variability in I_{bPAR} for the two most inshore locations compared to the midshelf and offshore locations across all NRM regions, the latter having consistently excellent water quality conditions. The annual fluctuations in bPAR index values in the inshore water bodies appear strongest from the 2010 water year although some fluctuations in prior years can also be noted particularly in the Dry Tropics and Mackay-Whitsunday NRM regions. Overall, the temporal variations in the annual I_{bPAR} (Figure 17) suggest that the strong local influences of nearshore processes that drives light attenuation at depth.

Specific variability in the annual water quality during certain years can further be inferred in the I_{bPAR} timeseries. For example, in the 2010-2011 water year there was a notable decline in the I_{bPAR} across all NRMs (except for the Cape York region). This decline is again most evident in the open coastal water body where the bPAR index grade drops by one step in most NRMs (e.g., “good” (B) to “moderate” (C) in Wet Tropics and Fitzroy) were obtained between the 2009-2010 and 2010-2011 water years. Following this, there were several other similar but smaller declines in I_{bPAR} during the other water years, but interestingly, the variability remained confined within the coastal inshore locations across all NRM regions particularly within the open coastal water body.

Figure 16: Cumulative (annual) benthic light stress (S) maps for two representative water years: top: 2005 – 2006 (the year with the lowest river discharge in the period for which we have bPAR data) and bottom: 2010 – 2011 (a high discharge year notable for the passage of Cyclone Yasi. Light stress scores highlight the strong spatial and temporal variability in the amount of light stress experienced by corals and seagrasses at each zone within the GBR. Nearshore areas are strongly influenced by river flood plumes, which vary from year to year, while offshore areas are less temporally variable, with reduced light in some pixels as a result of interaction between depth and water clarity. Areas in white do not contribute to the index due to low light even at 95th percentile bPAR (e.g. due to depth). Pixels are approximately 1 km^2.

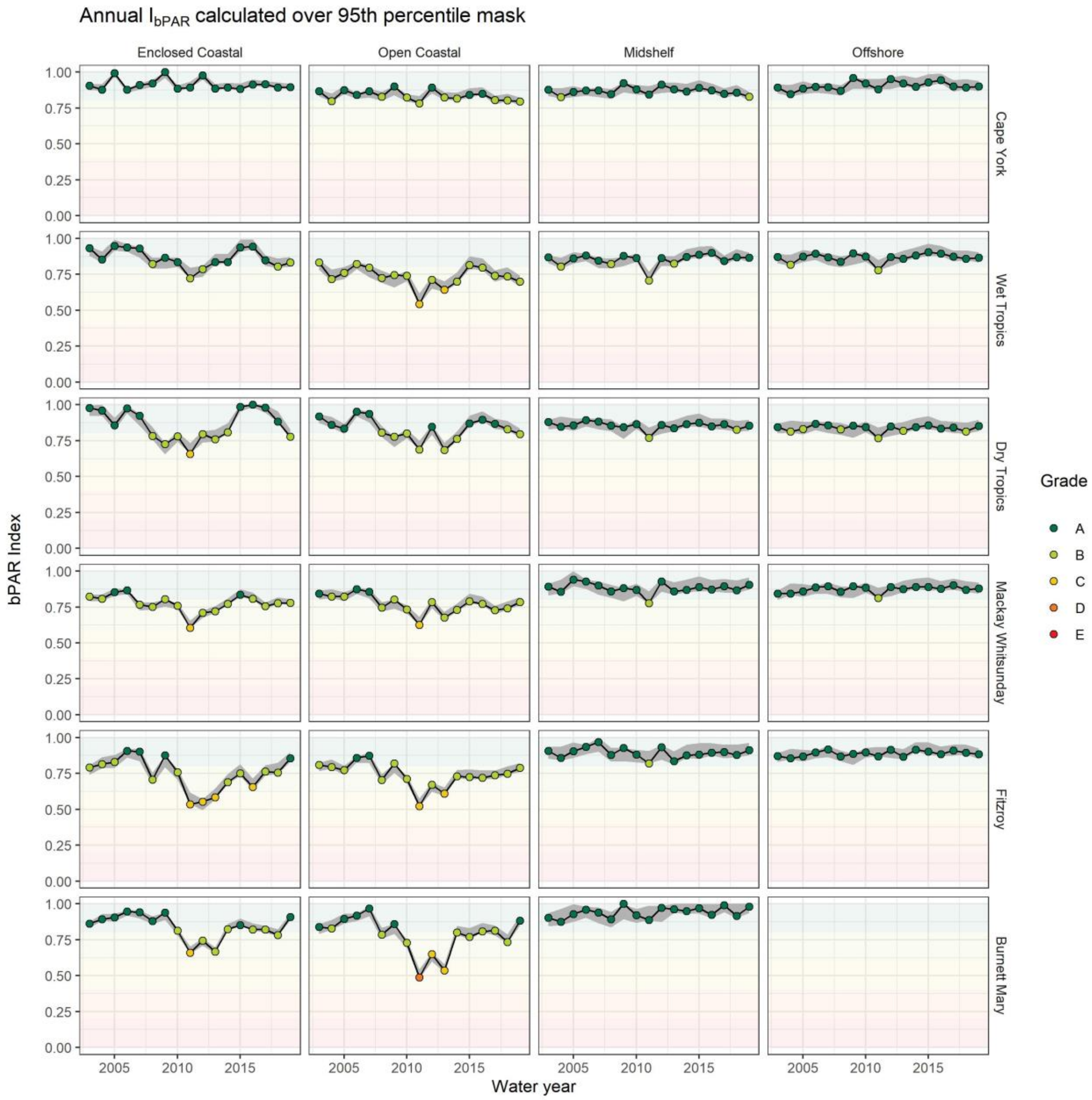

Figure 17: Timeseries of scaled annual bPAR index (I_{bPAR}) for water years (2002 – 2003) to (2018 – 2019) over locations within the 95th percentile of bPAR values ≤ 16 mol photons m^{-2} d^{-1}. Colours correspond to letter grades that indicate the quality of the water as: very good (A, dark green), good (B, light green), moderate (C, yellow), poor (D, orange), and very poor (E, red). Index values are not calculated for the Offshore Burnett-Mary NRM region because there are insufficient valid pixels of data (at 1 km^2 resolution, this small region contains no shallow pixels). Grey shaded bands show the 95th percent confidence interval of error introduced by the remote sensing algorithm for daily integrated benthic PAR. Other sources of error, including cloud cover and sub-grid depth variations, have not been taken into account.

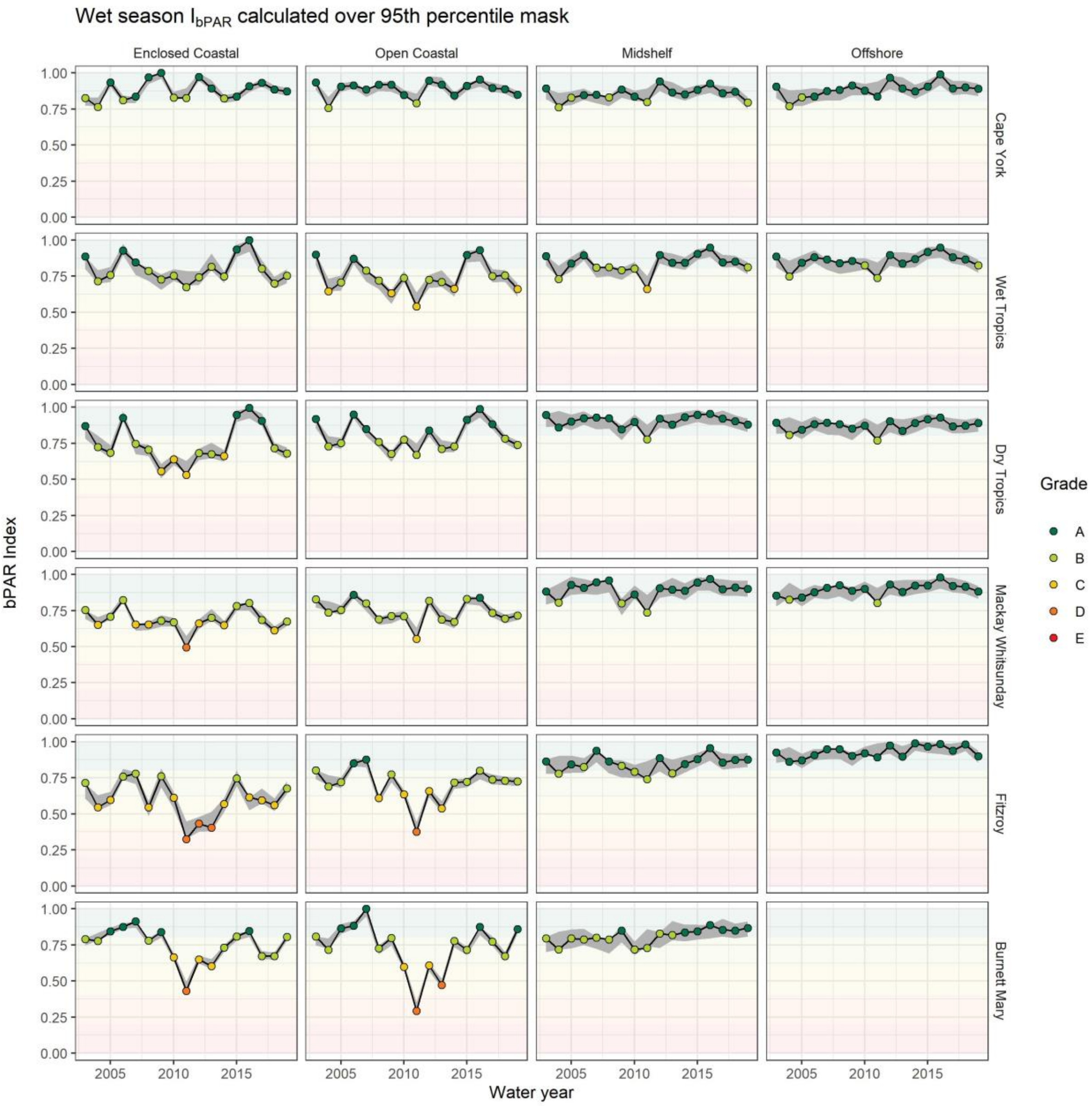

Figure 18: Timeseries of scaled wet-season bPAR index (I_{bPAR}) for water years (2002 – 2003) to (2018 – 2019) over locations within the 95th percentile of bPAR values ≤ 16 mol photons m^{-2} d^{-1} integrated over austral wet-season period (01 November to 30 April during each 'water year'). Colour legend same as Figure 17. Index values are not calculated for the Offshore Burnett-Mary NRM region because there are insufficient valid pixels of data (at 1 km^2 resolution, this small region contains no shallow pixels). Grey shaded bands show the 95th percent confidence interval of error introduced by the remote sensing algorithm for daily integrated benthic PAR. Other sources of error, including cloud cover and sub-grid depth variations, have not been taken into account.

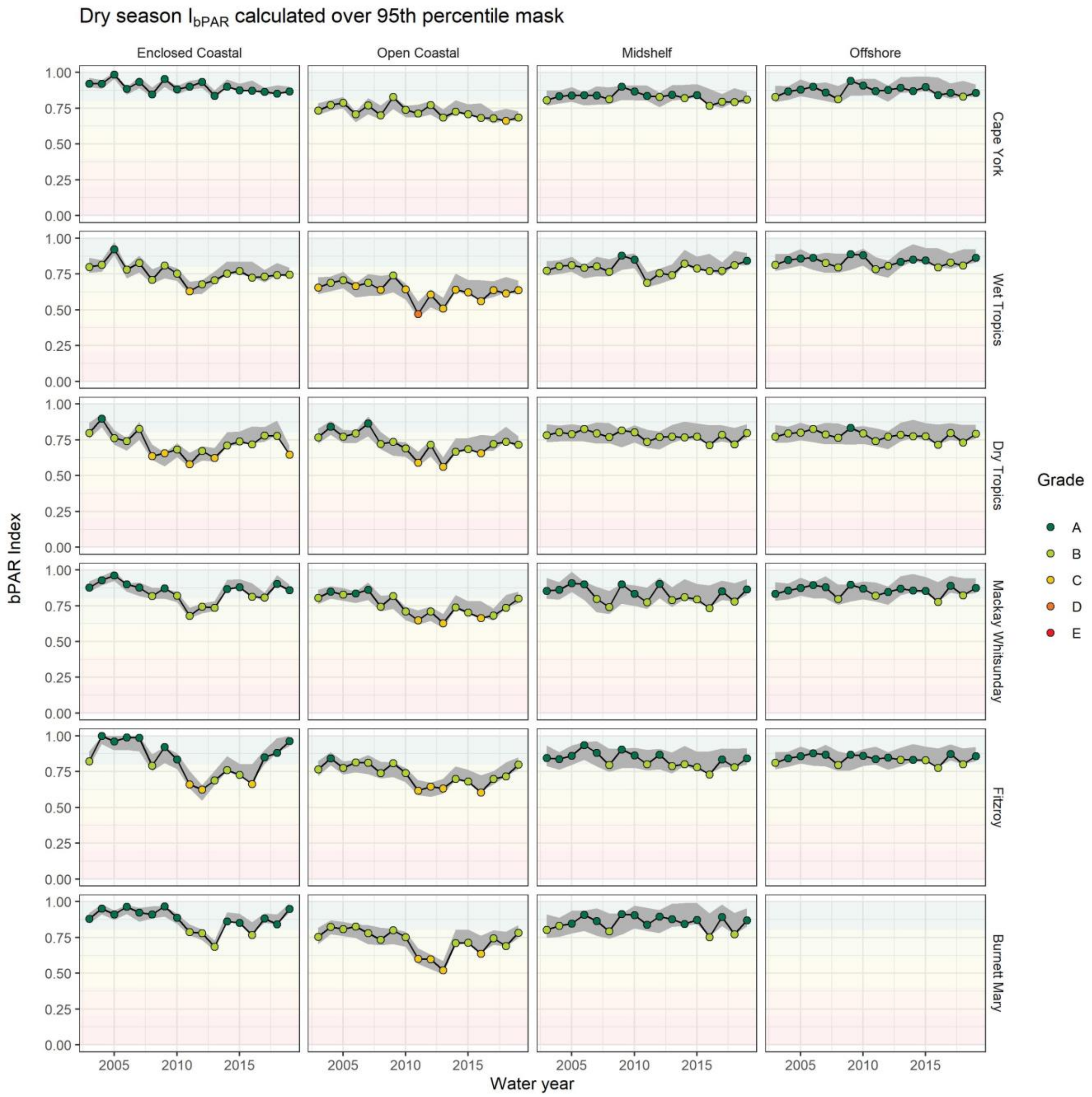

Figure 19: Timeseries of scaled dry-season bPAR index (I_{bPAR}) for water years (2002 – 2003) to (2018 – 2019) over locations within the 95th percentile of bPAR values ≤ 16 mol photons m^{-2} d^{-1} integrated over austral dry-season period (01 May to 31 October during each 'water year'). Colour legend same as Figure 17. Grey shaded bands show the 95th percent confidence interval of error introduced by the remote sensing algorithm for daily integrated benthic PAR. Other sources of error, including cloud cover and sub-grid depth variations, have not been taken into account.

4.3.4 Seasonal benthic light-based water quality index

Seasonal variations in bPAR are due to both variations in incident PAR at the surface and water quality. Our analyses show that there is a 20% difference between winter and summer surface PAR in the North of the GBR, increasing to a 60% difference in the South. Our seasonal bPAR indices account for the seasonal surface PAR variations by considering only the reduction in bPAR below the achievable bPAR for each calendar month given optimal water quality.

Inter- and intra-seasonal differences were apparent for the austral wet (Figure 18) and dry (Figure 19) season I_{bPAR}. The intra-seasonal patterns also displayed the same north-south latitudinal or across-shelf gradients as also observed in the annual data (Figure 17) where the midshelf and offshore water bodies again showed more consistent and less variable I_{bPAR}, while the inshore locations (both enclosed coastal and open coastal) showed stronger variability. The timeseries of I_{bPAR} indicated the stronger sensitivity of the nearshore water bodies to long-term reductions in benthic light availability (i.e., lower I_{bPAR} grade for the same 'water year' and zone).

Inter-seasonal differences between the seasonal indices indicated more pronounced variabilities during the austral wet than the austral dry season similarly with cross-shelf spatial differences being more notable in the two inshore water bodies compared to the midshelf and offshore locations.

4.4 Discussion

This study presents a novel method for calculating a index of water quality in the GBR that is responsive to changes in the quantity of light reaching corals and seagrasses. We used spatiotemporally-rich satellite-derived bPAR as a core input data along with a benthic light threshold to calculate the cumulative benthic light stress parameter, *S*, the cumulative amount of light lost (relative to a maximum benthic light threshold) where corals and seagrasses were potentially photolimited due to reduced light availability (i.e., from poor water quality). Many locations nearshore indicated as much as 500 mol photons m^{-2} yr^{-1} growth potential lost from light limitation stress (Figure 16). The *S* parameter served as the basis of the new bPAR index reported here as annual or seasonal values scaled for each NRM region and shelf water body between 0 and 1 indicating 'very poor' (very high light stress) and 'very good' (no light stress) water quality conditions, respectively. Our results showed that the benthic light stress and hence the proposed benthic light-based index (I_{bPAR}) vary both spatially and temporally within the six NRM focus regions and four coastal water bodies. Latitudinal patterns can be generalised as decreasing from north (Cape York) to south (Burnett Mary) while the cross-shelf gradients generally decrease towards the coast (e.g., higher benthic light stress calculated nearshore). Confidence is highest in the Midshelf region where the remote sensing benthic light data product has been validated, and lowest in the optically complex nearshore region.

The observed patterns are closely related to the dynamics of key water quality drivers that may include river discharge (and the related factors such as suspended sediment concentrations) and potentially to occurrence of atmospheric and physical disturbances (cyclones, wind, wave and tidal mixing) as well as the local oceanography that governs the transport and hydrodynamics of river or flood plumes within the shelf. While the inshore locations typically receive higher daily light doses due to greater potential for light penetration because of shallow bathymetry (Ackleson, 2003), the annual light stress maps (Figure 16) and I_{bPAR} timeseries (Figure 17 to Figure 19) showed that these coastal locations are most vulnerable to declines in benthic light levels compared to the midshelf and offshore locations due to both river plumes and resuspension. River flood plumes within the GBR can, in very wet years, simultaneously occur from the Cape York to Burnett-Mary regions but mostly impact areas within 20 km inshore, occasionally reaching beyond the midshelf regions (Devlin et al., 2012) and often spread in a band up to 50 km from the coast (Devlin and Brodie, 2005). The overall patterns we obtained in this study were also consistent with previous simulations (Skerratt et al., 2019) of the spatial distribution of some water quality parameters directly related to or considered a proxy for light availability at depth. For example, simulated Z_{sd} from Skerratt et al. (2019) was generally greater offshore and decreased as distance from shore decreased, and from north to south, while Chl *a* concentration increased from north to south and from outer to inner coastal regions. Higher concentrations of Chl *a* are generally associated with higher light attenuation (thus, reduced light availability) and in the context of this study, high light-stress (or increased stress from light attenuation) and a low I_{bPAR}.

4.5 Conclusion and future directions

We have presented a new method for developing an index of water quality based on the amount of benthic light reaching corals and seagrasses. Our method uses two core pieces of information. First, GBR-wide estimates of $bPAR_d$ obtained from a remote sensing algorithm allowed assessment of historical light conditions within the GBR on a near-daily time-step over the 17.5 years from July 2002 to December 2019. Second, we specified a combined (coral and seagrass) benthic light threshold that denotes the maximum amount of light that key coral and seagrass species can potentially use to maintain growth, above which very little increase in photosynthetic efficiency can be expected. We combined these two sets of information to derive the relative benthic light stress parameter – the stress on benthic habitats due to low light conditions. This parameter was aggregated over each water year for each 1km x 1km pixels, scaled to a value between 0 and 1 for each management region, and then mapped out to a letter grade, A to E to indicate ‘very good’ (no light stress) to ‘very poor’ (very high light stress) water quality conditions which aligned with the current format used in GBR water quality report cards.

The annual and seasonal I_{bPAR} calculated for the six NRM focus regions (Cape York to Burnett-Mary) and four water bodies (enclosed coastal to offshore) showed strong spatial and temporal variability characterised by an overall latitudinal gradient that decreases from north (Cape York) to south (Burnett Mary) and a cross-shelf gradient that improves with distance from the coast. The overall patterns of the I_{bPAR} obtained were indicative of strong response to known drivers of water quality within the GBR (e.g., variability of river discharge and associated total suspended sediment loads and dissolved organic matter, cyclone and weather-related flood events, and the transport (hydrodynamics) of flood plume in the marine environment) and emphasises the importance of robust monitoring tools able to detect exposure of relevant benthic ecosystems to these drivers to better inform water quality management policies implemented within the GBR. Latitudinal and seasonal variations in irradiance incident at the surface are filtered out of the index by the use of the 95th percentile bPAR for each pixel in each calendar month as the maximum reference bPAR in calculating light stress.

The sensitivity of the proposed method to variations in drivers of water quality highlights the ability of the new index to map changes in light availability and demonstrates its potential as a robust alternative to the metric currently used in Reef Report Cards, i.e. photic depth (Z_{sd}). The bPAR index accounts for variations in bathymetry as well as the quality and quantity of light and employs a threshold that is directly relevant to photobiology. It therefore relates much more directly to ecological outcomes for corals and seagrasses than other water quality metrics such as turbidity or Z_{sd}.

Future work should include quantification of error in the bPAR data product in the nearshore region – in the present study, validation was limited to Midshelf and offshore locations.

5.0 DRIVERS OF VARIABILITY IN BENTHIC LIGHT

5.1 Introduction

While the literature reviewed in Section 4.2.4 clearly shows that corals and seagrasses respond to variations in water clarity and bPAR, there has been a great deal of popular discussion in recent times about whether water clarity in the GBR has changed and if so, what is driving this change. Previous work has clearly established that water quality varies in response to river discharge in nearshore waters (Devlin et al., 2012; Devlin and Schaffelke, 2009; Devlin and Brodie, 2005; Devlin et al., 2015b; Howley et al., 2018) and there is some evidence that year-to-year variations in river discharge impact water clarity over a much wider area, extending into the Midshelf waters, and in the Wet Tropics even affecting the Outer reefs (Fabricius et al., 2014; Fabricius et al., 2016a). It is also well established that the sediment and nutrient loads associated with river discharges to the GBR have dramatically increased due to coastal land development since European settlement (Brodie et al., 2012; Kroon, 2012; Kroon et al., 2016).

In this Chapter, we assess how regional and temporal variations in the annual value of the bPAR index, I_{bPAR}, respond to variations in river discharge, providing additional evidence for the link between catchment activities and GBR ecological outcomes, mediated by river discharge.

Figure 20: The amount of light that penetrates to the bottom of the water column is a function of water quality as well as depth. Here, rays of light from the surface shine through marine snow. Credit: Renata Ferrari.

5.2 Annual river discharge, total suspended sediment (TSS) and dissolved inorganic nutrient (DIN) loads

Distinct temporal variability in annual river discharges of freshwater (ML/year) and loads of total suspended solids (TSS, kt/year) and dissolved inorganic nitrogen (DIN, t/year) loads were observed for five major GBR river systems over the period covering the 2003 to 2019 water years (Figure 21). For freshwater, the estimated annual Burdekin River discharges were consistently larger than those from the four other rivers (Figure 21a), with the exception of the Fitzroy River in few 'water years'. TSS loads were also highest for the Burdekin River, followed closely by the Fitzroy River (Figure 21b). The other three river systems, while smaller in comparison to the Burdekin and Fitzroy River, still showed regionally significant loads and substantial variability over time.

GBR wide, the TSS load was highest for the Burdekin River, especially in the 2007-2008 water year with almost 15,000 kt/year, followed by water years 2008-2009 with almost 11,000 kt/year and 2018-2019 with 7000 kt/year. For Fitzroy River, the highest TSS load over the period covered occurred in the 2010-2011 water year with ~7,000 kt/year.

DIN loads were highest in the Herbert River, followed very closely by the Burdekin and Fitzroy rivers (Figure 21b). The largest cumulative DIN load estimates throughout the period considered were recorded in the 2010-2011 water year, with particularly large contributions from the Fitzroy and Herbert rivers.

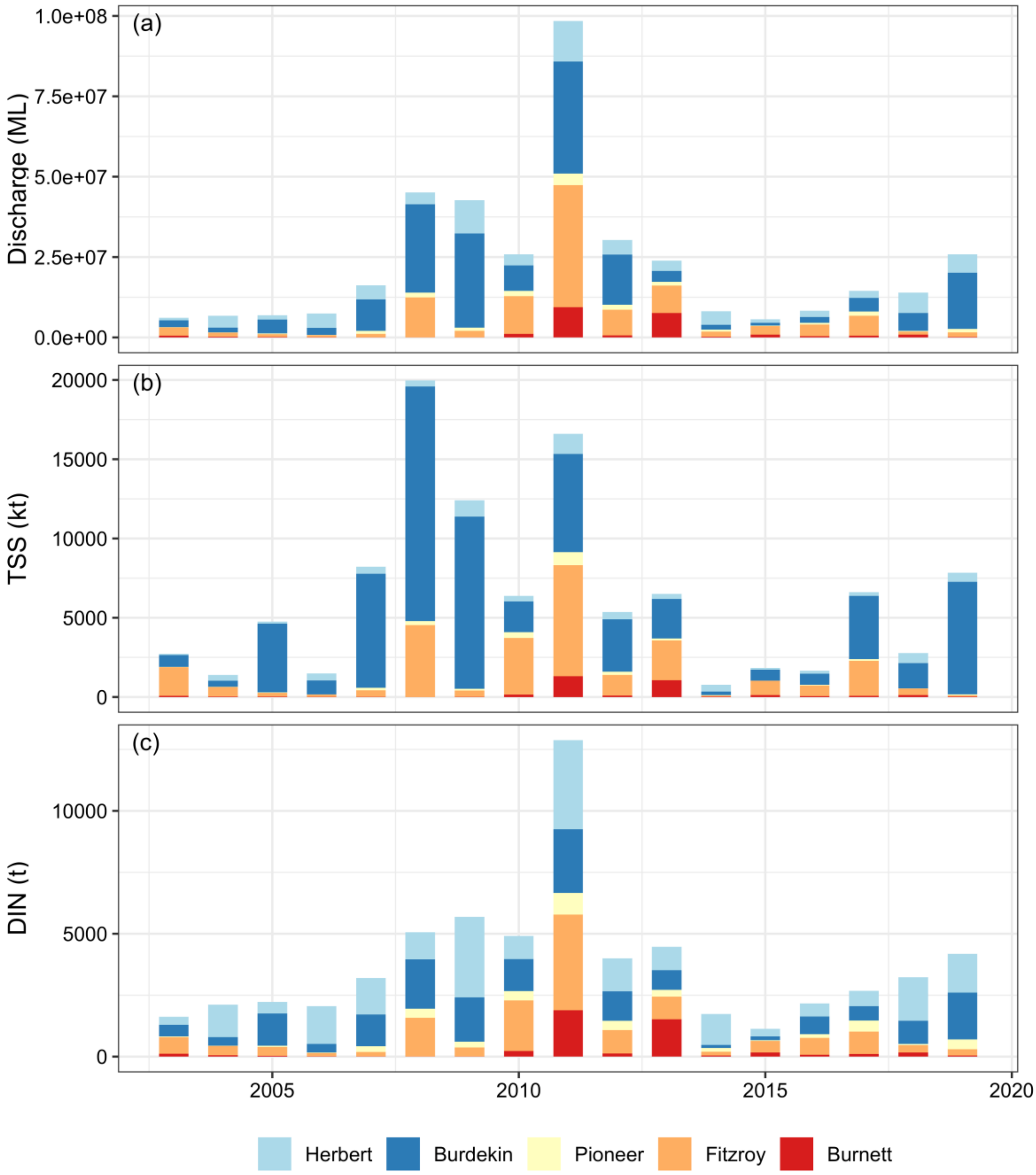

Figure 21: Annual estimates of (a) river freshwater discharge, (b) total suspended sediment (TSS), and (c) dissolved inorganic nutrients (DIN) loads calculated at selected five major rivers found along the length of the GBR. Colours indicate the associated river source.

5.3 Relationship between annual river loads and concentrations and the bPAR index

Simple linear regression analysis showed some strong relationships between the annual value of the bPAR index, I_{bPAR}, and annual estimates of river freshwater discharge and loads (both TSS and DIN). Slopes were negative for all NRM regions and all water bodies, i.e., higher discharges and loads were associated with lower I_{bPAR} values. Typically, regression slopes were steeper inshore (namely the enclosed coastal and open coastal water bodies), particularly in the southern NRM regions, compared to the midshelf and offshore waters (Table

7, Figure 22). This is consistent with the strong latitudinal and cross-shelf gradients observed in the I_{bPAR} time series.

For river freshwater discharges, the correlations between I_{bPAR} and Discharge were strongest (see R^2 values in Table 7) in the inshore locations for Mackay Whitsunday enclosed coastal and Fitzroy open coastal zones. North of these zones, respectively, Dry Tropics enclosed coastal and Mackay Whitsunday open coastal zones also showed comparable strong correlations. In the midshelf and open coastal water bodies, the correlations between I_{bPAR} and Discharge were strongest in the Wet Tropics, followed by the Dry Tropics.

For TSS load, the correlations between I_{bPAR} and TSS load showed a similar pattern except that the highest R^2 values for the midshelf and offshore waterbodies were noted in the Cape York NRM instead.

For DIN load, the correlations to I_{bPAR} were strongest in the inshore locations in the Mackay Whitsunday-enclosed coastal and Burnett Mary-open coastal zones, while Wet Tropics showed highest correlation coefficients in the water bodies away from the coast.

Overall, the relationship between I_{bPAR} and the three river-derived parameters (discharge, TSS and DIN) appear to be generally stronger in the inshore water bodies for the southern NRMs (Mackay Whitsundays, Fitzroy and Burnett Mary) and away from the coast for the northern NRMs (Dry and Wet Tropics and Cape York). Additionally, the correlation coefficients obtained for all three parameters against the I_{bPAR} are also comparably strong for the Dry Tropics-enclosed coastal water bodies.

Table 8 and Figure 23 show a similar analysis, with I_{bPAR} regressed against mean annual river TSS and DIN concentrations instead of river loads. There is substantial scatter around these regressions, and in the coastal waterbodies the relationship between TSS and DIN concentrations and I_{bPAR} is often inverse: high average concentrations are often associated with lower total loads as there is less dilution of catchment loads when discharge is low.

Table 7: Summary of linear regression statistics of I_{bPAR} versus DIN, freshwater discharge and TSS for each water body and NRM Region. Highlighted cells indicate the strongest correlation (i.e., highest the R^2 value) for each category and water body. Values in bold indicate very close R^2 values to the highest R^2. Abbreviations: EC, enclosed coastal; OC, open coastal; Mid, midshelf; Off, offshore. The methods used to generate load estimates have also been described in recent GBR Marine Monitoring Program reports (Gruber et al., 2020; Gruber et al., 2019)

		Discharge				**TSS load**				**DIN load**			
Region	**Statistics**	**EC**	**OC**	**Mid**	**Off**	**EC**	**OC**	**Mid**	**Off**	**EC**	**OC**	**Mid**	**Off**
Cape York	R^2	0.06	0.46	0.57	0.48	0.06	0.46	0.56	0.47	0.06	0.46	0.57	0.48
	intercept	0.95	0.92	0.95	0.97	0.95	0.93	0.95	0.97	0.95	0.92	0.95	0.97
	slope	-0.03	-0.06	-0.06	-0.03	-0.03	-0.06	-0.06	-0.03	-0.03	-0.06	-0.06	-0.03
Wet Tropics	R^2	0.26	0.53	0.75	0.53	0.04	0.17	0.39	0.33	0.20	0.53	0.74	0.52
	intercept	0.94	0.89	0.94	0.93	0.92	0.85	0.93	0.93	0.94	0.89	0.95	0.93
	slope	-0.07	-0.18	-0.10	-0.06	-0.02	-0.09	-0.06	-0.04	-0.06	-0.19	-0.11	-0.06
Dry Tropics	R^2	**0.62**	0.27	**0.69**	**0.52**	0.33	0.10	0.29	0.17	0.55	0.22	0.56	0.37
	intercept	0.95	0.93	0.96	0.92	0.94	0.93	0.95	0.92	0.96	0.94	0.97	0.93
	slope	-0.15	-0.09	-0.11	-0.03	-0.13	-0.06	-0.08	-0.02	-0.15	-0.09	-0.10	-0.03
Mackay Whitsunday	R^2	0.71	0.53	0.32	0.08	0.66	0.47	0.30	0.11	0.71	0.54	0.32	0.07
	intercept	0.84	0.87	0.94	0.94	0.84	0.86	0.93	0.94	0.84	0.87	0.94	0.94
	slope	-0.13	-0.15	-0.10	-0.02	-0.13	-0.15	-0.10	-0.02	-0.13	-0.15	-0.09	-0.02
Fitzroy	R^2	0.44	0.68	0.21	0.01	0.39	0.58	0.25	0.00	0.40	**0.63**	0.26	0.01
	intercept	0.86	0.84	0.95	0.94	0.86	0.85	0.95	0.94	0.86	0.85	0.95	0.94
	slope	-0.21	-0.26	-0.05	0.01	-0.18	-0.22	-0.05	0.00	-0.19	-0.25	-0.06	0.01
Burnett Mary	R^2	0.50	**0.62**	0.18	N/A	0.44	**0.56**	0.24	N/A	0.54	0.65	0.19	N/A
	intercept	0.91	0.90	0.98	N/A	0.92	0.92	0.98	N/A	0.92	0.91	0.98	N/A
	slope	-0.22	-0.39	-0.04	N/A	-0.19	-0.35	-0.05	N/A	-0.22	-0.39	-0.04	N/A

Table 8: Summary of linear regression statistics of I_{bPAR} versus river DIN annual mean concentration, freshwater discharge and river TSS annual mean concentration for each water body and NRM Region. Highlighted cells indicate the strongest correlation (i.e., highest the R^2 value) for each category and water body. Values in bold indicate very close R^2 values to the highest R^2. Abbreviations: EC, enclosed coastal; OC, open coastal; Mid, midshelf; Off, offshore. The methods used to generate load estimates have also been described in recent GBR Marine Monitoring Program reports (Gruber et al., 2020; Gruber et al., 2019)

		Discharge				TSS concentration				DIN concentration			
Region	**Statistics**	**EC**	**OC**	**Mid**	**Off**	**EC**	**OC**	**Mid**	**Off**	**EC**	**OC**	**Mid**	**Off**
Cape York	R^2	0.06	0.46	0.57	0.48	0.06	0.46	0.56	0.47	0.06	0.46	0.62	0.51
	intercept	0.95	0.92	0.95	0.97	0.95	0.93	0.95	0.97	0.95	0.93	0.94	0.97
	slope	-0.03	-0.06	-0.06	-0.03	-0.03	-0.06	-0.06	-0.03	-0.04	-0.07	0.00	0.00
Wet Tropics	R^2	0.26	0.53	0.75	0.53	0.04	0.17	0.39	0.33	0.21	0.57	0.77	0.54
	intercept	0.94	0.89	0.94	0.93	0.92	0.85	0.93	0.93	0.93	0.87	0.94	0.93
	slope	-0.07	-0.18	-0.10	-0.06	-0.02	-0.09	-0.06	-0.04	-0.06	-0.06	-0.05	-0.04
Dry Tropics	R^2	**0.62**	0.27	**0.69**	**0.52**	0.33	0.10	0.29	0.17	0.58	0.30	0.65	0.43
	intercept	0.95	0.93	0.96	0.92	0.94	0.93	0.95	0.92	0.95	0.93	0.95	0.92
	slope	-0.15	-0.09	-0.11	-0.03	-0.13	-0.06	-0.08	-0.02	-0.09	0.00	-0.02	-0.01
Mackay Whitsunday	R^2	0.71	0.53	0.32	0.08	0.66	0.47	0.30	0.11	0.72	0.54	0.32	0.12
	intercept	0.84	0.87	0.94	0.94	0.84	0.86	0.93	0.94	0.84	0.87	0.94	0.94
	slope	-0.13	-0.15	-0.10	-0.02	-0.13	-0.15	-0.10	-0.02	-0.15	-0.17	-0.11	0.02
Fitzroy	R^2	0.44	0.68	0.21	0.01	0.39	0.58	0.25	0.00	0.44	0.63	0.40	0.05
	intercept	0.86	0.84	0.95	0.94	0.86	0.85	0.95	0.94	0.87	0.85	0.96	0.95
	slope	-0.21	-0.26	-0.05	0.01	-0.18	-0.22	-0.05	0.00	-0.32	-0.29	-0.15	-0.03
Burnett Mary	R^2	0.50	**0.62**	0.18	N/A	0.44	0.56	0.24	N/A	0.61	0.71	0.39	N/A
	intercept	0.91	0.90	0.98	N/A	0.92	0.92	0.98	N/A	0.94	0.94	0.99	N/A
	slope	-0.22	-0.39	-0.04	N/A	-0.19	-0.35	-0.05	N/A	-0.44	-0.71	-0.16	N/A

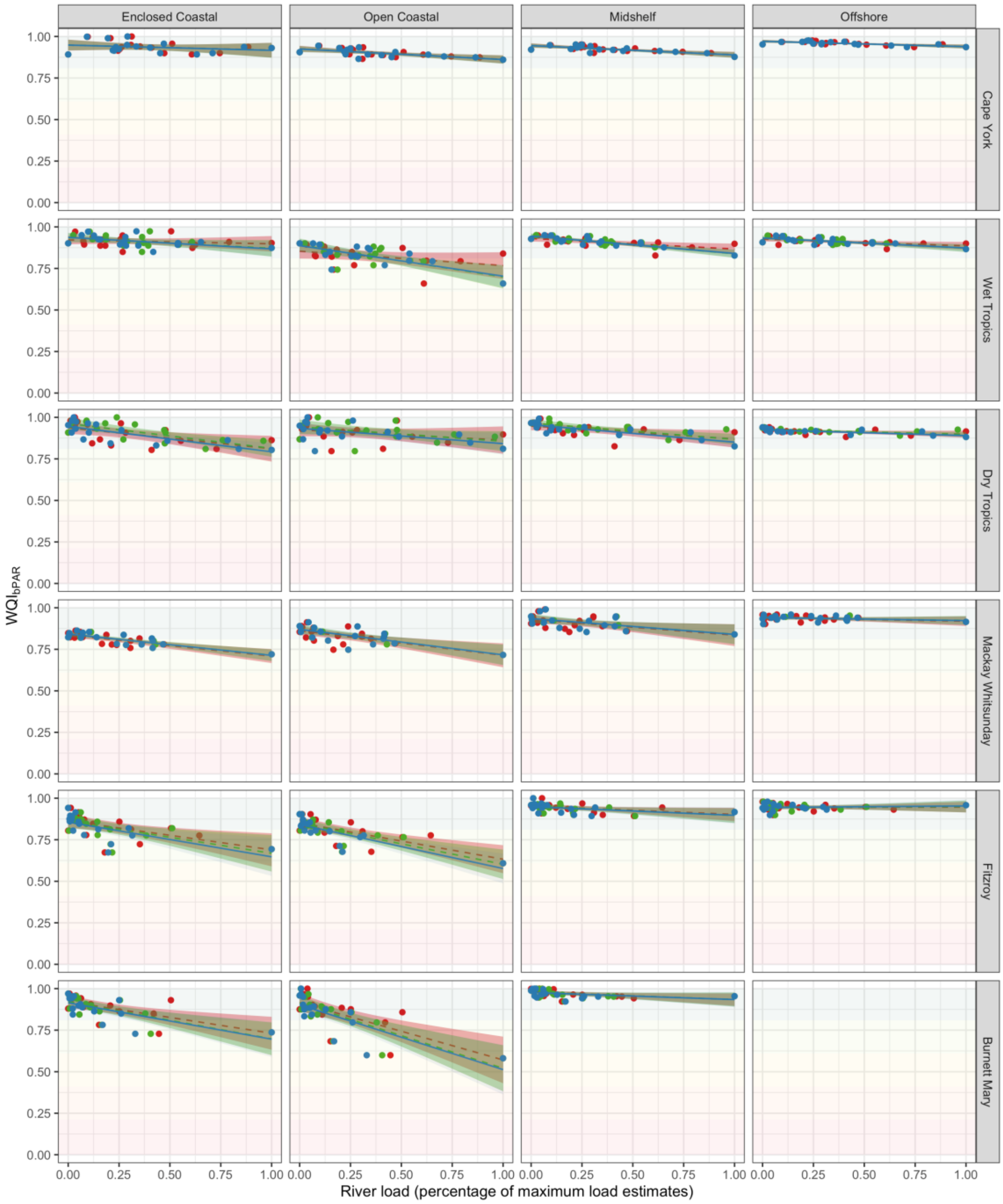

Figure 22: Scatterplots of scaled annual river loads of freshwater (blue-filled circles), DIN load (green-filled circles) and TSS load (red-filled circles) for each region versus annual I_{bPAR} for each zone. For each region, river loads are scaled from 0 (the minimum observed load) to 1 (the maximum observed load for that region). Also shown are the 95% confidence interval indicated as shaded areas: TSS load (red), DIN load (green), and freshwater (blue) with the mean fitted line: TSS load (red dashed line), DIN load (green dashed line), and river freshwater discharge (blue solid line).

Figure 23: Scatterplots of scaled annual river loads of freshwater (blue-filled circles), DIN mean annual river concentration (green-filled circles) and TSS mean annual river concentration (red-filled circles) for each region versus annual *I_{bPAR}* for each zone. For each region, river loads are scaled from 0 (the minimum observed load) to 1 (the maximum observed load for that region). Also shown are the 95% confidence interval indicated as shaded areas: TSS load (red), DIN load (green), and freshwater (blue) with the mean fitted line: TSS load (red dashed line), DIN load (green dashed line), and river freshwater discharge (blue solid line).

5.4 Discussion

The light stress in some but not all regions and water bodies in the GBR, quantified as the bPAR index I_{bPAR}, is clearly responsive to terrestrial inputs of freshwater, TSS and DIN, delivered from GBR catchments via rivers (Figure 22, and Table 7). Inter-annual variability in I_{bPAR} in the southern NRM regions was mostly confined to the inshore, while in the northern regions, it extended into the midshelf water bodies, in agreement with previous analyses on changes in annual values of photic depth associated with changes in annual values of river loads (Fabricius et al. 2014, 2016).

The spatial patterns in I_{bPAR} also reflect the depth and width of the continental shelf – narrow and shallow in the north and much wider and often deeper in the south. The low correlations noted for the Mackay Whitsunday and Fitzroy in offshore zones likely reflect the width and deep depth of these water bodies, with the edge of the continental shelf located up to 200 km from the coast. Materials are generally retained nearshore (and resuspended) by local wind-driven and tidal circulations, and those moved into offshore water bodies can sink below the depth of wave resuspension. For most of the central and northern NRMs, the stronger correlations between I_{bPAR} and TSS in the midshelf and offshore waterbodies may be related to the significant loads from the Burdekin and Wet Tropics rivers, together with the narrow width and shallow depth of the continental shelf, leading to chronic light reductions in mid- and outershelf water bodies due to resuspension of bottom sediment materials during strong winds. The role of potential drivers of variability in I_{bPAR} was explored via linear regression analysis (Figure 22 and Table 7). This analysis confirmed the strong association between river-discharge and I_{bPAR}, especially in the southern inshore NRMs and in most of the northern NRMs in the water bodies away from the coast. However, as there are typically strong correlations between estimates of annual river discharges and TSS and nutrient loads for the GBR rivers (Fabricius et al. 2016), the specific roles of each of the three potential drivers of reductions in I_{bPAR} could not readily be separated.

A comparison with regressions against river DIN and TSS concentrations (Figure 23 and Table 8) further highlights the dominant role of discharge (vs. concentration) in the impact of river loads on benthic light. River concentrations of sediments and nutrients affect benthic light in river flood plumes, which exist for a short period of time (often only a few days) over a relatively small area (usually restricted to the immediate coastal zone). For the seasonal and annual timeframes that we are interested in here, river loads more relevant than concentrations. Bainbridge et al. (2018) have provided a review and conceptual description of the pathways through which sediments and nutrients from river discharges are transformed and transported from catchment to reef, with impacts over a much wider area and longer time-interval than the direct effects of flood plumes. Unlike concentrations, loads capture the total amount of material delivered to the coastal zone and subject to further processing, including resuspension of particulate material that may initially have been deposited near the river mouth over a short or long period of time, remineralisation of organic nutrients associate with these particulate materials, desorption of adsorbed phosphorus, and transportation in biogeochemically transformed forms to Midshelf waters.

At intra-annual time scales, many processes contribute to variability in I_{bPAR}. Specifically, the austral wet season (October through May) is generally associated with elevated river discharge in the Queensland tropical region, resulting in lower water clarity and increased (more frequent and/or more intense) light stress from light attenuation. Furthermore, nutrient and suspended sediment concentrations in the water can change in response to the combined effects of the transport of river-derived materials, clearly indicating its role in driving light reduction (Schaffelke et al., 2012), and due to wind and wave driven resuspension of material from the seafloor and biological response from increased nutrient availability especially in the inshore areas.

In Queensland, river discharges are often episodic, often linked to monsoonal low pressure systems or tropical cyclones (TC). Our Wet season I_{bPAR} reflects the immediate influence of major events (Figure 18) but also the subsequent effects related to resuspension and retention of flood-derived materials (Neil et al., 2002; Orpin and Ridd, 2012), and potentially the flood-induced changes in biological productivity due to reduced water quality and light reduction across most of the zones (Devlin and Schaffelke, 2009). It may also partially reflect the predominantly northward transport of materials by currents and wind waves along coastlines in the southern hemisphere via Ekman transport and Coriolis effects. While plumes may occasionally move out to the mid- or outer shelf during larger events that coincide with slack or northerly winds, pollutants that can cause light reduction beyond inshore regions are probably dispersed more quickly or deposited in the deeper zones which do not get resuspended again except potentially during strong currents generated by cyclonic conditions (Larcombe and Carter, 2004). For example, the 2011 water year was associated with flooding in Queensland as early as November – December 2010 (associated with TC Tasha, and severe TC Yasi in early January 2011), and low wet season I_{bPAR} values (Figure 18). For most of the southern NRMs, I_{bPAR} values returned (within two years) to the “moderate to good” range within the inshore water bodies after the marked decline during the 2010 - 2011 water year associated with high river discharges and TC Yasi. Before this, however, steady decline in water quality conditions even before 2011 can also be noted in the time series. Coincidentally, the recent inshore GBR Marine Monitoring Program report (Gruber et al., 2019) has indicated that inshore Z_{sd} in most NRMs have declined since 2005 and have not been meeting guideline values based on *in situ* water quality data collected at several point locations within the GBR nearshore waterbodies during the austral wet season.

Spatial and temporal variability in I_{bPAR} not only underscores the exposure risk of the inshore water bodies to light reduction due to runoff from nearby catchments, but also emphasises two key points. Firstly, it lends support to current policies and measures (i.e., Reef 2050 Water Quality Improvement Plan 2017-2022) that aim to improve the quality of the water that enters the GBR lagoon. Secondly, our results clearly demonstrate the sensitivity of the proposed index to capture light variability, with its direct impact on coral and seagrass ecosystems of the GBR, as will be explored in Chapter 6. Its ecological relevance highlights the potential for the proposed new I_{bPAR} index as a water quality metric to replace (or complement?) the currently used metric based on the combined Chl*a* and Z_{sd} sub-indicator data, while also meeting the requirements for spatial and temporal data coverage that is essential for studying a region as vast as the GBR.

6.0 ECOLOGICAL VALIDATION

6.1 Introduction

In Chapter 4.0, we described the development of a new indicator for water quality in the Great Barrier Reef, I_{bPAR}. This index is based on an ecological understanding of the light requirements of benthic organisms (especially corals and seagrasses) that was developed during NESP TWQ Project 2.3.1 (the predecessor of the current project) through SeaSIM experiments and a review of the published, peer-reviewed literature on coral and tropical seagrass light requirements.

In Chapter 5.0, we demonstrated that this index is sensitive to year-to-year variations in water quality across different NRM regions and that much of this variation explained by variations in river discharges and their nutrient and sediment loads (though other factors, including storms also play a role).

For I_{bPAR} to be adopted in monitoring and reporting, however, it is important to demonstrate that the index reflects and can help to explain variations in the distribution and health of seagrass and coral communities in the GBR. In this Chapter, we briefly describe analyses that have been conducted through collaboration with NESP TWQ Hub Project 5.2 (Uthicke et al., 2020) and NESP TWQ Hub Project 5.4 and describe in more detail an original analysis conducted as part of the present project in collaboration with the GBR Marine Monitoring Program.

6.2 Coral Community Composition and Performance

Figure 24: Light shining through water over a coral bommie. Credit: Renata Ferrari.

bPAR data layers developed during the course of this project have been provided to NESP TWQ Hub Project 5.2 for use in an analysis of the cumulative impacts of spatial and temporal variations in water quality, heat stress, storms, and crown of thorns starfish outbreaks on coral performance, where “performance” is a metric reflecting the difference between the observed reef state and the expected state in the absence of acute disturbances. A variety of statistical analyses were applied, including GAMM and REML modelling. In total, 25 potential water quality and disturbance metrics were assessed using coral performance data from 335 long term coral monitoring sites from the AIMS Long Term Monitoring Program and the GBR Marine Monitoring Program. While acute stressors, include storms, bleaching events and crown of thorns starfish outbreaks were found to have stronger effects on coral cover and performance, we also found PAR at 8 m to explain some of the variation in *Acropora* cover in the southern GBR and coral performance in the central GBR when year-to-year variability in PAR was taken into account.

Uthicke et al. (2020) describe the methods and results of these analyses in detail. The work has been submitted to a peer-reviewed international journal.

6.3 Seagrass Habitat Suitability

Chapter authors: Catherine Collier, Luke Hoffman, Barbara Robson and Alex Carter
The work presented in this chapter is being prepared for submission to a peer-reviewed international journal. It can be cited as “Collier, C., Hoffman, Robson, B. and Carter, A. (in

prep.) Seagrass distribution and community diversity in the Great Barrier Reef lagoon, Australia: Applications for spatial planning."

6.3.1 Introduction

Figure 25: GBR seagrass. Credit: Grace Frank.

Seagrass meadows are important habitats in the Great Barrier Reef (GBR) (Coles et al., 2015; Scott et al., 2020). They form diverse communities in the estuaries, coasts, on reef tops and in the deeper inter-reef areas of the lagoon, where the potential habitat is very large (Carter et al., in prep.). Benthic light levels are an important environmental variable influencing the distribution of seagrass species and seagrass communities (Carter et al., in prep.; Carter et al., submitted; Collier and Waycott, 2009; Waycott et al., 2005). Reductions in benthic light leads to lower productivity rates (Collier et al., 2018; Collier et al., 2011), and over time, leads to declines in the extent and amount of seagrass (Chartrand et al., 2016; Chartrand et al., 2018; Collier et al., 2012a), with flow on effects for the species that are dependent on them including iconic dugong and turtles (Preen and Marsh, 1995).

While the eReefs marine models can be used to predict changes in seagrass biomass, integrating the effects of variations in light, temperature and nutrient availability over time, they are currently limited to one or two seagrass groups and so are not able to resolve changes in community composition or the differing responses of different species (Baird et al., 2016a). Lambert et al. (2020) found that an eReefs RECOM application to Cleveland Bay did not reliably predict the distribution of *Halophilia* or *Zostera*. The same authors attempted to related observed changes in seagrass cover to fine sediment loads from GBR rivers to derive improved catchment targets for sediment loads, but found that the relationship between recent river loads, historical river loads and nearshore light conditions has not yet been sufficiently well characterised to allow this (Lambert et al., 2020).

Short-term light thresholds, below which seagrass growth rates and biomass declines, have been quantified for a number of species (Chartrand et al., 2016; Chartrand et al., 2018; Collier et al., 2016b), and estimated for most species on the GBR (Collier et al., 2016a). Longer-term light requirements are needed for broad-scale assessment of habitat suitability and for identifying the risk of changes to habitat suitability due to light limitation. Until recently, spatial light data has not been available for assessment of light levels across the distributional range of seagrasses; however, the benthic light product bPAR provides a spatially-explicit estimate of benthic light for the entire GBR (See Chapter 2.0). A new indicator of chronic light stress that can be used to monitor and report on water quality in the GBR has been described in Chapter 4.0, and is referred to here as the bPAR Index (I_{bPAR}).

The aims of this work were to examine long-term light levels suitable for seagrass species to inhabit. We examined both bPAR and I_{bPAR} as indicators of habitat suitability. To do this, we applied both bPAR and I_{bPAR} with thresholds ranging from 2 to 12 mol m^{-2} d^{-1} in seagrass species distribution models that use a range of environmental data and the seagrass composite (Carter et al., submitted) to predict suitable habitat (probability of species occurrence) of five seagrass species.

6.3.2 Methods

6.3.2.1 Data

The seagrass composite summarises 35 years of seagrass data collection (1984-2018) within the GBR into one GIS shapefile containing seagrass survey data as seagrass presence and absence for 81,387 sites (Carter et al., submitted). The data set is publicly available on e-atlas: https://eatlas.org.au/data/uuid/5011393e-0db7-46ce-a8ee-f331fcf83a88

This analysis uses data on seagrass presence of five seagrass species from the whole data set which overlapped with the environmental data set:

- *Cymodocea serrulata*
- *Halophila decipiens*
- *Halophila ovalis*
- *Halophila spinulosa*
- *Halodule uninervis*

6.3.2.2 Environmental predictors

Environmental data sets have been summarised by Carter et al. (in prep.) and included the long-term averages:

- Depth (metres below mean sea level; gbr30; intertidal sites MSL = 0m, (Beaman et al., 2016)).
- Benthic photosynthetically active radiation modelled from satellite images, bPAR, dry season from 2003-2020).
- Current speed (derived from eReefs marine models)

- Benthic geomorphology (Heap and Harris, 2008)
- Proportion of benthic sediment that is mud (derived from the eReefs marine models) (Steven et al., 2019)
- Tidal exposure (ITEM; subtidal sites ITEM = 0) (Bishop-Taylor et al., 2019)
- Salinity (eReefs)
- Water temperature (eReefs)
- Wave height (eReefs)
- Wind speed (eReefs)

6.3.2.3 General model analysis

We used Maximum Entropy (MaxEnt) software (version 3.4.1) to generate seagrass species distributions and potential distribution based on the complementary log-log (cloglog) link (Phillips et al., 2006; Phillips and Dudik, 2008). This assumes that the species' presence or absence at nearby sites (pixels) are independent, and is suitable for freely dispersed species such as seagrasses. MaxEnt models were generated using 10 replicate runs each with 10,000 background points and a maximum of 1000 iterations each. The convergence threshold was set to 10-5 with a regularisation multiplier of 1. Occurrence records were thinned to 100m resolution so only one point was present in each of the environmental layer cells. Model performance was assessed using Area Under the Curve (AUC) values which assesses model performance for binary data, and the percent variable contribution gained from jack-knife tests on each of the model runs (Bradie and Leung, 2017; Jayathilake and Costello, 2018; Phillips et al., 2006; Phillips and Dudik, 2008). The seagrass species distribution models are summarised by Carter et al. (in prep.). Two examples of the output are given below, one for *C. serrulata*, a shallow water specialist, and for *H. decipiens*, a deep-water specialist (Figure 26). The models including bPAR as a predictor variable are referred to hereafter as bPAR SDMs.

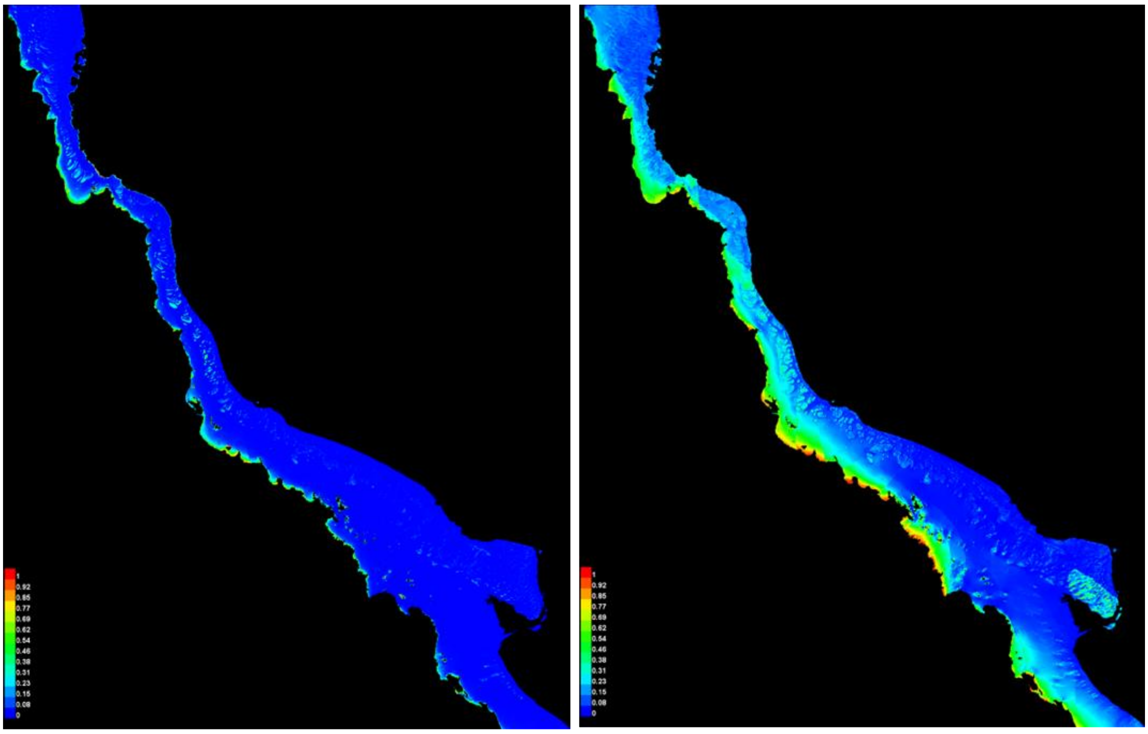

Figure 26: Habitat suitability for C. serrulata (left) and H. decipiens (right) ranging from 0-1 (coloured scale). From Carter, Hoffman et al. (In prep c)

Response curves demonstrating probability of each species presence were explored with bPAR in concert with all other variables. Full model outputs including response to other model variables are reported in Carter, Hoffman et al. (In prep c).

6.3.2.4 Threshold analysis

The I_{bPAR} Index is the cumulative stress due to benthic light levels falling below defined bPAR thresholds, as described in Chapter 4.0. The thresholds most relevant to seagrass species are tested here by exploration of threshold increments of 2 ranging from 2 to 12 mol photons m^{-2} d^{-1}. This testing range was based on outcomes of the SDMs outlined above and previous review of seagrass light thresholds (Collier et al., 2016c). For coral reefs, a threshold value of 16 mol photons m^{-2} d^{-1} has applied for the I_{bPAR} Index (see Section 6.4), while a lower range is likely to be more relevant to seagrass (Collier et al., 2016c) because they occur predominantly in the more turbid inshore regions of the reef.

To identify benthic light thresholds for individual seagrass species we ran pairwise models, as above. We ran a model with the full bPAR layer, which was then rerun and the bPAR layer replaced by each of the I_{bPAR} threshold layers.

The outputs of these models (AUC and percent variable importance) were then compared to identify which threshold layer was most informative with each of the five seagrass species. The models including I_{bPAR} as a predictor variable are referred to I_{bPAR} SDM.

6.3.3 Results and discussion

There is an increase in the probability of species presence with increasing bPAR from 0 to around 9 to 12 mol photons m^{-2} d^{-1} depending on species (Figure 27). The highest probabilities occur in the range 6 to 12 mol photons m^{-2} d^{-1} for *C. serrulata* and *H. ovalis* and 6 to 10 mol photons m^{-2} d^{-1}. for *H. spinulosa* and *H. uninervis*. The range in bPAR leading to highest probability of *H. decipiens* presence was lower, at 4 to 9 mol photons m^{-2} d^{-1}. The probability of species presence declines as bPAR increases above these ranges, and the confidence intervals in the predictions become larger (more uncertain) (Figure 27). This is likely related to light becoming saturated and surplus to requirements, and therefore small changes no longer influencing species presence. Higher bPAR levels occur in the mid and outer reef which is not optimal habitat for seagrasses due to other limiting factors. For this reason, we explored I_{bPAR}, as, above a given threshold, the index no longer increases which potentially avoids high levels masking the response of seagrass species to lower benthic light that influences their natural range.

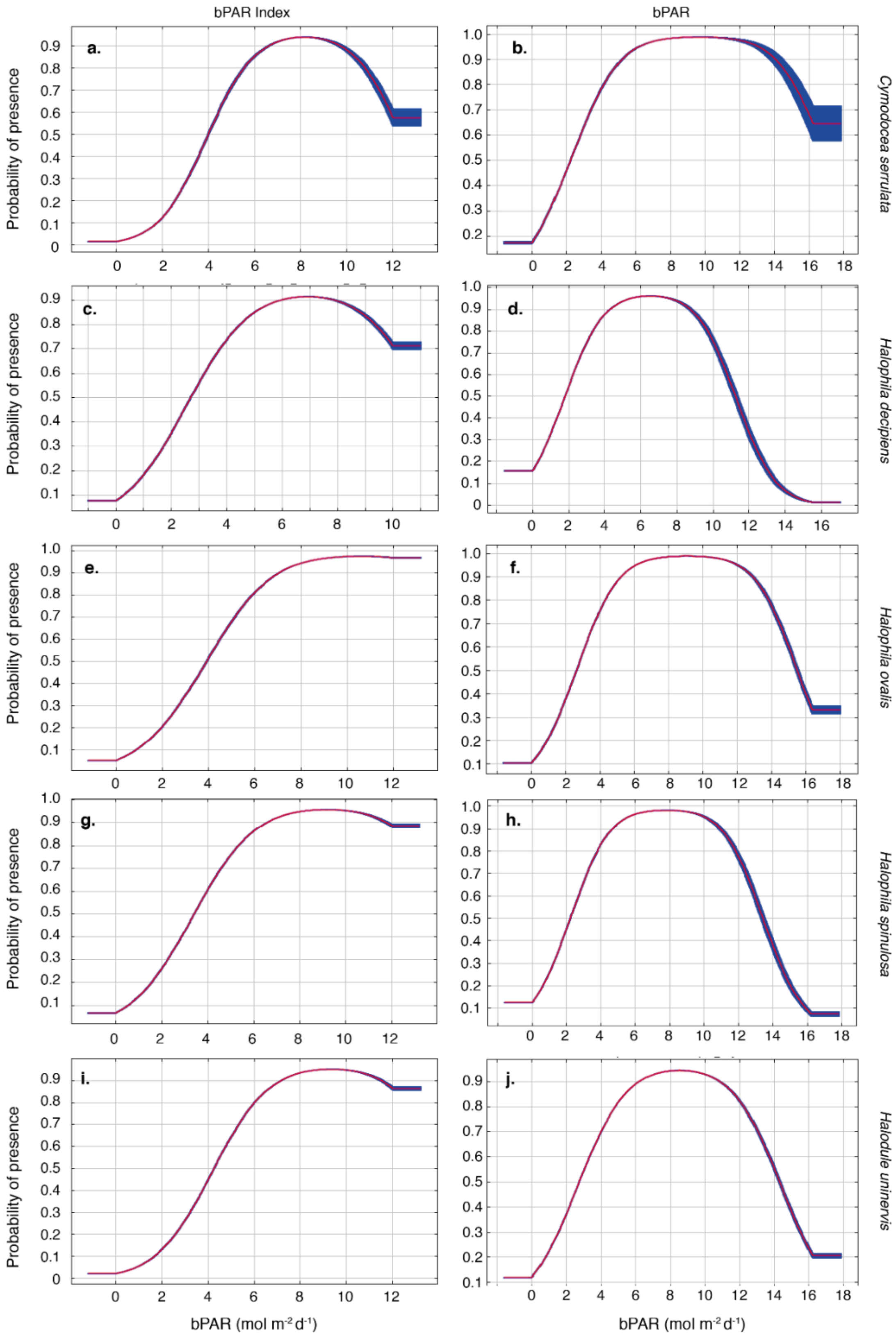

Figure 27: Response of seagrass species presence/absence in MaxEnt species distribution models showing response to the IbPAR with the highest percent contribution to the models which is I_{bPAR} 12 for all species except *H. decipiens* in which it was 10 (Table 1) on the left and to bPAR on the right. Response curves shown for *C. serrulata* (a & b), *H. decipiens* (c & d), *H. ovalis* (e & f), *H. spinulosa* (g & h), and *H. uninervis* (I & j).

The AUC values for the bPAR SDMs were >0.9 (Table 1), indicating a high level of predictive performance (Phillips and Dudik 2008). The predictive performance of models for *C. serrulata*, *H. decipiens* and *H. spinulosa* were largely unchanged, when bPAR was replaced with I_{bPAR}. For the *H. ovalis* and *H. uninervis* models, the model performance improved with I_{bPAR} at some threshold levels but reduced at other threshold levels, with the AUC ranging from 0.65 to 0.99 for those two species.

Table 9: Results of MaxEnt species distribution models including bPAR (mol m^{-2} d^{-1}) or I_{bPAR} thresholds in increments of 2 ranging from 2 to 12 mol photons m^{-2} d^{-1}. Area under the curve (AUC), and percent contribution of bPAR or I_{bPAR} to the models is shown. Bold type indicates highest percent contribution.

Species	Threshold	AUC	% contribution	Species	Threshold	AUC	% contribution
	bPAR	0.98	3.30	*Halophila spinulosa*	bPAR	0.91	5.92
Cymodocea serrulata	I_{bPAR}2	0.98	1.93		I_{bPAR} 2	0.92	2.22
	I_{bPAR} 4	0.96	5.94		I_{bPAR} 4	0.91	7.78
	I_{bPAR} 6	0.98	4.24		I_{bPAR} 6	0.91	11.34
	I_{bPAR} 8	0.97	3.03		I_{bPAR} 8	0.91	13.56
	I_{bPAR} 10	0.97	5.92		I_{bPAR} 10	0.91	12.75
	I_{bPAR} 12	0.97	**6.24**		I_{bPAR} 12	0.91	**14.02**
	bPAR	0.90	2.35	*Halodule uninervis*	bPAR	0.90	0.19
Halophila decipiens	I_{bPAR} 2	0.90	3.20		I_{bPAR} 2	0.99	1.36
	I_{bPAR} 4	0.90	3.78		I_{bPAR} 4	0.97	2.06
	I_{bPAR} 6	0.90	4.47		I_{bPAR} 6	0.99	1.61
	I_{bPAR} 8	0.89	6.15		I_{bPAR} 8	0.99	2.17
	I_{bPAR} 10	0.90	**6.99**		I_{bPAR} 10	0.99	1.31
	I_{bPAR} 12	0.90	4.18		I_{bPAR} 12	0.79	**8.08**
	bPAR	0.94	2.54				
Halophila ovalis	I_{bPAR} 2	0.92	3.17				
	I_{bPAR} 4	0.93	2.06				
	I_{bPAR} 6	0.93	1.67				
	I_{bPAR} 8	0.65	8.13				
	I_{bPAR} 10	0.91	2.77				
	I_{bPAR} 12	0.93	**8.85**				

For the SDMs based on bPAR, the % contribution of bPAR to each model ranged from 0.19 to 5.20%. When depth was not included in the SDMs, the % contribution from bPAR was much higher, but the overall model performance for predicting species distributions was considerably lower (i.e. lower AUC, data not shown) (Carter et al., in prep.), hence those results are not shown here.

For all species, the predictive power of the models increased when the models used I_{bPAR} for at least one threshold +compared to using bPAR. The maximum contribution of I_{bPAR} to the prediction ranged from 6.24 to 14.02%. The maximum percentage contribution was associated with a threshold of 12 mol photons m^{-2} d^{-1} for all species except *H. decipiens*, in which it was 10 mol photons m^{-2} d^{-1} (Table 1). For all species, there were other I_{bPAR} thresholds that were within one percentage of the maximum, indicating that other nearby thresholds generally ranging from 8 to 12 mol photons m^{-2} d^{-1}, would also be acceptable. The exception to this was for *H. uninervis* in which the percentage contribution from I_{bPAR} 12 was considerably higher than any other I_{bPAR} or bPAR. In the *C. serrulata* models, I_{bPAR} 4 and I_{bPAR} 12 produced similar results. *C. serrulata* can occur in shallow and very turbid coastal waters where there may be low bPAR as detected through I_{bPAR} 4 model, but we are not as interested in these lower values for this work as I_{bPAR} 4 would not allow us to explore how changes in bPAR affect habitat suitability over the majority of the range for the species.

It is important to note that these models are based on average long-term conditions at the sites where the species occur. The spatial data set underpinning the SDMs (Carter et al., submitted) is a 35-year composite data set and many areas of the reef, especially the expansive reef subtidal habitats where *Halophila* spp. dominate (Carter et al., in prep.), have only been surveyed once, and more than 15 years ago. Further investigation is required into the sensitivity of seagrass habitat suitability, as well as other indicators of seagrass health such as biomass or percentage cover, to temporal changes in I_{bPAR}. It is also important to note that bPAR modelled from remotely-sensed data is not necessarily equivalent to PAR measured by *in situ* loggers within seagrass meadows, which have been used to establish acute light thresholds (Collier et al., 2016a). There are a number of reasons for this, including the pixel size of bPAR (1 km) which spans a range of depths, tidal exposure in intertidal seagrass habitats, that influences benthic light on scales much smaller than the 1 km pixel and the temporal resolution of the data sets used in this analysis (long-term average dry season bPAR, and 35 years seagrass composite underpinning the SDMs) compared to the short-term light thresholds previously described.

6.3.4 Conclusions

The probability of seagrasses occurring declined above a mean seasonal bPAR ranging from 9 to 12 mol photons m^{-2} d^{-1}. This is not because the light levels become too high for survival, but rather the higher light levels occur where other conditions limit growth for most seagrasses in the mid and outer reef. Therefore, we tested the SDMs with I_{bPAR}, which is calculated using bPAR capped at a defined threshold. We found that I_{bPAR} increased the contribution of benthic light to each species model compared with models using bPAR as a predictor variable. I_{bPAR} using a threshold of 12 mol photons m^{-2} d^{-1} provided the strongest predictions for four seagrass species, while I_{bPAR} using a threshold of 10 had the strongest result for *H. decipiens*.

In conclusion, benthic light is a useful predictor of seagrass habitat suitability and light stress ($I_{bPAR'}$ calculated using a capped daily bPAR) has more predictive power than temporally avaeraged raw daily bPAR.

6.4 Coral Community Health

The work described in Section 6.4 was prepared as an additional, uncontracted, product of the present project (NESP TWQ 5.3) in collaboration with the GBR Marine Monitoring Program. It is being prepared for submission to a peer-reviewed international journal. It can be cited as:

> Robson, B. J., Fabricius, K., Canto, M. M., & Thompson, A. (in prep.). A new light stress index is an effective predictor of coral reef resilience in the Great Barrier Reef.

Figure 28: Year to year changes in coral community health are influenced by variations in water clarity. Credit: Grace Frank.

6.4.1 Introduction

Coral communities are subject to a broad range of disturbances and chronic stressors. In the Great Barrier Reef (GBR), it has been estimated that coral cover declined by more than 50% between 1985 and 2012 as a result of the interacting effects of tropical cyclones, crown of thorns starfish outbreaks and marine heatwaves (De'ath et al., 2012). In the years since then, some recovery but also further massive declines in coral cover and restructuring of reef and associated communities have been observed, mainly attributable to marine heatwaves of increasing severity and frequency (Hughes et al., 2019; Stuart-Smith et al., 2018). Similar events have been observed in other coral reef systems around the world over the same period, with flow-on implications for fish and invertebrate communities (Eakin et al., 2019).

Climate change from global greenhouse gas emissions has been acknowledged by the Great Barrier Reef Marine Park Authority as the greatest threat to the GBR and its World Heritage values (Great Barrier Reef Marine Park Authority, 2019). To date, efforts have therefore been intensified to at least better manage local and regional efforts, in order to minimise other drivers of change, particularly crown of thorns starfish outbreaks (Babcock et al., 2020; Bostrom-Einarsson and Rivera-Posada, 2016; Plaganyi et al., 2020; Pratchett and Cumming, 2019) and sediment and nutrient pollution from catchment runoff (Bartley et al., 2018; Brodie and Pearson, 2016; Fraser et al., 2017; Nachimuthu et al., 2017; Star et al., 2018). This is underpinned by the well-supported expectation that reducing the multiple interacting impacts of various pressures will reduce their cumulative impacts on the health of GBR Ecosystems, improve overall outcomes, and improve the resilience of the system to climate change impacts

(Great Barrier Reef Marine Park Authority, 2018; MacNeil et al., 2019; Mellin et al., 2019; Ortiz et al., 2018; Wolff et al., 2018).

Efforts to reduce local and regional pressures are not without cost to agriculture and other industries. This has driven political controversy (Foxwell-Norton and Konkes, 2019; Foxwell-Norton and Lester, 2017; Tan and Humphries, 2018), calls for improved methods of monitoring GBR water quality and reef health (Hedge et al., 2017), and popular calls for even stronger empirical evidence of the impacts of climate change and water quality on ecosystem outcomes in the Great Barrier Reef.

In response to these calls, Thompson et al. (2020) recently presented a new index to simplify reporting of coral community condition and monitoring of coral community health. This "coral index" combines a range of directly-observed indicators of coral community health and resilience, which consists of (i) coral cover, (ii) change in coral cover from one monitoring observation to the next, (iii) the density of juvenile corals, (iv) reef macroalgal cover and (v) reef community composition. The rationale and observational methods for each of these indicators, as well as the method for combining them into a single index, are described and discussed in detail in Thompson et al. (2020). They show that the coral index is sensitive to both acute pressures from cyclones and storms, bleaching events, crown of thorns outbreaks and the direct influence of flood plumes and chronic pressures associated with reduced water quality as indicated by elevated chlorophyll *a*.

In Chapter 4 we developed a new index for water quality based on remote sensing benthic photosynthetically available radiation (the I_{bPAR} index). This approach uses satellite ocean colour observations to calculate daily integrated bPAR (Magno-Canto et al., 2019; Magno-Canto et al., 2020a) and uses this data product to estimate the seasonal and annual chronic "light stress" for each nominal 1 km^2 pixel across the whole Great Barrier Reef World Heritage Area. In this sense, light stress indicates the reduction in PAR below the locally and seasonally optimal values, due to reduced water clarity associated with dissolved and particulate materials such as suspended sediments and chlorophyll. Whereas the raw bPAR data product tells us how much light is reaching benthic habitats across the GBR, the light stress indicator I_{bPAR} tells us by how much potential photosynthesis in benthic habitats may be reduced by variations in water quality. This light stress indicator is spatially averaged for each Natural Resource Management (NRM) Region and waterbody in the GBR. The I_{bPAR} index ranges from a value of 0 (indicating no light reaching the bottom throughout the reporting period) to 1 (indicating optimal conditions throughout the reporting period), and hence can be used to track changes from year to year.

6.4.2 Methods

GBR Marine Monitoring Program and inshore data from the AIMS Long Term Monitoring Program data were combined and used to calculate the coral index for each of 42 reefs in the GBR for all available observations between 2005 and 2020 following the methods described by Thompson et al. (2020). From this, we calculated the biennial change in the coral index for each reef (reefs are typically monitored once every 2 years). The location of the GBR and of reefs included in the study are shown in Figure 29. Each reef was located within one of four NRM regions (Wet Tropics, Dry Tropics, Mackay Whitsunday or Fitzroy) and one of two waterbodies (Open Coastal or Midshelf), the boundaries of which are also shown. These two water bodies have previously been found to have pronounced intra- and inter-annual changes in water clarity that are strongly associated with river runoff (Fabricius et al. 2016).

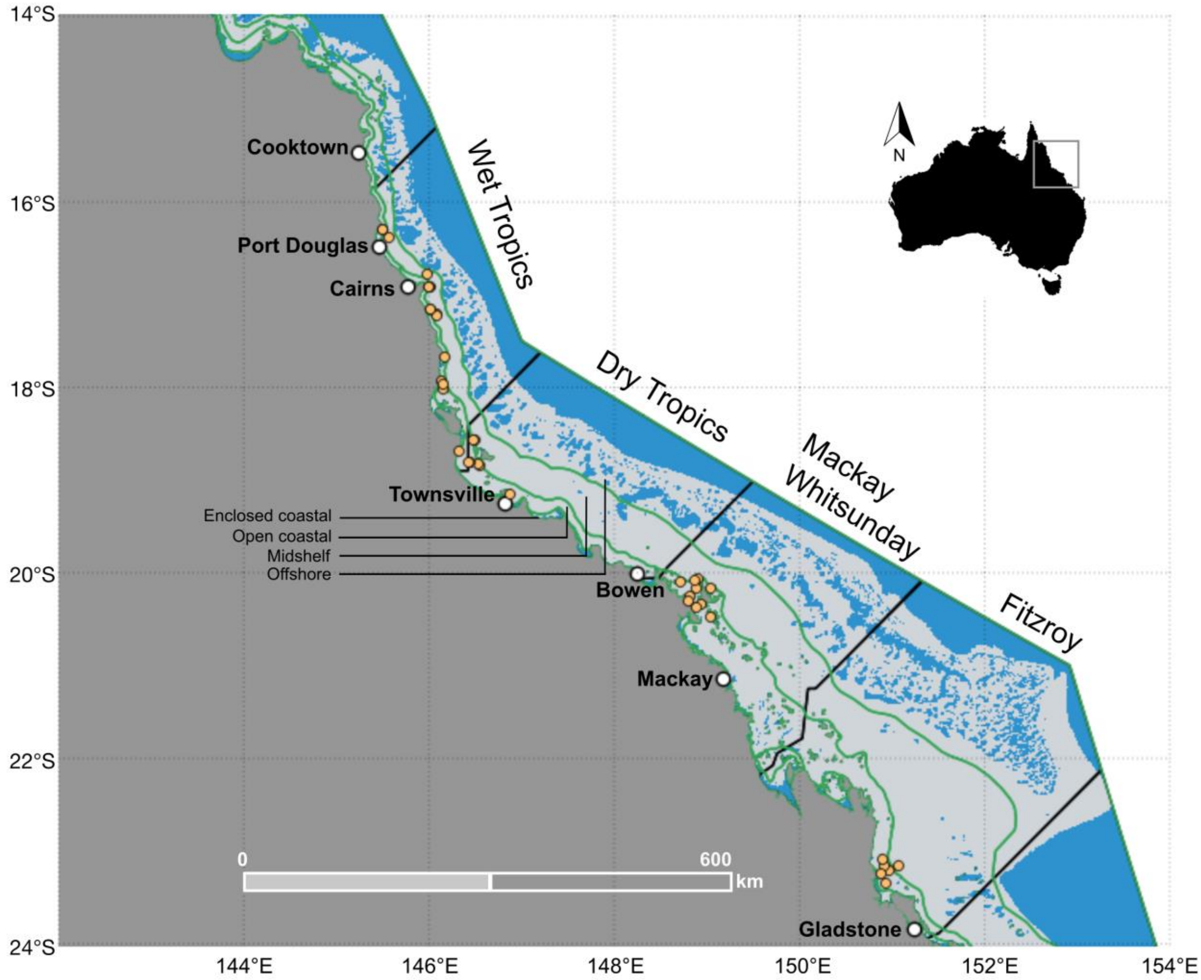

Figure 29: Map of the Great Barrier Reef showing the reef matrix, boundaries of the six NRM regions (black: N to S: Cape York, Wet Tropics, Dry Tropics, Mackay Whitsunday, Fitzroy, and Burnett Mary), and the four cross-shelf water bodies used in the analysis (green: Enclosed coastal, Open coastal, Midshelf and Offshore). Also indicated are the reef locations used in the analysis (orange circles), and several major cities (filled white circles).

Daily remote sensing bPAR data, available from the eAtlas data repository (https://eatlas.org.au/data/uuid/356e7b3c-1508-432e-9d85-263ec8a67cef), were used to calculate annual mean daily photosynthetically-active radiation (PAR) 8 m below the surface ("hereafter, "raw PAR") using the algorithm described in Chapter 2.0. Annual mean chlorophyll *a* and non-algal particulate (NAP) concentrations were estimated from MODIS-Aqua satellite ocean colour data using the algorithm of Brando et al. (2012). For chlorophyll *a*, NAP and raw PAR, data were based on the averages of valid pixels from a square of nine 1 km^2 pixels located as close as possible to each reef but far enough to not be contaminated by shallow benthos.

The daily remote sensing bPAR data were used to calculate light stress and an annual I_{bPAR} index value for each GBR pixel for each year between 2003 and 2019 following the method described in Chapter 4.0. These values were averaged for each NRM region and waterbody for each reporting interval (i.e. all reefs within a given NRM region/waterbody combination were assigned the same I_{bPAR} index value for each year). This was done to allow examining the utility of the regional NRM I_{bPAR} index as a reporting metric relevant to reef health.

Total annual river discharges from catchments adjacent to each region were also calculated as described by Thompson et al. (2020).

Finally, each reef was assigned its local environmental data. To do so, we averaged chlorophyll *a*, raw PAR, NAP, annual (water year) I_{bPAR} index and river discharge values over each of the 2-year intervals between successive reef observations at each reef MMP or LTMP monitoring site to estimate average conditions over the period associated with each calculated change in coral index.

Again following Thompson et al. (2020), reef data for each two-year block were filtered to exclude reefs affected by known acute disturbances; specifically major storms and cyclones, crown of thorns starfish outbreaks, bleaching due to marine heatwaves, and direct exposure to low-salinity river plumes. This allowed us to assess the impacts of chronic pressure associated with water quality indicators (rather than from an acute disturbance).

Using data from all reefs across all years (a total of 517 transitions observed at 41 reefs over 11 two-year intervals – in some cases, at multiple sites within a reef), a random forest model limited to 5 nodes was constructed using the 'randomForest' package (Liaw and Wiener, 2002) in R (R Core Team, 2019a) to predict the change in coral index as a function of 2-year mean chlorophyll *a*, NAP, I_{bPAR} index, depth of observation (2 m or 5 m below lowest tide), total river discharge and NRM region as a categorical variable.

In addition, separate 3-knot generalised additive models (GAMS; Wood, 2011) were calculated to predict the change in coral index within each NRM region and waterbody combination as a function of each of 2-year mean values of chlorophyll *a*, NAP, raw PAR, and I_{bPAR} index.

6.4.3 Results and Discussion

Figure 30 shows the variable importance plots produced by the random forest model. I_{bPAR} index is clearly the single best predictor of change in coral index amongst all those included in the model, followed by river discharge, and chlorophyll *a* and/or NAP. Raw PAR at 8 m had some predictive value, but less than the I_{bPAR} index product. While raw PAR depends largely on geographic location, the bPAR index captures the year-to-year variation in benthic light caused by sub-optimal water quality (Canto et al., submitted).

Simplifying the random forest model to omit all covariates except I_{bPAR} reduces model performance only slightly, with MSE of residuals remaining at 0.0039 and the percentage of variance explained falling from 14% to 13%. This suggests that other covariates (river discharge, NAP, chlorophyll *a*, raw PAR, NRM region and depth) add little additional information that is not already captured by the I_{bPAR}; other variation in the coral index remained unexplained.

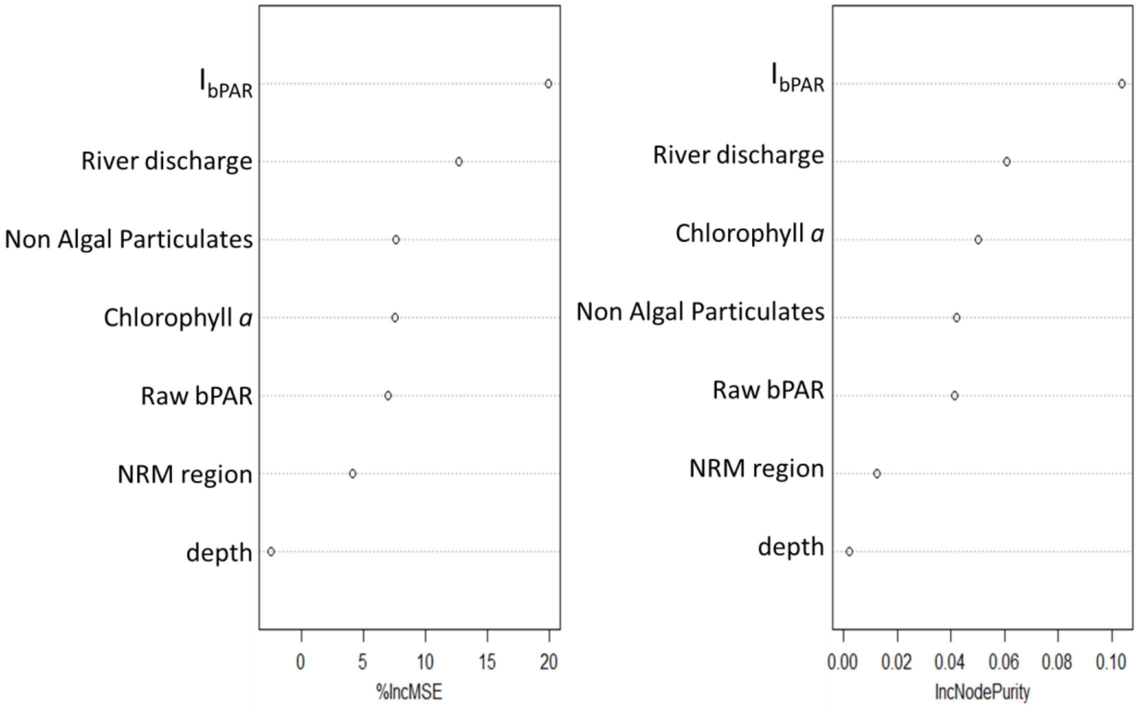

Figure 30: The relative importance of variables included in the random forest model in predicting the temporal change in the value of the coral index. Left: The percent increase in mean square error in the model predictions of coral index if a variable is omitted from the random forest. Right: The mean decrease in node purity in the random forest if a variable is omitted. Both figures show that the *I_{bPAR}* index is a more important predictor of changes in the coral index than any of the other variables considered. The coral index has been designed to be independent of depth.

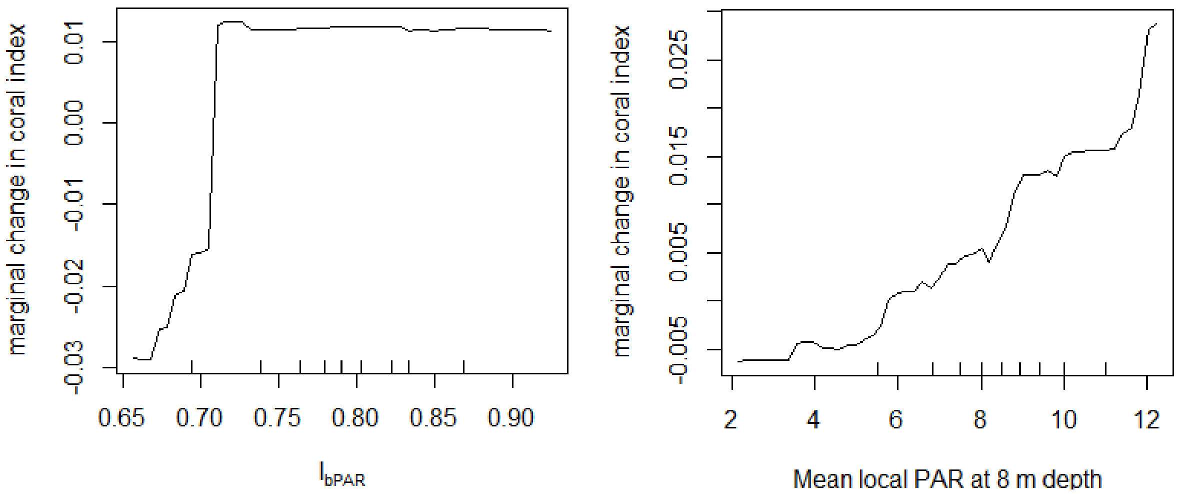

Figure 31: Partial dependence of change in coral index on the annual *I_{bPAR}* index (left) and local mean annual PAR (“raw PAR”) at a depth of 8 m (right) across all NRM Regions and Water Bodies from the random forest model. While PAR depends on depth and geographic location, *I_{bPAR}* captures the reduction in PAR caused by regionally and temporally sub-optimal water clarity. There is little additional effect of improvements in water clarity above a *I_{bPAR}* index value of approximately 0.72.

Fit metrics for all GAMs are presented in Table 10. The GAM informed by *I_{bPAR}* index provides the strongest fit to the observed change in coral index in three out of six regions (namely: the

Open Coastal Wet Tropics and Fitzroy regions, and in the Midshelf Dry Tropics region). In the other three regions, variation in the coral index remained only weakly or largely unexplained by all predictors included ($r^2 \leq 0.13$). The second strongest predictor was River discharge, but I_{bPAR} index out-performed River discharge in two of the three regions. Raw PAR, NAP and chlorophyll were only weakly associated with coral index in all regions ($r^2 \leq 0.20$).

Table 10: Fit statistics r^2 and % deviance explained ("% dev.") for GAMs fitted to predict change in coral index as a function of the indicated variable within each NRM region/waterbody combination. For each row, the model that explains the highest percentage of deviance after excluding models with very low (<0.1) r^2 is highlighted in bold. The Midshelf Mackay Whitsunday and Fitzroy NRM regions had too few data points to generate significant results (n=18 and n=6 respectively).

		Chlorophyll *a*		NAP		Raw PAR		River discharge		I_{bPAR} index	
		r^2	% dev.	r^2	% dev.	r^2	% dev.	r^2	% dev.	r^2	% dev.
Open Coastal	Wet Tropics (n=142)	0.01	2.5%	0.01	2.8%	0.03	3.8%	0.16	18%	**0.23**	**25%**
Open Coastal	Dry Tropics (n=69)	0.01	3.9%	0.01	3.8%	0.04	6.1%	0.01	3.4%	0.02	5.4%
Open Coastal	Mackay Whitsunday (n=108)	-0.01	0.3%	**0.13**	**15%**	-0.01	0.0%	-0.01	0.5%	-0.01	1.1%
Open Coastal	Fitzroy (n=70)	0.25	27%	0.05	6.9%	0.12	15%	0.33	35%	**0.41**	**43%**
Midshelf	Wet Tropics (n=66)	-0.03	0.0%	-0.01	1.3%	**0.12**	**16%**	0.05	7.3%	0.0	2.9%
Midshelf	Dry Tropics (n=38)	0.20	25%	0.16	21%	0.18	21%	**0.34**	**37%**	**0.34**	**37%**

Figure 32 and Figure 33 show in more detail the fitted models for the I_{bPAR} index and the best model other than bPAR, respectively. In the Open Coastal regions, the change in coral index increases from a negative value (indicating a decline in coral community resilience indicators such as coral cover and number of juveniles) to a positive value (indicating an improvement in coral community resilience between successive observations) for increases in I_{bPAR} index up to a value of around 0.8 in two of the regions, with no further improvement above this value. In two of the remaining regions the I_{bPAR} index did not drop below 0.73.

Figure 33 shows that change in coral index as a function of the best water quality indicator for each region excluding the bPAR index.

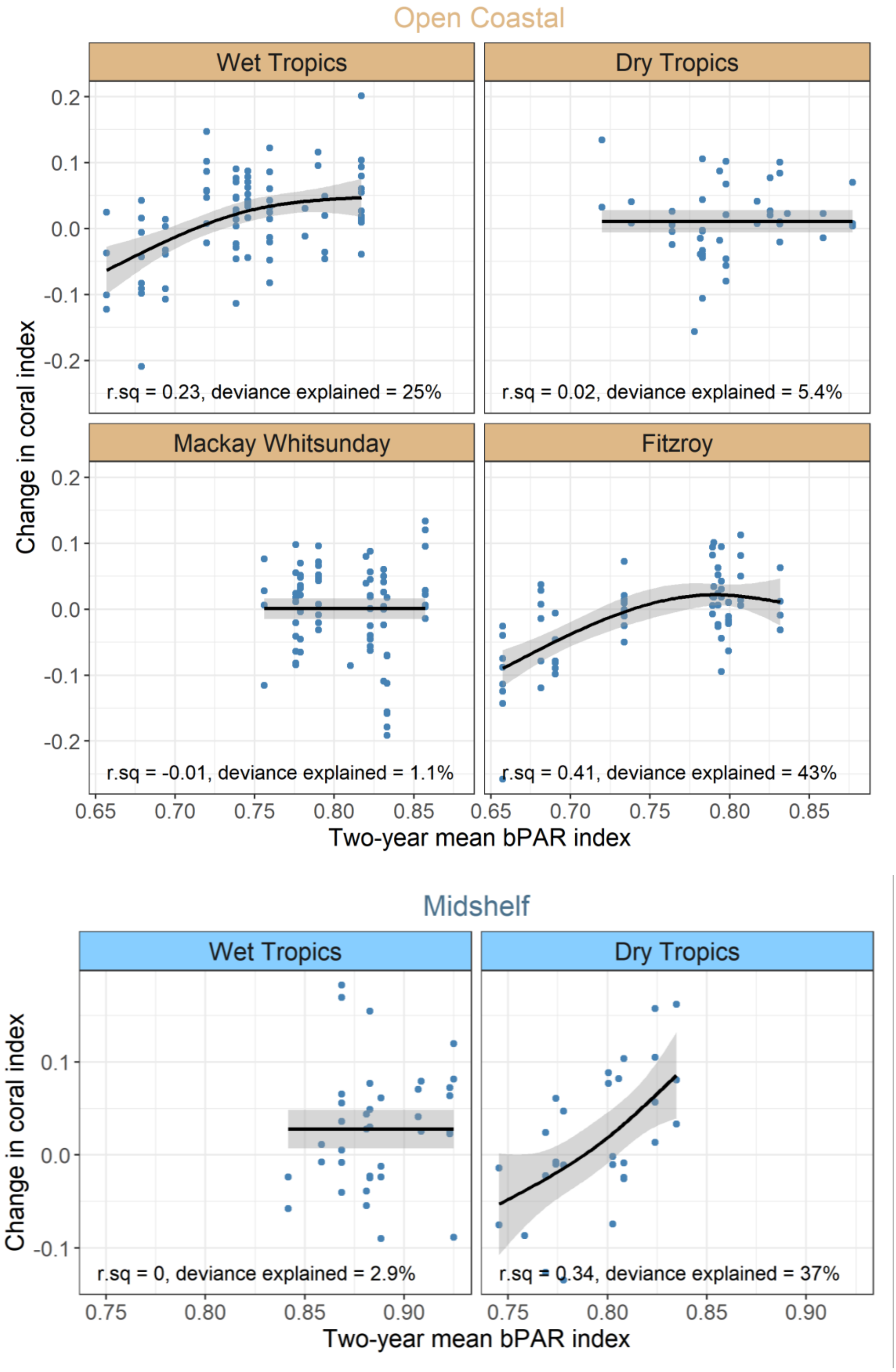

Figure 32: Change in coral index between successive two-yearly GBR Marine Monitoring Program and LTMP observations as a function of the new I_{bPAR} index. Grey shading indicates the 95th percentile confidence interval, the black line indicates the fitted GAM and blue dots are data points for individual reefs for all years.

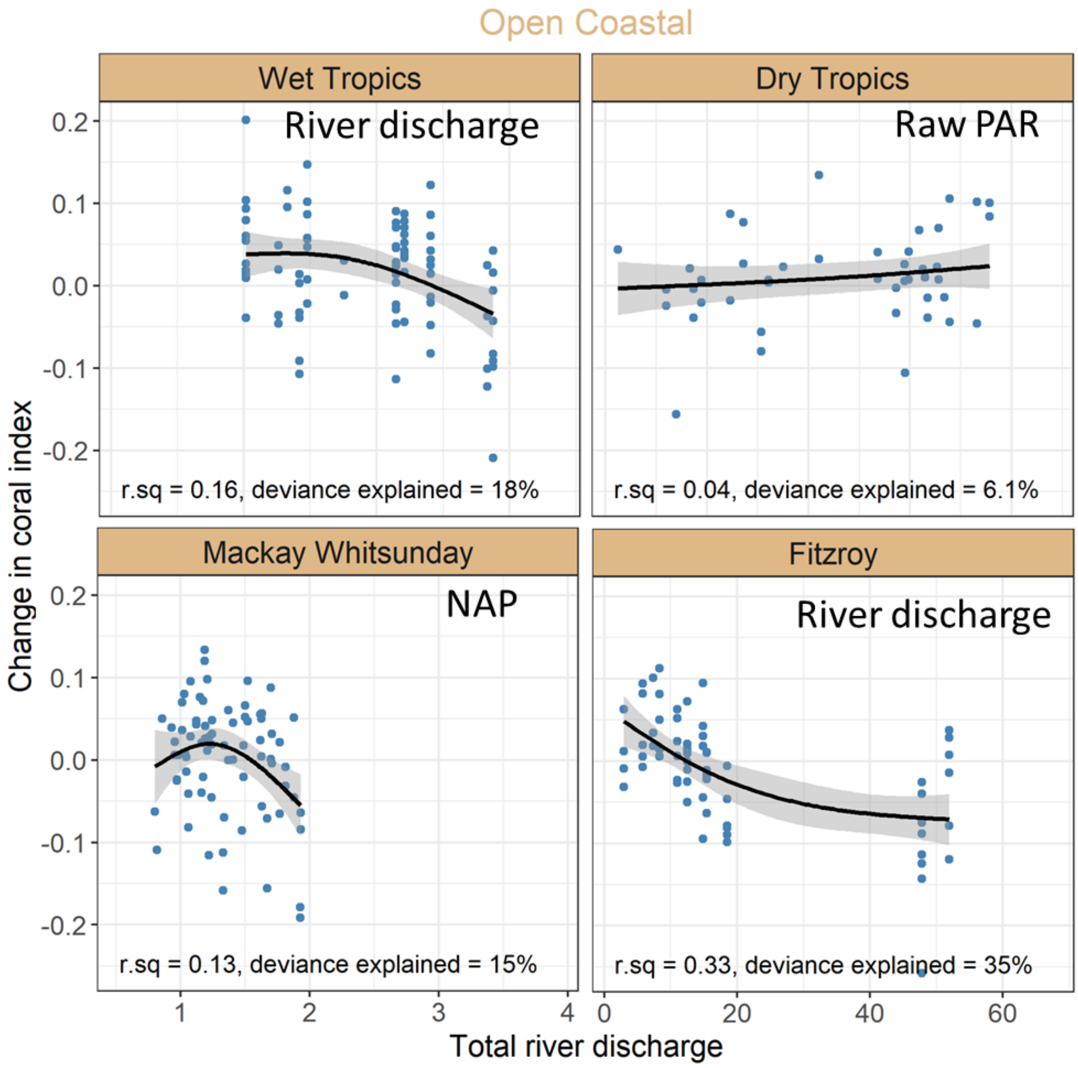

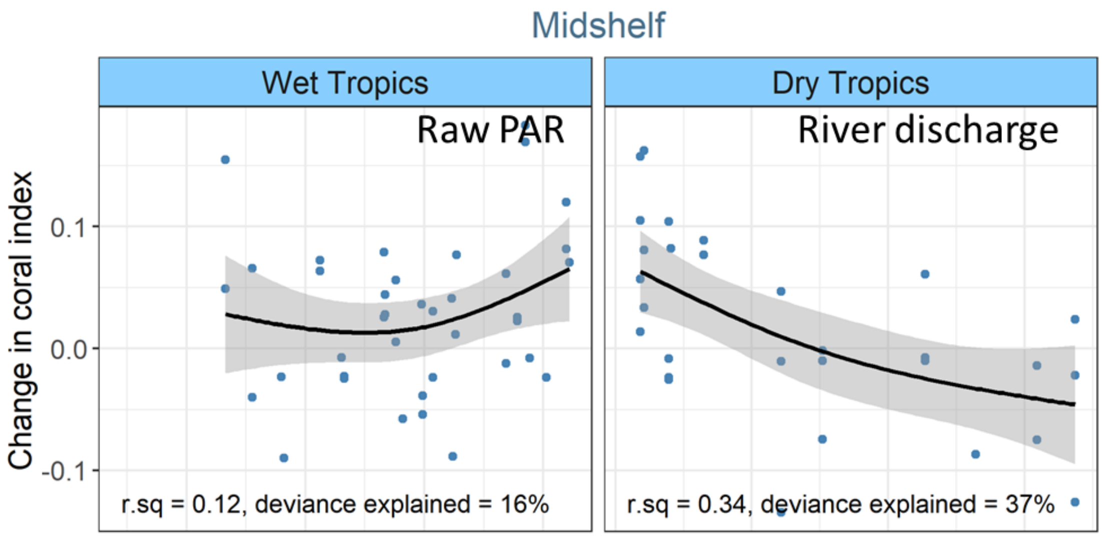

Figure 33: Change in coral index between successive two-yearly GBR Marine Monitoring Program and LTMP observations as a function of the water quality indicator other than bPAR that provides the best fit. In some cases, the heteroscedascity of the data indicates that these alternative models should not be trusted. Left: Open Coastal waters. Right: Midshelf. Grey shading indicates the 95th percentile confidence interval, the black line indicates the fitted GAM and blue dots are data points for individual reefs for all years.

6.4.4 Conclusion

Our results show that chronic stress due to low light associated with poor water quality is (of those tested here) the single strongest predictor of a decline in coral community resilience due to chronic disturbance (i.e. unrelated to acute disturbance such as a bleaching event, crown of thorns outbreak or storm damage). I_{bPAR} explains some of the variation in coral index in 3 of the 6 regions for which we had sufficient data to build models. In the remaining three regions, none of the water quality indicators considered in our models provided a useful predictive fit.

While it explains only a fraction of the total temporal variability in coral community resilience, the recently proposed bPAR index is thus a better predictor of reef health in the GBR than alternative water quality metrics, including regional river discharge, chlorophyll *a*, NAP, and raw PAR 8m below the surface. I_{bPAR} index can be calculated routinely from satellite observations and is available and ready for incorporation into reef report cards.

7.0 EREEFS MODELS AS AN ALTERNATIVE BPAR DATA SOURCE

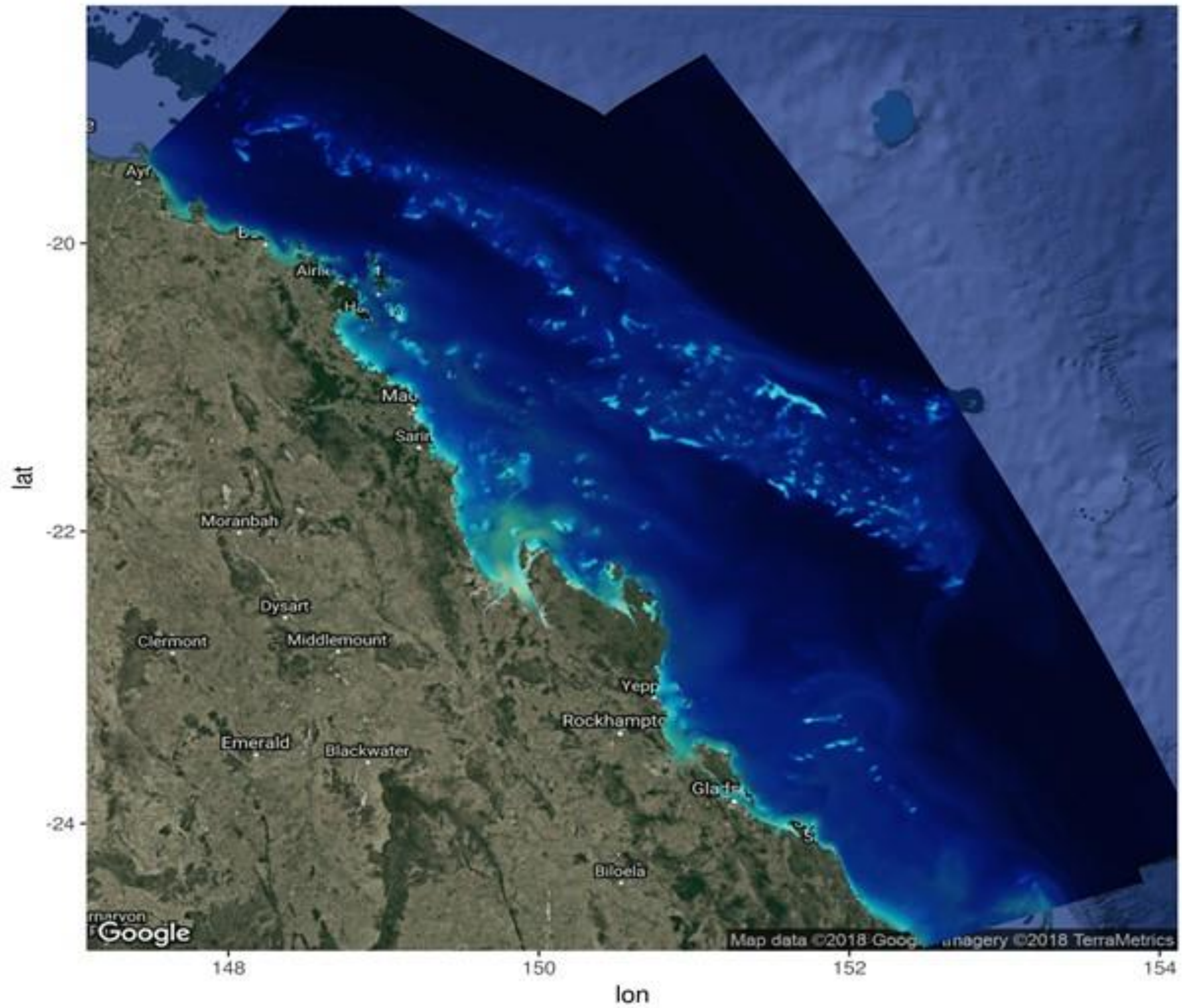

Figure 34: The eReefs marine modelling suite simulates optical conditions and ocean colour in the GBR and is an alternative source of data to calculate the bPAR index.

While remote sensing provides one rich source of bPAR data, satellite data has some limitations. These include:

- The MODIS satellites are near the end of their lifespan (Ladner et al., 2014) and the algorithm has not yet been tested with newer ocean colour satellites, though there is every reason to expect that it will work equally well with data from other satellites.
- Satellites cannot provide observations through clouds, meaning that especially during the wet season and during major storm or monsoon events, many days of data may be missing for large areas of the GBR.
- Remote sensing bPAR calculations assume that water quality in the optical surface layer is vertically uniform, an assumption that benthic PAR calculations in the eReefs model do not share.
- Extrapolating from a single daily satellite overpass to daily integrated values requires the assumption that water quality does not change appreciably during each day. The

impact of this error on the bPAR index calculated over seasonal or annual timescales will be small, as satellite overpass times span a wide range of tidal phases over the course of a season. The eReefs models, however, do not make this assumption and instead integrate PAR from hourly simulated water quality conditions.

- Remote sensing ocean colour-derived water quality observations are known to be unreliable in optically complex nearshore waters, where it is difficult to distinguish among the optical signatures of bottom reflection, suspended sediments, chromatographic dissolved organic material and chlorophyll *a* (Blondeau-Patissier et al., 2009). Although bottom reflectance is accounted for in bPAR data as per McKinna et al. (2015).

In addition, the eReefs models (Baird et al., 2016b; Steven et al., 2019) have the advantage of being the current data source for water quality indicators used in GBR report cards and allow the possibility of testing the impact of scenarios of change (including land management change scenarios) on the value of the water quality index. Indices based on remote sensing data products can only measure current and historical conditions.

For these reasons, it is important to test the suitability of the eReefs biogeochemical model as an alternative data source for calculation of a bPAR index, while noting that the eReefs biogeochemical model also has limitations. These include:

- A limited historical record, with the 4 km^2 resolution eReefs biogeochemical model going back to December 2010 (Skerratt et al., 2019), or the 1 km^2 model since September 2015 (vs April 2002 for MODIS Aqua ocean colour data).
- Known limitations of the models with respect to reproduction of short-term temporal variations in chlorophyll and sediment concentrations (Margvelashvili et al., 2018; Robson et al., 2020).
- Variable trust in models in general (Hunka et al., 2013; Olsson and Andersson, 2006) and these models in particular among key stakeholders and decision makers, despite a high standard of model evaluation (Robson et al., 2020; Skerratt et al., 2019).

For the eReefs biogeochemical model to be a suitable alternative data source, we would need to establish: (1) that the model adequately captures variations in benthic light dose on relevant spatial and temporal scales; and (2) that output from the model can be used to predict changes in ecosystem health.

7.1 Performance of eReefs benthic PAR data products against *in situ* benthic PAR observations at Yongala NRS

The first step in our evaluation of the eReefs models as an alternative data source for the bPAR index was to assess model performance vs *in situ* bPAR measurements at the Yongala National Reference Station (NRS). Comparing instantaneous eReefs simulated PAR with *in situ* measured instantaneous PAR, we find a very weak correlation (Figure 35). A closer examination of the temporal record (Figure 36) and underlying model processes (Baird et al., 2020c; Herzfeld et al., 2016) reveals that this is largely due to a limited representation of cloud cover in the eReefs models: the current models consider only cloud cover in octals, which does not adequately capture local spatial and short-timescale variations in light attenuation due to clouds of varying height and density. Hence, at the Yongala NRS, we see the eReefs models assuming some days to have limited incident light at the surface when, locally, these days were not cloudy, and the reverse on other days (Figure 36). These issues have been discussed with the CSIRO eReefs team and an improved representation of cloud cover is under development.

However, as the bPAR index does not depend on instantaneous bPAR but instead on aggregated bPAR metrics over a seasonal or annual reporting period, the poor match between simulated and observed instantaneous bPAR is not fatal to the prospect of using eReefs-derived bPAR in calculating the bPAR index. More relevant than direct comparisons of daily PAR at an individual site are: a) the relationship between year-to-year variations in a bPAR index derived from eReefs data and variations in the same index calculated from remote sensing data; and more importantly, b) the utility of each version of the bPAR index in predicting changes in coral health.

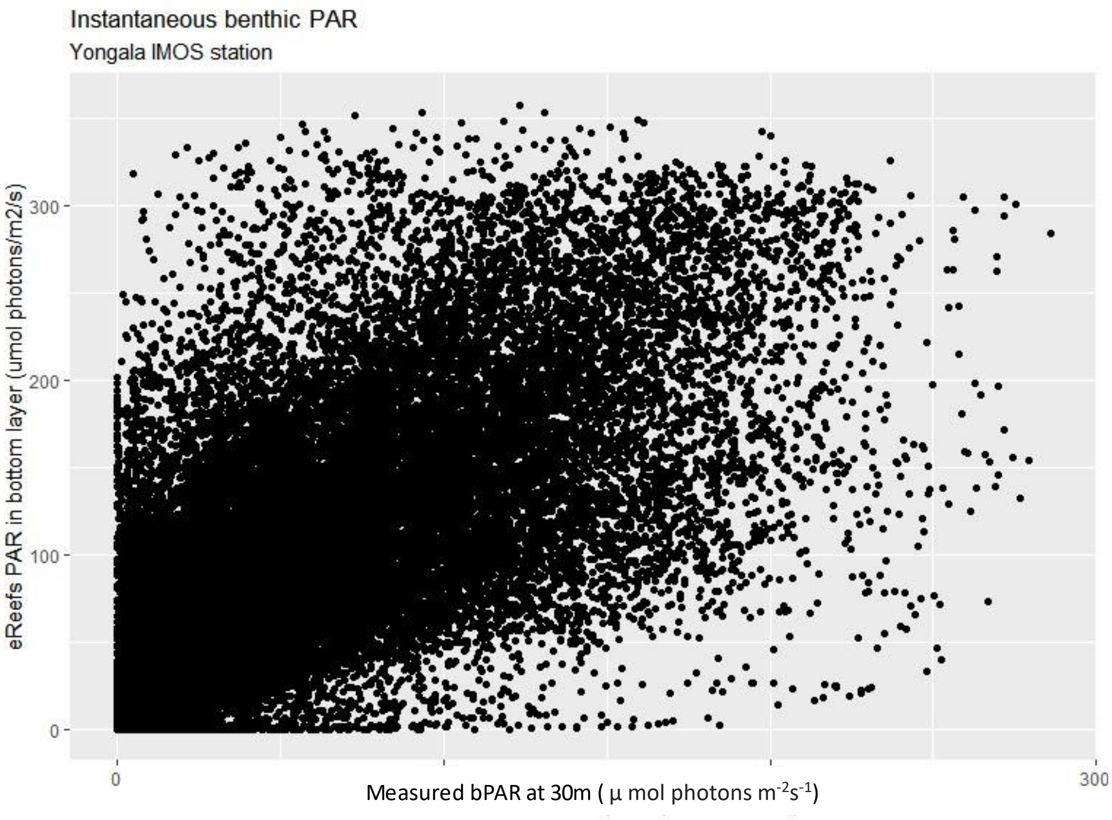

Figure 35: ***In situ*** **measured bPAR at the IMOS Yongala National Reference Station versus eReefs simulated PAR in the bottom layer of the water column.**

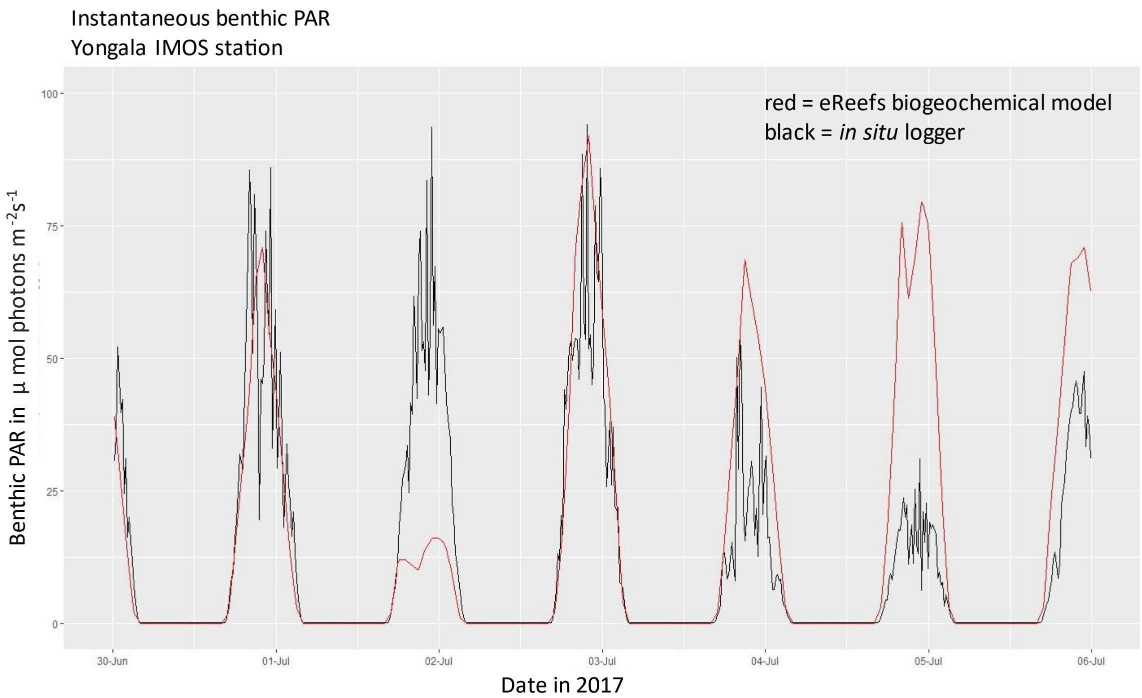

Figure 36: In situ logger PAR at Yongala IMOS station (black) and hourly eReefs simulated Epibenthic PAR over a one-week period in July 2017.

7.2 Comparison of an eReefs-derived bPAR index against the remote sensing bPAR index

Our next step was to calculate a bPAR index using benthic PAR information taken from the 4 km^2-resolution eReefs biogeochemical model (B3p1) (Baird et al., 2020b). While the 1 km^2 model would allow higher-resolution calculation of light stress and is better able to capture the effects of varying bathymetric depth on bPAR, the available 1 km^2 resolution eReefs biogeochemical model covers a shorter historical time-span (beginning in September 2015 vs December 2010 for the 4 km^2-resolution model) and has not been updated to the most recent version of the biogeochemical and optical models.

To calculate a bPAR index using eReefs model output, we applied the same method used in Chapter 2.0, but using the eReefs variable, "EpiPAR_sg" (epibenthic PAR above the seagrass) instead of remote sensing bPAR.

Figure 37 shows that year-to-year variations in eReefs-derived and remote sensing-derived bPAR indices are strongly correlated in every NRM region, except the Burnett-Mary, which may be impacted by the proximity of the model's open boundary and the limited number of optically-shallow model grid cells in this region. In the case of the Offshore Burnett-Mary, there were not sufficient shallow grid cells on a 4 km^2 scale to allow calculation of an index at all. Across all regions, the median correlation between the two versions of the index is 0.71, indicating a strong agreement between the two data sources regarding year-to-year variations in the index. An R of 0.71 indicates that, overall, 49% of the variance is accounted for. Errors in both the eReefs and remote sensing bPAR and the limited resolution of the eReefs data product account for the remainder.

The slope of the regression varies between regions and is not equal to 1.0. In most regions, the eReefs-based index varies across a wider range than the remote sensing bPAR index. This is attributable at least in part to the method used to scale light stress to achieve an index value between 0 and 1, as scaling is performed separately for each index and region. Rescaling the indices to achieve a 1.0 slope or a specified spread amongst A-E grades would be straightforward if desired.

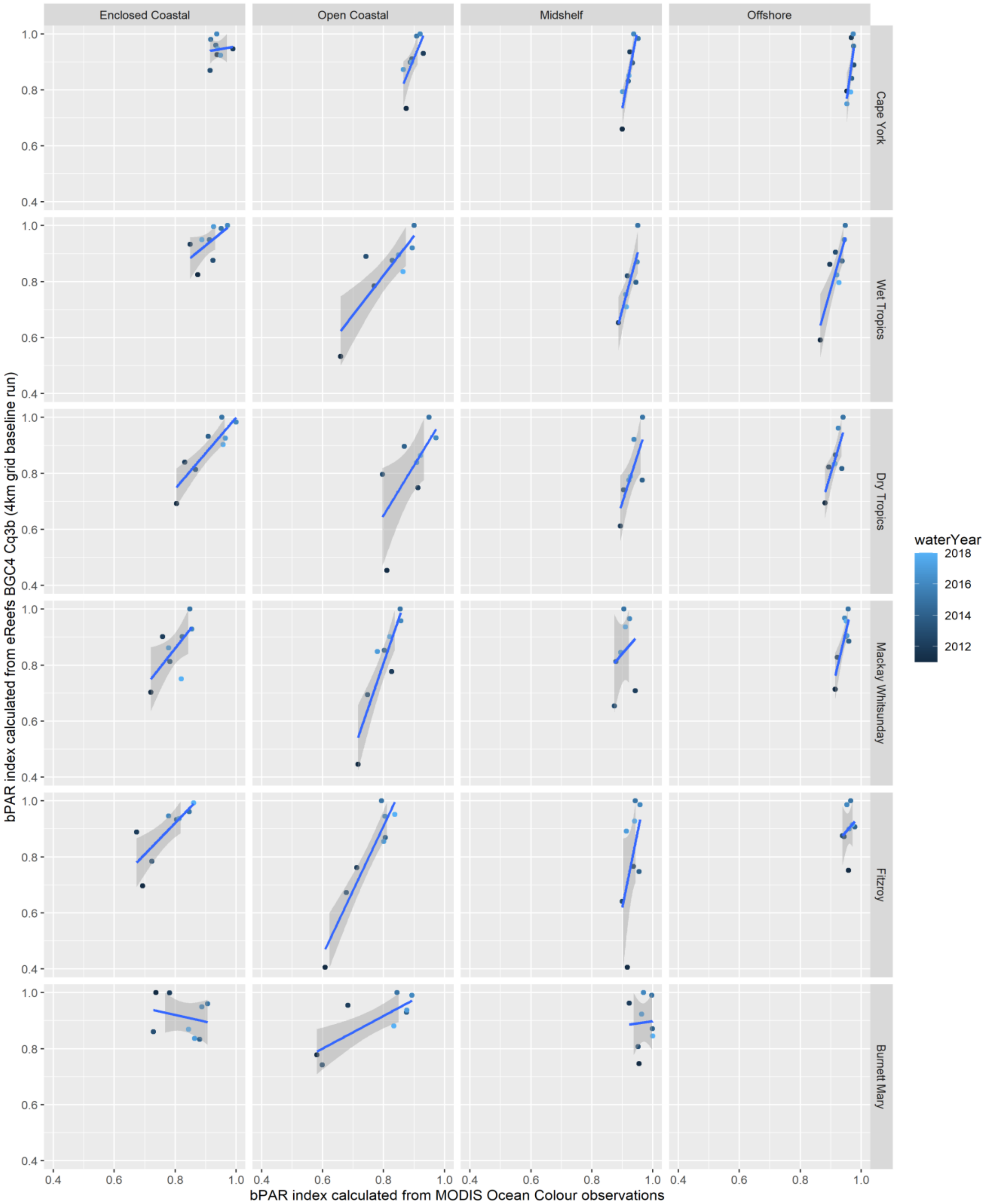

Figure 37: The value of the annual bPAR index calculated from eReefs benthic PAR data (EpiPAR) plotted against value of the annual bPAR index calculate from remote sensing data. Median R across all regions = 0.71

7.3 Utility of the eReefs bPAR index in predicting coral community resilience

A more direct test of the utility of the eReefs-based bPAR index is whether it provides comparable performance as a predictor of coral community resilience. Figure 38 and Figure 39 illustrate generalised additive models for prediction of change in the coral index (Thompson et al., 2020), an index of coral community resilience recently developed through the GBR Marine Monitoring Program. The development and detailed implementation of the model based on remote sensing bPAR was described in Chapter 6 - Ecological validation. The same approach has been applied using eReefs-derived bPAR data to produce the models shown in Figure 38. We see that the eReefs bPAR index and the remote sensing bPAR index are both useful in predicting temporal changes in coral community resilience, and the two versions of the bPAR index have similar predictive performance.

Both the remote sensing and eReefs bPAR indices are better predictors of temporal changes in the coral index than remote sensing chlorophyll *a*, non-algal particulates, raw remote sensing PAR or river discharge in the Open Coastal Fitzroy and Wet Tropics and the Midshelf Dry Tropics regions, while variation in coral index in the other regions remained not well predicted by any available variables. The eReefs bPAR index is comparable with the best alternative water quality indicator available.

We can therefore use eReefs simulated bPAR with some confidence as an alternative operational data source for the bPAR index if grade scores are scaled appropriately. We can also use eReefs catchment management scenarios to anticipate changes in coral community health that may arise from changes in catchment management. This has been followed up in a NESP Synthesis case study, and the resulting findings will be reported as part of NESP TWQ Synthesis Project 6.4.

That the eReefs bPAR index and the remote sensing bPAR index produce similar results in open coastal waters, despite making different assumptions regarding the effects of clouds and the vertical distribution of suspended material in the water column, provides an added level of confidence that these assumptions do not have a large effect on the reported year-to-year variations in the index.

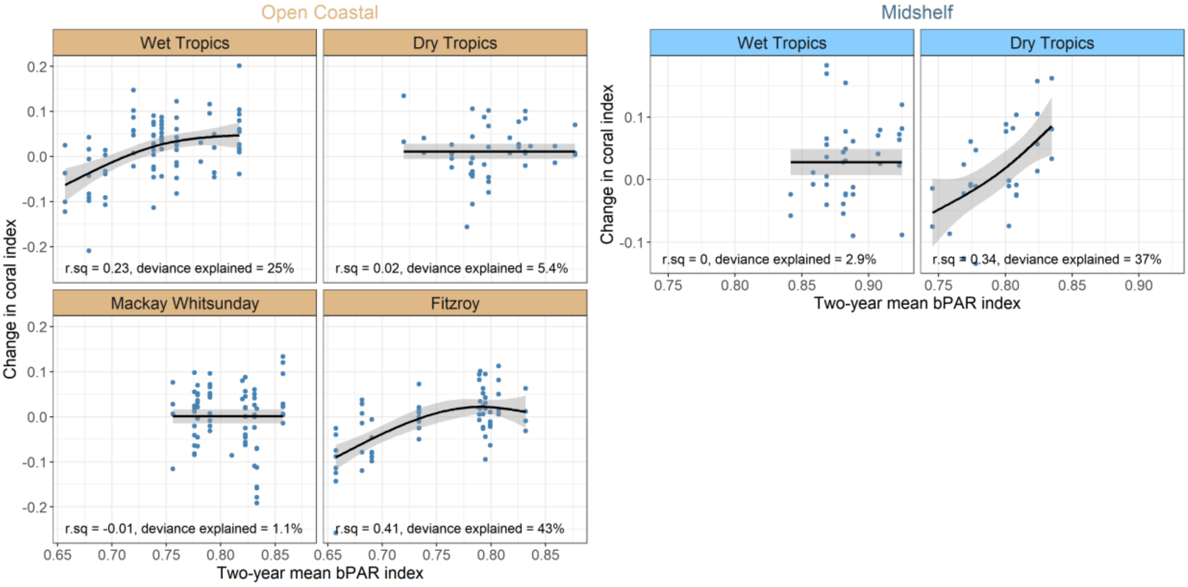

Figure 38: Coral index (an index of coral community resilience) as a function of annual bPAR index calculated from remote sensing bPAR.

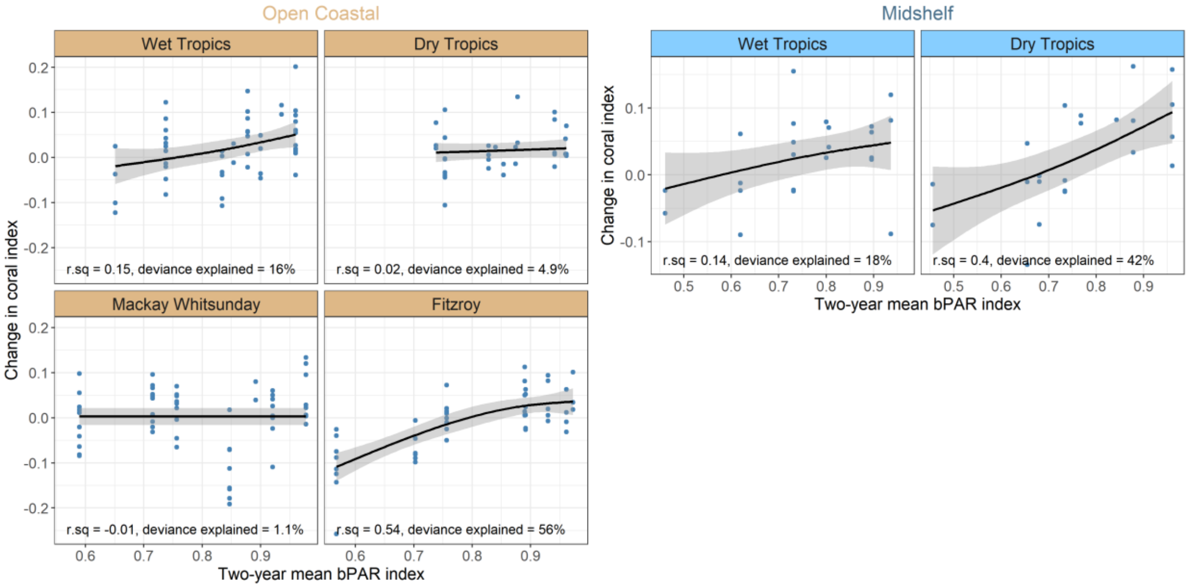

Figure 39: Coral index (an index of coral community resilience) as a function of annual bPAR index calculated from eReefs simulated bPAR (biogeochemical model variable EpiPAR_sg).

8.0 RECOMMENDATIONS AND CONCLUSION

In this project, we have demonstrated that benthic light (bPAR) can be estimated from remote sensing ocean colour observations, and these estimates are accurate at the four (Midshelf) sites for which we have *in situ* PAR data. We then developed a new index of water quality for the GBR that can be based on either remote sensing or eReefs modelled bPAR. The new bPAR index measures the chronic light stress experienced by benthic photosynthesising biota such as seagrasses and corals over the course of a reporting period (i.e. a season or year). We have shown that an aggregated version of the index reported at the level of NRM Region and Water Body is sensitive to year-to-year variations in water quality in nearshore and Midshelf waters, and that these variations can largely be attributed to variations in river discharge and river sediment and nutrient loads. Further, we have demonstrated that the aggregated bPAR index explains some of the temporal variation in in coral community resilience in NRM Regions and Water Bodies impacted by variable water quality.

One of the major limitations of the bPAR data product is its spatial resolution – the current data product is limited to 1 km^2 pixels assumed to have uniform bathymetry, which is not directly relevant to the environmental conditions of corals in the complex reef environment. Priorities for further work include:

1) Development and provision of a tool that will allow users to calculate bPAR at any specified depth and resolution. As a first step towards this, we have provided spectral light attenuation (spectral K_d) as an additional eAtlas data product from this project;
2) Validation of the bPAR data product in turbid nearshore waters;
3) Testing the utility of the light stress index as a predictor of temporal changes in seagrass communities (and finalisation of the work regarding the index of a predictor of changes in coral community resilience);
4) Operationalisation of the bPAR data product using data from newer ocean colour satellites.

We recommend that the bPAR index be further explored as a potential indicator of water quality in the GBR in future Reef Reports. We additionally recommend that as eReefs catchment change and climate change scenarios are conducted, they are also assessed in terms of their potential impacts on bPAR, the bPAR index, and resulting ecological outcomes.

Figure 40: Healthy reef habitats depend on good water quality. Image: Grace Frank.

9.0 CODE AND DATA AVAILABILITY

Data and code developed for this project has been made available through e-Atlas (https://eatlas.org.au/nesp-twq-5/benthic-light-5-3). These datasets include:

1) Daily maps in netCDF format of BR spectral diffuse attenuation coefficient (K_d) of downwelling irradiance (E_d) from ocean colour, 2002-2019 (https://eatlas.org.au/data/uuid/88ae7fc2-0f9a-4453-b929-ffb8273c26e9).

   This dataset contains estimates of diffuse attenuation coefficient (K_d) of downwelling irradiance at different wavelengths (412, 443, 469, 488, 531, 547, 555, 645, 667 and 678 nm) in the Great Barrier Reef Marine Park and Coral Sea for each day from July 2002 through to December 2019. Data are provided on a nominal 1km grid for each wavelength.

   The spectral diffuse attenuation coefficient (K_d) of downwelling irradiance (E_d) determines the amount of light that penetrates the water column and reaches at depth. When this parameter is known along with water depth and estimates of surface irradiance at corresponding spectral wavelength, equivalent benthic irradiance (or the amount of light reaching the seafloor) can be estimated for any location within the GBR. Information on the available light at depth is important since light is a critical requirement to sustain growth and maintain health of benthic ecosystems via photosynthesis. In coastal marine environment, light is a limiting factor that determines the distribution of benthic organisms including seagrasses and corals.

   These data are available through an online visualisation tool, for direct download, or for programmatic access via a THREDDS server.

2) Daily maps in netCDF format of GBR benthic light (bPAR) from ocean colour, 2002-2019. (https://eatlas.org.au/data/uuid/356e7b3c-1508-432e-9d85-263ec8a67cef).

   This dataset contains estimated daily integrated benthic photosynthetically active radiation (bPAR) in the Great Barrier Reef Marine Park and Coral Sea for each day from July 2007 through to December 2019. Data are provided on a 1km grid.

   The amount of light available for photosynthesis (photosynthetically active radiation, or PAR) is an important determinant of ecosystem health. PAR reaching the bottom of the water column is known as benthic PAR (bPAR). Where there is sufficient light reaching the bottom, seagrasses and corals may thrive. bPAR varies seasonally as a function of surface PAR, but also varies function of both water depth and water quality.

   These data are available through an online visualisation tool, for direct download, or for programmatic access via a THREDDS server.

3) Daily maps in netCDF format of GBR PAR at 8 m depth from ocean colour, 2002-2019. (link pending).

This dataset contains estimated daily integrated photosynthetically active radiation (PAR) at a depth of 8 m in the Great Barrier Reef Marine Park and Coral Sea for each day from July 2007 through to December 2019. Data are provided on a 1km grid.

These data will be available through an online visualisation tool, for direct download, or for programmatic access via a THREDDS server.

4) Code used to calculate the bPAR index for water quality described in Chapter 4.0, along with the associated figures (link pending).

5) Annual and seasonal bPAR index values for each NRM region and water body, 2003-2019 (link pending).

6) Code to calculate for spectral K_d and PAR at any depth, as described in Chapter 2.0. This code has been written in C and has also been provided to NASA for incorporation into their SeaDAS software (NASA). NASA have advised us that it will be available as a test algorithm in the next release of SeaDAS, and can be applied to data from any ocean colour satellite.

REFERENCES

Ackleson, S.G., 2003. Light in shallow waters: A brief research review. Limnology and Oceanography 48(1 part 2) 323-328.

Ahmad, Z., Franz, B.A., McClain, C.R., Kwiatkowska, E.J., Werdell, J., Shettle, E.P., Holben, B.N., 2010. New aerosol models for the retrieval of aerosol optical thickness and normalized water-leaving radiances from the SeaWiFS and MODIS sensors over coastal regions and open oceans. Applied Optics 49(29) 5545-5560.

Alvarez-Romero, J.G., Devlin, M., da Silva, E.T., Petus, C., Ban, N.C., Pressey, R.L., Kool, J., Roberts, J.J., Cerdeira-Estrada, S., Wenger, A.S., Brodie, J., 2013. A novel approach to model exposure of coastal-marine ecosystems to riverine flood plumes based on remote sensing techniques. Journal of Environmental Management 119 194-207.

Anthony, K., Ridd, P.V., Orpin, A.R., Larcombe, P., Lough, J., 2004. Temporal variation of light availability in coastal benthic habitats: Effects of clouds, turbidity, and tides. Limnology and Oceanography 49 2201-2211.

Austin, R.W., Petzold, T.J., 1981. The Determination of the Diffuse Attenuation Coefficient of Sea Water Using the Coastal Zone Color Scanner, In: Gower, J.F.R. (Ed.), Oceanography from Space. Springer US: Boston, MA, pp. 239-256.

Babcock, R.C., Plaganyi, E.E., Condie, S.A., Westcott, D.A., Fletcher, C.S., Bonin, M.C., Cameron, D., 2020. Suppressing the next crown-of-thorns outbreak on the Great Barrier Reef. Coral Reefs 39(5) 1233-1244.

Bailey, S.W., Franz, B.A., Werdell, P.J., 2010. Estimation of near-infrared water-leaving reflectance for satellite ocean color data processing. Optics Express 18(7) 7521-7527.

Bailey, S.W., Werdell, P.J., 2006. A multi-sensor approach for the on-orbit validation of ocean color satellite data products. Remote Sensing of Environment 102(1–2) 12-23.

Bainbridge, Z., Lewis, S., Bartley, R., Fabricius, K., Collier, C., Waterhouse, J., Garzon-Garcia, A., Robson, B., Burton, J., Wenger, A., 2018. Fine sediment and particulate organic matter: A review and case study on ridge-to-reef transport, transformations, fates, and impacts on marine ecosystems. Marine pollution bulletin 135 1205-1220.

Baird, M., Wild-Allen, K., Parslow, J., Mongin, M., Robson, B., Skerratt, J., Rizwi, F., Soja-Wozniak, M., Jones, E., Herzfeld, M., 2020a. CSIRO environmental modelling suite (EMS): scientific description of the optical and biogeochemical models (vB3p0). Geoscientific Model Development Article number: 115.

Baird, M.E., Adams, M.P., Andrewartha, J., Herzfeld, M., Jones, E., Margvelashvili, N., Mongin, M., Rizwi, F., Robson, B., Skerratt, J., 2020b. Additional processes and diagnostic variables in the CSIRO Environmental Modelling Suite. CSIRO: Hobart, Australia.

Baird, M.E., Adams, M.P., Babcock, R.C., Oubelkheir, K., Mongin, M., Wild-Allen, K.A., Skerratt, J., Robson, B.J., Petrou, K., Ralph, P.J., O'Brien, K.R., Carter, A.B., Jarvis, J.C., Rasheed, M.A., 2016a. A biophysical representation of seagrass growth for application in a complex shallow-water biogeochemical model. Ecological Modelling 325 13-27.

Baird, M.E., Cherukuru, N., Jones, E., Margvelashvili, N., Mongin, M., Oubelkheir, K., Ralph, P.J., Rizwi, F., Robson, B.J., Schroeder, T., 2016b. Remote-sensing reflectance and true colour produced by a coupled hydrodynamic, optical, sediment, biogeochemical model of the Great Barrier Reef, Australia: comparison with satellite data. Environmental Modelling & Software 78 79-96.

Baird, M.E., Mongin, M., Rizwi, F., Bay, L.K., Cantin, N.E., Soja-Woźniak, M., Skerratt, J., 2018. A mechanistic model of coral bleaching due to temperature-mediated light-driven reactive oxygen build-up in zooxanthellae. Ecological Modelling 386 20-37.

Baird, M.E., Wild-Allen, K.A., Parslow, J., Mongin, M., Robson, B., Skerratt, J., Rizwi, F., Soja-Woźniak, M., Jones, E., Herzfeld, M., 2020c. CSIRO environmental modelling suite (EMS): scientific description of the optical and biogeochemical models (vB3p0). Geoscientific Model Development 13(9) 4503-4553.

Baker, K., Smith, R.C., 1990. Irradiance transmittance through the air/water interface, In: Spinrad, R.W. (Ed.), Ocean Optics X. SPIE, pp. 556-565.

Barnes, B.B., Hu, C., Cannizzaro, J.P., Craig, S.E., Hallock, P., Jones, D.L., Lehrter, J.C., Melo, N., Schaeffer, B.A., Zepp, R., 2014. Estimation of diffuse attenuation of ultraviolet light in optically shallow Florida Keys waters from MODIS measurements. Remote Sensing of Environment 140 519-532.

Barnes, B.B., Hu, C., Schaeffer, B.A., Lee, Z., Palandro, D.A., Lehrter, J.C., 2013. MODIS-derived spatiotemporal water clarity patterns in optically shallow Florida Keys waters: A new approach to remove bottom contamination. Remote Sensing of Environment 134(Supplement C) 377-391.

Bartley, R., Thompson, C., Croke, J., Pietsch, T., Baker, B., Hughes, K., Kinsey-Henderson, A., 2018. Insights into the history and timing of post-European land use disturbance on sedimentation rates in catchments draining to the Great Barrier Reef. Marine pollution bulletin 131 530-546.

Beaman, R., 2010. 3DGBR: A high-resolution depth model for the Great Barrier Reef and Coral Sea. Marine and Tropical Sciences Facility (MTSRF) Project 2.

Beaman, R.J., Bridge, T.C.L., Luter, C., Reitner, J., Worheide, G., 2016. Spatial patterns in the distribution of benthic assemblages across a large depth gradient in the Coral Sea, Australia. Marine Biodiversity 46(4) 795-808.

Bessell-Browne, P., Negri, A.P., Fisher, R., Clode, P.L., Jones, R., 2017. Impacts of light limitation on corals and crustose coralline algae. Scientific Reports 7 11553.

Bishop-Taylor, R., Sagar, S., Lymburner, L., Beaman, R.J., 2019. Between the tides: Modelling the elevation of Australia's exposed intertidal zone at continental scale. Estuarine Coastal and Shelf Science 223 115-128.

Blondeau-Patissier, D., Brando, V.E., Oubelkheir, K., Dekker, A.G., Clementson, L.A., Daniel, P., 2009. Bio-optical variability of the absorption and scattering properties of the Queensland inshore and reef waters, Australia. Journal of Geophysical Research: Oceans 114(C5).

BOM, 2018. Tropical Cyclone Debbie Technical Report: A comprehensive summary of meteorological and hydrological data associated with Severe Tropical Cyclone Debbie that affected Queensland and New South Wales during March and April 2017.

Bostrom-Einarsson, L., Rivera-Posada, J., 2016. Controlling outbreaks of the coral-eating crown-of-thorns starfish using a single injection of common household vinegar. Coral Reefs 35(1) 223-228.

Bradie, J., Leung, B., 2017. A quantitative synthesis of the importance of variables used in MaxEnt species distribution models. Journal of Biogeography 44(6) 1344-1361.

Brando, V.E., Dekker, A.G., Park, Y.J., Schroeder, T., 2012. Adaptive semianalytical inversion of ocean color radiometry in optically complex waters. Applied Optics 51(15) 2808-2833.

Brando, V.E., Schroeder, T., Dekker, A.G., Clementson, L., 2013. Reef Rescue Marine Monitoring Program: Using remote sensing for GBR-wide water quality. Final report for 2011/12 activities.

Brodie, J., Pearson, R.G., 2016. Ecosystem health of the Great Barrier Reef: Time for effective management action based on evidence. Estuarine Coastal and Shelf Science 183 438-451.

Brodie, J.E., Kroon, F.J., Schaffelke, B., Wolanski, E.C., Lewis, S.E., Devlin, M.J., Bohnet, I.C., Bainbridge, Z.T., Waterhouse, J., Davis, A.M., 2012. Terrestrial pollutant runoff to the Great Barrier Reef: An update of issues, priorities and management responses. Marine pollution bulletin 65(4–9) 81-100.

Bureau of Meteorology, 2017. eReefs Catchments: simulations, nowcasts, and forecasts of water quantity and quality flowing to the Great Barrier Reef, Final Report, eReefs Project Phase 3: Great Barrier Reef Foundation, Brisbane, QLD Australia.

Cacciapaglia, C., van Woesik, R., 2016. Climate-change refugia: shading reef corals by turbidity. Global change biology 22(3) 1145-1154.

Canto, M.M., Fabricius, K.E., Logan, M., Lewis, S., McKinna, L.I.W., Robson, B.J., submitted. A benthic light index of water quality in the Great Barrier Reef, Australia.

Carter, A.B., Collier, C.J., Lawrence, E., Rasheed, M.A., Robson, B., Coles, R., in prep. Modelling the spatial distrubution of 12 seagrass species on the Great Barrier Reef.

Carter, A.B., McKenna, S.A., Rasheed, M.A., Collier, C., McKenzie, L., Pitcher, R., Coles, R., submitted. Synthesizing 35 years of seagrass spatial data from the Great Barrier Reef World Heritage Area, Queensland, Australia. Limnology and Oceanography Letters.

Chartrand, K.M., Bryant, C.V., Carter, A.B., Ralph, P.J., Rasheed, M.A., 2016. Light Thresholds to Prevent Dredging Impacts on the Great Barrier Reef Seagrass, Zostera muelleri ssp. capricorni. Frontiers in Marine Science 3(106).

Chartrand, K.M., Szabo, M., Sinutok, S., Rasheed, M.A., Ralph, P.J., 2018. Living at the margins - The response of deep-water seagrasses to light and temperature renders them susceptible to acute impacts. Marine Environmental Research 136 126-138.

Coles, R.G., Rasheed, M.A., McKenzie, L.J., Grech, A., York, P.H., Sheaves, M., McKenna, S., Bryant, C., 2015. The Great Barrier Reef World Heritage Area seagrasses: Managing this iconic Australian ecosystem resource for the future. Estuarine Coastal and Shelf Science 153 A1-A12.

Collier, C., Chartrand, K., Honchin, C., Fletcher, A., Rasheed, M., 2016a. Light thresholds for seagrasses of the GBR: a synthesis and guiding document. Including knowledge gaps and future priorities, Report to the National Environmental Science Programme. Reef and Rainforest Research Centre Limited, p. 41.

Collier, C., Waycott, M., 2009. Drivers of change to seagrass distributions and communities on the Great Barrier Reef: literature review and gaps analysis. Reef and Rainforest Research Centre.

Collier, C., Waycott, M., McKenzie, L., 2012a. Light thresholds derived from seagrass loss in the coastal zone of the northern Great Barrier Reef, Australia. Ecological Indicators 23 211-219.

Collier, C.J., Adams, M.P., Langlois, L., Waycott, M., O'Brien, K.R., Maxwell, P.S., McKenzie, L., 2016b. Thresholds for morphological response to light reduction for four tropical seagrass species. Ecological Indicators 67 358-366.

Collier, C.J., Chatrand, K., Hionchin, C., Fletcher, A., Rasheed, M.A., 2016c. Light thresholds for seagrasses of the GBR: a synthesis and guiding document. Reef and Rainforest Research Centre: Cairns, Queensland.

Collier, C.J., Langlois, L., Ow, Y., Johansson, C., Giammusso, M., Adams, M.P., O'Brien, K.R., Uthicke, S., 2018. Losing a winner: thermal stress and local pressures outweigh the positive effects of ocean acidification for tropical seagrasses. New Phytologist 219(3) 1005-1017.

Collier, C.J., Uthicke, S., Waycott, M., 2011. Thermal tolerance of two seagrass species at contrasting light levels: Implications for future distribution in the Great Barrier Reef. Limnology and Oceanography 56(6) 2200-2210.

Collier, C.J., Waycott, M., McKenzie, L., 2012b. Light thresholds derived from seagrass loss in the coastal zone of the northern Great Barrier Reef, Australia. Ecological Indicators 23 211-219.

Collier, C.J., Waycott, M., Ospina, A.G., 2012c. Responses of four Indo-West Pacific seagrass species to shading. Marine pollution bulletin 65(4–9) 342-354.

Commonwealth of Australia, 2015. Reef 2050 long-term sustainability plan.

Cooper, T.F., Uthicke, S., Humphrey, C., Fabricius, K.E., 2007. Gradients in water column nutrients, sediment parameters, irradiance and coral reef development in the Whitsunday Region, central Great Barrier Reef. Estuarine, Coastal and Shelf Science 74(3) 458-470.

De'ath, G., Fabricius, K., 2010. Water quality as a regional driver of coral biodiversity and macroalgae on the Great Barrier Reef. Ecological Applications 20(3) 840-850.

De'ath, G., Fabricius, K.E., Sweatman, H., Puotinen, M., 2012. The 27-year decline of coral cover on the Great Barrier Reef and its causes. Proceedings of the National Academy of Sciences of the United States of America 109(44) 17995-17999.

Deloitte Access Economics, 2013. Economic contribution of the Great Barrier Reef: Great Barrier Reef Marine Park Authority Townsville.

Dennison, W.C., 1987. Effects of light on seagrass photosynthesis, growth and depth distribution. Aquatic Botany 27(1) 15-26.

Devlin, M., McKinna, L., Alvarez-Romero, J., Petus, C., Abott, B., Harkness, P., Brodie, J., 2012. Mapping the pollutants in surface riverine flood plume waters in the Great Barrier Reef, Australia. Marine pollution bulletin 65(4-9) 224-235.

Devlin, M., Petus, C., da Silva, E., Tracey, D., Wolff, N., Waterhouse, J., Brodie, J., 2015a. Water quality and river plume monitoring in the Great Barrier Reef: an overview of methods based on ocean colour satellite data. Remote Sensing 7(10) 12909.

Devlin, M., Schaffelke, B., 2009. Spatial extent of riverine flood plumes and exposure of marine ecosystems in the Tully coastal region, Great Barrier Reef. Marine and Freshwater Research 60(11) 1109-1122.

Devlin, M.J., Brodie, J., 2005. Terrestrial discharge into the Great Barrier Reef Lagoon: nutrient behavior in coastal waters. Marine pollution bulletin 51(1–4) 9-22.

Devlin, M.J., Petus, C., Da Silva, E., Tracey, D., Wolff, N.H., Waterhouse, J., Brodie, J., 2015b. Water quality and river plume monitoring in the Great Barrier Reef: an overview of methods based on ocean colour satellite data. Remote Sensing 7(10) 12909-12941.

DiPerna, S., Hoogenboom, M., Noonan, S., Fabricius, K., 2018. Effects of variability in daily light integrals on the photophysiology of the corals Pachyseris speciosa and Acropora millepora. PloS one 13(9) e0203882.

Eakin, C.M., Sweatman, H.P.A., Brainard, R.E., 2019. The 2014-2017 global-scale coral bleaching event: insights and impacts. Coral Reefs 38(4) 539-545.

Fabricius, K.E., 2005. Effects of terrestrial runoff on the ecology of corals and coral reefs: review and synthesis. Marine pollution bulletin 50(2) 125-146.

Fabricius, K.E., 2011. Factors Determining the Resilience of Coral Reefs to Eutrophication: A Review and Conceptual Model, In: Dubinsky, Z., Stambler, N. (Eds.), Coral Reefs: An Ecosystem in Transition. Springer Netherlands: Dordrecht, pp. 493-505.

Fabricius, K.E., De'ath, G., Humphrey, C., Zagorskis, I., Schaffelke, B., 2013. Intra-annual variation in turbidity in response to terrestrial runoff on near-shore coral reefs of the Great Barrier Reef. Estuarine, Coastal and Shelf Science 116 57-65.

Fabricius, K.E., Logan, M., Weeks, S., Brodie, J., 2014. The effects of river run-off on water clarity across the central Great Barrier Reef. Marine pollution bulletin 84(1-2) 191-200.

Fabricius, K.E., Logan, M., Weeks, S.J., Lewis, S.E., Brodie, J., 2016a. Changes in water clarity in response to river discharges on the Great Barrier Reef continental shelf: 2002-2013. Estuarine Coastal and Shelf Science 173 A1-A15.

Fabricius, K.E., Logan, M., Weeks, S.J., Lewis, S.E., Brodie, J., 2016b. Changes in water clarity in response to river discharges on the Great Barrier Reef continental shelf: 2002–2013. Estuarine, Coastal and Shelf Science 173 A1-A15.

Fabricius, K.E., Okaji, K., De'ath, G., 2010. Three lines of evidence to link outbreaks of the crown-of-thorns seastar Acanthaster planci to the release of larval food limitation. Coral Reefs 29(3) 593-605.

Fisher, R., Bessell-Browne, P., Jones, R., 2019. Synergistic and antagonistic impacts of suspended sediments and thermal stress on corals. Nature Communications 10(1) 2346.

Foxwell-Norton, K., Konkes, C., 2019. The Great Barrier Reef: News media, policy and the politics of protection. International Communication Gazette 81(3) 211-234.

Foxwell-Norton, K., Lester, L., 2017. Saving the Great Barrier Reef from disaster, media then and now. Media Culture & Society 39(4) 568-581.

Fraser, G., Rohde, K., Silburn, M., 2017. Fertiliser management effects on dissolved inorganic nitrogen in runoff from Australian sugarcane farms. Environmental Monitoring and Assessment 189(8).

Frouin, R., McPherson, J., 2012. Estimating photosynthetically available radiation at the ocean surface from GOCI data. Ocean Science Journal 47(3) 313-321.

Frouin, R., McPherson, J., Ueyoshi, K., Franz, B.A., 2012. A time series of photosynthetically available radiation at the ocean surface from SeaWiFS and MODIS data, Remote Sensing of the Marine Environment II. International Society for Optics and Photonics, p. 852519.

Furnas, M.M., 2003. Catchments and corals: terrestrial runoff to the Great Barrier Reef. Australian Institute of Marine Science & CRC Reef Research Centre.

Gattuso, J.-P., Gentili, B., Duarte, C.M., Kleypas, J.A., Middelburg, J.J., Antoine, D., 2006. Light availability in the coastal ocean: impact on the distribution of benthic photosynthetic organisms and contribution to primary production. Biogeosciences Discussions 3(4) 895-959.

Great Barrier Marine Park Authority, 2010a. Water quality guidelines for the Great Barrier Reef Marine Park. Great Barrier Marine Park Authority, Townsville.

Great Barrier Marine Park Authority, 2010b. Water quality guidelines for the Great Barrier Reef Marine Park (Revised Edition), Revised Edition ed. Great Barrier Reef Marine Park Authority: Townsville, Queensland.

Great Barrier Reef Marine Park Authority, 2018. Cumulative impact management policy. Great Barrier Reef Marine Park Authority.

Great Barrier Reef Marine Park Authority, 2019. Position statement: Climate change (Document no. 100486).

Gruber, R., Waterhouse, J., Logan, M., Petus, C., Howley, C., Lewis, S., Tracey, D., Langlois, L., Tonin, H., Skuza, M., Costello, P., Davidson, J., Gunn, K., Lefevre, C., Moran, D., Robson, B., Shanahan, M., Zagorskis, I., Shellberg, J., Neilen, A., 2020. Marine Monitoring Program: Annual Report for Inshore Water Quality Monitoring 2018-19, Report for the Great Barrier Reef Marine Park Authority: Great Barrier Reef Marine Park Authority, Townsville.

Gruber, R., Waterhouse, J., Logan, M., Petus, C., Howley, C., Lewis, S., Tracey, D., Langlois, L., Tonin, H., Skuza, M., Costello, P., Davidson, J., Gunn, K., Lefevre, C., Shanahan, M., Wright, M., Zagorskis, I., Kroon, F., Neilen, A., 2019. Marine Monitoring Program: Annual report for inshore water quality monitoring 2017-18, Report for the Great Barrier Reef Marine Park Authority.

Haltrin, V., 2002. Algorithm and code to calculate specular reflection of light from a wavy water surface. Naval Research Laboratory, Stennis Space Centre, MS Oceanography Division.

Haltrin, V.I., McBride, W.E., Weidemann, A.D., 2000. Fresnel reflection by wavy sea surface, IGARSS 2000. IEEE 2000 International Geoscience and Remote Sensing Symposium. Taking the Pulse of the Planet: The Role of Remote Sensing in Managing the Environment. Proceedings (Cat. No. 00CH37120). IEEE, pp. 1863-1865.

Heap, A.D., Harris, P.T., 2008. Geomorphology of the Australian margin and adjacent seafloor. Australian Journal of Earth Sciences 55(4) 555-585.

Hedge, P., Molloy, F., Sweatman, H., Hayes, K.R., Dambacher, J.M., Chandler, J., Bax, N., Gooch, M., Anthony, K., Elliot, B., 2017. An integrated monitoring framework for the Great Barrier Reef World Heritage Area. Marine Policy 77 90-96.

Herzfeld, M., Andrewartha, J., Baird, M., Brinkman, R., Furnas, M., Gillibrand, P., Hener, M., Joehnk, K.D., Jones, E., McKinnon, D., Margevlashvili, N., Mongin, M., Oke, P., Rizwi, F., Robson, B., Seaton, S., Skerratt, J., Tonin, H., Wild-Allen, K., 2016. eReefs Marine Modelling: Final Report. CSIRO: Hobart, Tasmania, p. 497.

Hooker, S.B., Esaias, W.E., 1993. An overview of the SeaWiFS project. Eos, Transactions American Geophysical Union 74(21) 241-246.

Howley, C., Devlin, M., Burford, M., 2018. Assessment of water quality from the Normanby River catchment to coastal flood plumes on the northern Great Barrier Reef, Australia. Marine and Freshwater Research 69(6) 859-873.

Hughes, T., Kerry, J., Simpson, T., 2018a. Large-scale bleaching of corals on the Great Barrier Reef. Ecology 99(2) 501-501.

Hughes, T.P., Kerry, J.T., Álvarez-Noriega, M., Álvarez-Romero, J.G., Anderson, K.D., Baird, A.H., Babcock, R.C., Beger, M., Bellwood, D.R., Berkelmans, R., Bridge, T.C., Butler, I.R., Byrne, M., Cantin, N.E., Comeau, S., Connolly, S.R., Cumming, G.S., Dalton, S.J., Diaz-Pulido, G., Eakin, C.M., Figueira, W.F., Gilmour, J.P., Harrison, H.B., Heron, S.F., Hoey, A.S., Hobbs, J.-P.A., Hoogenboom, M.O., Kennedy, E.V., Kuo, C.-y., Lough, J.M., Lowe, R.J., Liu, G., McCulloch, M.T., Malcolm, H.A., McWilliam, M.J., Pandolfi, J.M., Pears, R.J., Pratchett, M.S., Schoepf, V., Simpson, T., Skirving, W.J., Sommer, B., Torda, G., Wachenfeld, D.R., Willis, B.L., Wilson, S.K., 2017. Global warming and recurrent mass bleaching of corals. Nature 543 373.

Hughes, T.P., Kerry, J.T., Connolly, S.R., Baird, A.H., Eakin, C.M., Heron, S.F., Hoey, A.S., Hoogenboom, M.O., Jacobson, M., Liu, G., Pratchett, M.S., Skirving, W., Torda, G., 2019. Ecological memory modifies the cumulative impact of recurrent climate extremes. Nature Climate Change 9(1) 40-+.

Hughes, T.P., Kerry, J.T., Simpson, T., 2018b. Large-scale bleaching of corals on the Great Barrier Reef. Ecology 99(2) 501-501.

Hunka, A.D., Meli, M., Thit, A., Palmqvist, A., Thorbek, P., Forbes, V.E., 2013. Stakeholders' perspective on ecological modeling in environmental risk assessment of pesticides: challenges and opportunities. Risk Analysis: An International Journal 33(1) 68-79.

Hurrey, L.P., Pitcher, C.R., Lovelock, C.E., Schmidt, S., 2013. Macroalgal species richness and assemblage composition of the Great Barrier Reef seabed. Marine Ecology Progress Series 492 69-83.

Hutchings, P., Kingsford, M., Hoegh-Guldberg, O., 2008. The Great Barrier Reef : Biology, Environment and Management. CSIRO Publishing, Victoria, Australia.

Jayathilake, D.R.M., Costello, M.J., 2018. A modelled global distribution of the seagrass biome. Biological Conservation 226 120-126.

Jones, R., Giofre, N., Luter, H.M., Neoh, T.L., Fisher, R., Duckworth, A., 2020. Responses of corals to chronic turbidity. Scientific Reports 10(1) 4762.

Joo, M., Raymond, M.A.A., McNeil, V.H., Huggins, R., Turner, R.D.R., Choy, S., 2012. Estimates of sediment and nutrient loads in 10 major catchments draining to the Great Barrier Reef during 2006–2009. Marine pollution bulletin 65(4) 150-166.

Kirk, J.T.O., 1992. The Nature and Measurement of the Light Environment in the Ocean, In: Falkowski, P.G., Woodhead, A.D., Vivirito, K. (Eds.), Primary Productivity and Biogeochemical Cycles in the Sea. Springer US: Boston, MA, pp. 9-29.

Kirk, J.T.O., 2011. Light and Photosynthesis in Aquatic Ecosystems, 3rd Ed. Cambridge University Press.

Kleypas, J.A., 1997. Modeled estimates of global reef habitat and carbonate production since the Last Glacial Maximum. Paleoceanography 12(4) 533-545.

Kleypas, J.A., McManus, J.W., Meñez, L.A., 1999. Environmental limits to coral reef development: where do we draw the line? American Zoologist 39(1) 146-159.

Kroon, F.J., 2012. Towards ecologically relevant targets for river pollutant loads to the Great Barrier Reef. Marine pollution bulletin 65(4–9) 261-266.

Kroon, F.J., Thorburn, P., Schaffelke, B., Whitten, S., 2016. Towards protecting the Great Barrier Reef from land-based pollution. Global change biology 22(6) 1985-2002.

Kuhnert, P.M., Henderson, B.L., Lewis, S.E., Bainbridge, Z.T., Wilkinson, S.N., Brodie, J.E., 2012. Quantifying total suspended sediment export from the Burdekin River catchment using the loads regression estimator tool. Water Resources Research 48(4).

Kumar, L., Skidmore, A.K., Knowles, E., 1997. Modelling topographic variation in solar radiation in a GIS environment. International Journal of Geographical Information Science 11(5) 475-497.

Ladner, S., Arnone, R., Vandermeulen, R., Martinolich, P., Lawson, A., Bowers, J., Crout, R., Ondrusek, M., Fargion, G., 2014. Inter-satellite comparison and evaluation of Navy SNPP VIIRS and MODIS-Aqua ocean color properties, Ocean Sensing and Monitoring VI. International Society for Optics and Photonics, p. 911107.

Lambert, V.M., Collier, C., Brodie, J., Adams, M.P., Baird, M., Bainbridge, Z., Carter, A., Lewis, S., Rasheed, M.A., Saunders, M.I., O'Brien, K., 2020. Connecting Sediment Load Targets to Ecological Outcomes for Seagrass. Reef and Rainforest Research Centre Limited: Cairns, Queensland.

Larcombe, P., Carter, R.M., 2004. Cyclone pumping, sediment partitioning and the development of the Great Barrier Reef shelf system: a review. Quaternary Science Reviews 23(1) 107-135.

Leahy, S.M., Kingsford, M.J., Steinberg, C.R., 2013. Do Clouds Save the Great Barrier Reef? Satellite Imagery Elucidates the Cloud-SST Relationship at the Local Scale. PloS one 8(7) e70400.

Lee, Z.-P., Darecki, M., Carder, K.L., Davis, C.O., Stramski, D., Rhea, W.J., 2005a. Diffuse attenuation coefficient of downwelling irradiance: An evaluation of remote sensing methods. Journal of Geophysical Research: Oceans 110(C2) n/a-n/a.

Lee, Z.-P., Du, K.-P., Arnone, R., 2005b. A model for the diffuse attenuation coefficient of downwelling irradiance. Journal of Geophysical Research: Oceans 110(C2) n/a-n/a.

Lee, Z., Shang, S., Du, K., Wei, J., Arnone, R., 2014. Usable solar radiation and its attenuation in the upper water column. Journal of Geophysical Research: Oceans 119(2) 1488-1497.

Legendre, P., 2014. lmodel2: Model II Regression, R package version 1.7-2.

Lewis, S., Brodie, J., Endo, G.G.K., Lough, J., Bainbridge, Z., 2014. Synthesizing Historical Land Use Change, Fertiliser and Pesticide Usage and Pollutant Load Data in the Regulated Catchments to Quantify Baseline and Changing Pollutant Loads Exported to the Great Barrier Reef, Centre for Tropical Water & Aquatic Ecosystem Research (TropWATER) Technical Report 14/20: James Cook University, Townsville, p. 105.

Liaw, A., Wiener, M., 2002. Classification and Regression by randomForest. R news 2(3) 18-22.

Liu, X., Wang, M., 2019. Filling the gaps of missing data in the merged VIIRS SNPP/NOAA-20 ocean color product using the DINEOF method. Remote Sensing 11(2) 178.

Logan, M., Fabricius, K., Weeks, S., Canto, M., Noonan, S., Wolanski, E., Brodie, J., 2013. The relationship between Burdekin River discharges and photic depth in the central Great Barrier Reef, Report to the National Environmental Research Program. Reef and Rainforest Research Centre Limited, Cairns p. 29 pp.

Lucas, P., Webb, T., Valentine, P., Marsh, H., 1997. The outstanding universal value of the Great Barrier Reef world heritage area. Great Barrier Reef Marine Park Authority, Townsville.

MacNeil, M.A., Mellin, C., Matthews, S., Wolff, N.H., McClanahan, T.R., Devlin, M., Drovandi, C., Mengersen, K., Graham, N.A.J., 2019. Water quality mediates resilience on the Great Barrier Reef. Nature Ecology & Evolution 3(4) 620-627.

Magno-Canto, M.M., McKinna, L.I.W., Robson, B.J., Fabricius, K.E., 2019. Model for deriving benthic irradiance in the Great Barrier Reef from MODIS satellite imagery. Optics Express 27(20) A1350-A1371.

Magno-Canto, M.M., McKinna, L.I.W., Robson, B.J., Fabricius, K.E., Garcia, R., 2020a. Model for deriving benthic irradiance in the Great Barrier Reef from MODIS satellite imagery (vol 27, pg 1350, 2019). Optics Express 28(19) 27473-27475.

Magno-Canto, M.M., McKinna, L.I.W., Robson, B.J., Fabricius, K.E., Garcia, R., 2020b. Model for deriving benthic irradiance in the Great Barrier Reef from MODIS satellite imagery: erratum. Optics Express 28(19) 27473-27475.

Margvelashvili, N., Andrewartha, J., Baird, M., Herzfeld, M., Jones, E., Mongin, M., Rizwi, F., Robson, B., Skerratt, J., Wild-Allen, K., 2018. Simulated fate of catchment-derived sediment on the Great Barrier Reef shelf. Marine pollution bulletin 135 954-962.

McClain, C.R., Feldman, G.C., Hooker, S.B., 2004. An overview of the SeaWiFS project and strategies for producing a climate research quality global ocean bio-optical time series. Deep Sea Research Part II: Topical Studies in Oceanography 51(1-3) 5-42.

McCloskey, G., Waters, D., Baheerathan, R., Darr, S., Dougall, C., Ellis, R., Fentie, B., Hateley, L., 2017. Modelling pollutant load changes due to improved management practices in the Great Barrier Reef catchments: updated methodology and results, Technical Report for Reef Report Card 2014: Queensland Department of Natural Resources and Mines, Brisbane, Queensland.

McKenzie, L., Collier, C., Waycott, M., Unsworth, R., Yoshida, R., Smith, N., 2012. Monitoring inshore seagrasses of the GBR and responses to water quality.

McKenzie, L.J., Unsworth, R.K.F., Waycott, M., 2010. Reef Rescue Marine Monitoring Program: Intertidal Seagrass, Annual Report for the sampling period 1st September 2009 – 31st May 2010: Fisheries Queensland, Cairns.

McKinna, L.I., Werdell, P.J., 2018. Approach for identifying optically shallow pixels when processing ocean-color imagery. Optics Express 26(22) A915-A928.

McKinna, L.I.W., C., F.P.R., J., W.S., Jeremy, W.P., Martina, R., A., F.B., M., S.D., C., F.G., 2015. A semianalytical ocean color inversion algorithm with explicit water column depth and substrate reflectance parameterization. Journal of Geophysical Research: Oceans 120(3) 1741-1770.

Mellin, C., Matthews, S., Anthony, K.R.N., Brown, S.C., Caley, M.J., Johns, K.A., Osborne, K., Puotinen, M., Thompson, A., Wolff, N.H., Fordham, D.A., MacNeil, M.A., 2019. Spatial resilience of the Great Barrier Reef under cumulative disturbance impacts. Global change biology 25(7) 2431-2445.

Mobley, C.D., 1994. Light and water: radiative transfer in natural waters. Academic press.

Morel, A., 1988. Optical modeling of the upper ocean in relation to its biogenous matter content (Case I waters). Journal of Geophysical Research 93(10) 749-710.

Morel, A., Gentili, B., Claustre, H., Babin, M., Bricaud, A., Ras, J., Tièche, F., 2007. Optical properties of the “clearest” natural waters. Limnology and Oceanography 52(1) 217-229.

Morgan, K.M., Perry, C.T., Johnson, J.A., Smithers, S.G., 2017. Nearshore Turbid-Zone Corals Exhibit High Bleaching Tolerance on the Great Barrier Reef Following the 2016 Ocean Warming Event. Frontiers in Marine Science 4(224).

Mueller, J.L., 2000. SeaWIFS algorithm for the diffuse attenuation coefficient, K(490), using water-leaving radiances at 490 and 555 nm, In: Hooker, S.B. (Ed.), SeaWIFS Postlaunch Calibration and Validation Analyses NASA Goddard Space Flight Center: Greenbelt Md, pp. 24-27.

Muir, P.R., Wallace, C.C., Done, T., Aguirre, J.D., 2015. Limited scope for latitudinal extension of reef corals. Science 348(6239) 1135-1138.

Mumby, P.J., Chisholm, J.R., Edwards, A.J., Andrefouet, S., Jaubert, J., 2001. Cloudy weather may have saved Society Island reef corals during the 1998 ENSO event. Marine Ecology Progress Series 222 209-216.

Nachimuthu, G., Halpin, N.V., Bell, M.J., 2017. Impact of Practice Change on Runoff Water Quality and Vegetable Yield: An On-Farm Case Study. Agriculture-Basel 7(3).

NASA, SeaDAS: https://seadas.gsfc.nasa.gov/.

NASA Goddard Space Flight Center, Ocean Ecology Laboratory, Ocean Biology Processing Group, Moderate-resolution Imaging Spectroradiometer (MODIS) Aqua Ocean Color Data; 2018 Reprocessing: NASA OB.DAAC, Greenbelt, MD, USA. data/10.5067/AQUA/MODIS/L2/OC/2018. Accessed on 07/06/2020.

Neil, D.T., Orpin, A.R., Ridd, P.V., Yu, B., 2002. Sediment yield and impacts from river catchments to the Great Barrier Reef lagoon: a review. Marine and Freshwater Research 53(4) 733-752.

Noonan, S.H.C., DiPerna, S., Hoogenboom, M.O., Fabricius, K.E., (in prep). Effects of light variability and elevated CO2 on the adult and juvenile performance of two Acropora corals.

Olsson, J.A., Andersson, L., 2006. Possibilities and problems with the use of models as a communication tool in water resource management, Integrated Assessment of Water Resources and Global Change. Springer, pp. 97-110.

Orpin, A.R., Ridd, P.V., 2012. Exposure of inshore corals to suspended sediments due to wave-resuspension and river plumes in the central Great Barrier Reef: A reappraisal. Continental Shelf Research 47 55-67.

Ortiz, J.C., Wolff, N.H., Anthony, K.R.N., Devlin, M., Lewis, S., Mumby, P.J., 2018. Impaired recovery of the Great Barrier Reef under cumulative stress. Science Advances 4(7).

Packett, R., Dougall, C., Rohde, K., Noble, R., 2009. Agricultural lands are hot-spots for annual runoff polluting the southern Great Barrier Reef lagoon. Marine pollution bulletin 58(7) 976-986.

Petus, C., da Silva, E.T., Devlin, M., Wenger, A.S., Álvarez-Romero, J.G., 2014. Using MODIS data for mapping of water types within river plumes in the Great Barrier Reef, Australia: Towards the production of river plume risk maps for reef and seagrass ecosystems. Journal of Environmental Management 137 163-177.

Petus, C., Devlin, M., Teixera da Silva, E., Lewis, S., Waterhouse, J., Wenger, A., Bainbridge, Z., Tracey, D., 2018. Defining wet season water quality target concentrations for ecosystem conservation using empirical light attenuation models: A case study in the Great Barrier Reef (Australia). Journal of Environmental Management 213 451-466.

Phillips, S.J., Anderson, R.P., Schapire, R.E., 2006. Maximum entropy modeling of species geographic distributions. Ecological Modelling 190(3-4) 231-259.

Phillips, S.J., Dudik, M., 2008. Modeling of species distributions with Maxent: new extensions and a comprehensive evaluation. Ecography 31(2) 161-175.

Pitcher, R., Doherty, P., Arnold, P., Hooper, J., Gribble, N., Bartlett, C., Browne, M., Campbell, N., Cannard, T., Cappo, M., Carini, G., Chalmers, S., Cheers, S., Chetwynd, D., Colefax, A., Coles, R., Cook, S., Davie, P., De'ath, G., Devereux, D., Done, B., Donovan, T., Ehrke, B., Ellis, N., Ericson, G., Fellegara, I., Forcey, K., Furey, M., Gledhill, D., Good, N., Gordon, S., Haywood, M., Jacobsen, I., Johnson, J., Jones, M., Kinninmoth, S., Kistle, S., Last, P., Leite, A., Marks, S., McLeod, I., Oczkowicz, S., Rose, C., Seabright, D., Sheils, J., Sherlock, M., Skelton, P., Smith, D., Smith, G., Speare, P., Stowar, M., Strickland, C., Sutcliffe, P., Van der Geest, C., Venables, W., Walsh, C., Wassenberg, T., Welna, A., Yearsley, G., 2007. Seabed biodiversity on the continental shelf of the Great Barrier Reef World Heritage Area: AIMS/CSIRO/QM/QDPI CRC Reef Research Task Final Report., p. 315.

Plaganyi, E.E., Babcock, R.C., Rogers, J., Bonin, M., Morello, E.B., 2020. Ecological analyses to inform management targets for the culling of crown-of-thorns starfish to prevent coral decline. Coral Reefs 39(5) 1483-1499.

Platt, T., Sathyendranath, S., White, G.N., III, Ravindran, P., 1994. Attenuation of visible light by phytoplankton in a vertically structured ocean: solutions and applications. Journal of Plankton Research 16(11) 1461-1487.

Pratchett, M.S., Cumming, G.S., 2019. Managing cross-scale dynamics in marine conservation: Pest irruptions and lessons from culling of crown-of-thorns starfish (Acanthaster spp.). Biological Conservation 238.

Preen, A., Marsh, H., 1995. Response of Dugongs to Large-Scale Loss of Seagrass from Hervey Bay, Queensland, Australia. Wildlife Research 22(4) 507-519.

R Core Team, 2019a. R: A language and environment for statistical computing. Vienna, Austria.

R Core Team, 2019b. R: A language and environment for statistical computing. R Foundation for Statistical Computing: Vienna, Austria.

Ralph, P.J., Durako, M.J., Enríquez, S., Collier, C.J., Doblin, M.A., 2007. Impact of light limitation on seagrasses. Journal of Experimental Marine Biology and Ecology 350(1–2) 176-193.

Reichstetter, M., Fearns, P., Weeks, S., McKinna, L., Roelfsema, C., Furnas, M., 2015. Bottom Reflectance in Ocean Color Satellite Remote Sensing for Coral Reef Environments. Remote Sensing 7(12) 15852.

Rigby, P., Steinberg, C.R., Williams, D.K., Brinkman, G., Brinkman, R., Tonin, H., Hughes, D., 2014. Real-Time marine observing systems: Challenges, benefits and opportunities in Australian coastal waters. Australian Journal of Civil Engineering 12(1) 83-99.

Robillot, C., Logan, M., Baird, M., Waterhouse J., Martin, K., Schaffelke, B., 2018. Testing and implementation of an improved water quality index for the 2016 and 2017 Great Barrier Reef Report Cards: Summary Report, Report to the National Environmental Science Program.: Reef and Rainforest Research Centre Limited, Cairns, p. 65.

Robinson, I.S., 2004. Measuring the oceans from space: the principles and methods of satellite oceanography. Springer Science & Business Media.

Robinson, W.D., Franz, A., Patt, F.S., Bailey, S.W., Werdell, P.J., Lehrter, J.C., 2003. Chapter 6: Masks and Flags Update, In: Hooker, S.B., Firestone, E.R. (Eds.), NASA Technical Memorandum 2003-206892. NASA Goddard Space Flight Center, pp. 34-40.

Robson, B., Canto, M., Collier, C., di Perna, S., Logan, M., Fabricius, K., 2019. Benthic light as ecologically-validated GBR-wide indicator for water quality. NESP Tropical Water Hub: Townsville, Australia.

Robson, B., Skerratt, J., Baird, M., Davies, C., Herzfeld, M., Jones, E., Mongin, M., Richardson, A., Rizwi, F., Wild-Allen, K., 2020. Enhanced assessment of the eReefs biogeochemical model for the Great Barrier Reef using the Concept/State/Process/System model evaluation framework. Environmental Modelling & Software 104707.

Sakshaug, E., 1997. Parameters of photosynthesis: definitions, theory and interpretation of results. Journal of Plankton Research 19(11) 1637-1670.

Schaeffer, B., Hagy, J., Stumpf, R., 2013. Approach to developing numeric water quality criteria for coastal waters: transition from SeaWiFS to MODIS and MERIS satellites. Journal of Applied Remote Sensing 7(1) 073544.

Schaffelke, B., Carleton, J., Skuza, M., Zagorskis, I., Furnas, M.J., 2012. Water quality in the inshore Great Barrier Reef lagoon: Implications for long-term monitoring and management. Marine pollution bulletin 65(4–9) 249-260.

Schaffelke, B., Collier, C., Kroon, F., Lough, J., McKenzie, L., Ronan, M., Uthicke, S., Brodie, J., 2017. Chapter 1: The condition of coastal and marine ecosystems of the Great Barrier Reef and their responses to water quality and disturbances, In: Waterhouse, J., Schaeffelke, B., Bartley, R., Eberhard, R., Brodie, J., Star, M., Thorburn, P., Rolfe, J., Ronan, M., Taylor, B., Kroon, F. (Eds.), 2017 Scientific Consensus Statement: A synthesis of the science of land-based water quality impacts on the Great Barrier Reef. The State of Queensland: Townsville, Queensland.

Scott, A.L., York, P.H., Rasheed, M.A., 2020. Green turtle (Chelonia mydas) grazing plot formation creates structural changes in a multi-species Great Barrier Reef seagrass meadow. Marine Environmental Research 162 105183.

Seegers, B.N., Stumpf, R.P., Schaeffer, B.A., Loftin, K.A., Werdell, P.J., 2018. Performance metrics for the assessment of satellite data products: an ocean color case study. Optics Express 26(6) 7404-7422.

Siegel, D.A., Wang, M., Maritorena, S., Robinson, W., 2000. Atmospheric correction of satellite ocean color imagery: the black pixel assumption. Applied Optics 39(21) 3582-3591.

Skerratt, J.H., Mongin, M., Baird, M.E., Wild-Allen, K.A., Robson, B.J., Schaffelke, B., Davies, C.H., Richardson, A.J., Margvelashvili, N., Soja-Wozniak, M., Steven, A.D.L., 2019. Simulated nutrient and plankton dynamics in the Great Barrier Reef (2011-2016). Journal of Marine Systems 192 51-74.

Slivkoff, M.M., 2014. Ocean colour remote sensing of the Great Barrier Reef waters. Curtin University.

Smith, R.C., Baker, K.S., 1986. Analysis OF Ocean Optical Data II, pp. 95-107.

Star, M., Rolfe, J., McCosker, K., Smith, R., Ellis, R., Waters, D., Waterhouse, J., 2018. Targeting for pollutant reductions in the Great Barrier Reef river catchments. Environmental Science & Policy 89 365-377.

State of Queensland, 2018. Reef 2050 Water Quality Improvement Plan 2017-2022

Steven, A.D.L., Baird, M.E., Brinkman, R., Car, N.J., Cox, S.J., Herzfeld, M., Hodge, J., Jones, E., King, E., Margvelashvili, N., Robillot, C., Robson, B., Schroeder, T., Skerratt, J., Tickell, S., Tuteja, N., Wild-Allen, K., Yu, J., 2019. eReefs: An operational information system for managing the Great Barrier Reef. Journal of Operational Oceanography 1-17.

Strahl, J., Rocker, M.M., Fabricius, K.E., 2019. Contrasting responses of the coral Acropora tenuis to moderate and strong light limitation in coastal waters. Marine Environmental Research 147 80-89.

Stuart-Smith, R.D., Brown, C.J., Ceccarelli, D.M., Edgar, G.J., 2018. Ecosystem restructuring along the Great Barrier Reef following mass coral bleaching. Nature 560(7716) 92-+.

Suggett, D.J., Dong, L.F., Lawson, T., Lawrenz, E., Torres, L., Smith, D.J., 2013. Light availability determines susceptibility of reef building corals to ocean acidification. Coral Reefs 32(2) 327-337.

Sully, S., van Woesik, R., 2020. Turbid reefs moderate coral bleaching under climate-related temperature stress. Global change biology 26(3) 1367-1373.

Tan, P.L., Humphries, F., 2018. Adaptive or aspirational? Governance of diffuse water pollution affecting Australia's Great Barrier Reef. Water International 43(3) 361-384.

Thompson, A., Martin, K., Logan, M., 2020. Development of the coral index, a summary of coral reef resilience as a guide for management. Journal of Environmental Management 271.

Titlyanov, E.A., Latypov, Y.Y., 1991. Light-dependence in scleractinian distribution in the sublittoral zone of South China Sea Islands. Coral Reefs 10(3) 133-138.

Uthicke, S., Castro-Sanguino, C., Ferarri, R., Fabricius, K., Lawrey, E., Flores, F., Patel, F., Brunner, C., Negri, A., 2020. From Exposure to Risk: Novel Experimental Approaches to Analyse Cumulative Impacts and Determine Thresholds in the Great Barrier Reef World Heritage Area (GBRWHA). Australian Institute of Marine Science: Townsville, Queensland.

Vogel, N., Meyer, F.W., Wild, C., Uthicke, S., 2015. Decreased light availability can amplify negative impacts of ocean acidification on calcifying coral reef organisms. Marine Ecology Progress Series 521 49-61.

Waterhouse, J., Lønborg, C., Logan M., Petus, C., Tracey, D., Lewis, S., Tonin, H., Skuza, M., da Silva, E., Carreira, C., Costello, P., Davidson, J., Gunn, K., Wright, M., Zagorskis, I., Brinkman R., Schaffelke, B., 2017. Marine Monitoring Program: Annual Report for inshore water quality monitoring 2015-2016. Report for the Great Barrier Reef Marine Park Authority: Great Barrier Reef Marine Park Authority, Townsville, p. 227.

Waycott, M., Longstaff, B.J., Mellors, J., 2005. Seagrass population dynamics and water quality in the Great Barrier Reef region: A review and future research directions. Marine pollution bulletin 51(1-4) 343-350.

Weeks, S., Werdell, P.J., Schaffelke, B., Canto, M., Lee, Z., Wilding, J.G., Feldman, G.C., 2012. Satellite-derived photic depth on the Great Barrier Reef: spatio-temporal patterns of water clarity. Remote Sensing 4(12) 3781-3795.

Wells, S.C., Cole, S.J., Moore, R.J., Black, K.B., Khan, U., Hapuarachchi, P., Gamage, N., Hasan, M., MacDonald, A., Bari, M., Tuteja, N., 2017. Forecasting the water flows draining to the Great Barrier Reef using the G2G distributed hydrological model [Draft]: Wallingford, UK.

Werdell, P.J., McKinna, L.I.W., Boss, E., Ackleson, S.G., Craig, S.E., Gregg, W.W., Lee, Z., Maritorena, S., Roesler, C.S., Rousseaux, C.S., Stramski, D., Sullivan, J.M., Twardowski, M.S., Tzortziou, M., Zhang, X., 2018. An overview of approaches and challenges for retrieving marine inherent optical properties from ocean color remote sensing. Progress in Oceanography 160 186-212.

Whinney, J., Jones, R., Duckworth, A., Ridd, P., 2017. Continuous in situ monitoring of sediment deposition in shallow benthic environments. Coral Reefs 36(2) 521-533.

Wolff, N.H., Mumby, P.J., Devlin, M., Anthony, K.R.N., 2018. Vulnerability of the Great Barrier Reef to climate change and local pressures. Global Change Biology 24(5) 1978-1991.

Wood, S.N., 2011. Fast stable restricted maximum likelihood and marginal likelihood estimation of semiparametric generalized linear models. Journal of the Royal Statistical Society Series B-Statistical Methodology 73 3-36.

Yaakub, S.M., Chen, E., Bouma, T.J., Erftemeijer, P.L.A., Todd, P.A., 2014. Chronic light reduction reduces overall resilience to additional shading stress in the seagrass Halophila ovalis. Marine pollution bulletin 83(2) 467-474.

Reef & Rainforest
RESEARCH CENTRE